

## ABSTRACT

Title of thesis: ANALYSIS OF PROPANE GAS FIRE EXPERIMENTS AND SIMULATIONS IN RESIDENTIAL SCALE STRUCTURES

Joseph M. Willi, Master of Science, 2017

Dissertation directed by: Professor James A. Milke  
Department of Fire Protection Engineering

Nine full-scale fire experiments were conducted in two residential-scale structures with a fire source provided by three propane gas burners. Five of the experiments were conducted in a single-story structure, and four were conducted in a two-story structure. The structures were instrumented to measure temperature; oxygen and carbon dioxide gas concentrations; gas velocity; and heat flux. Various doors and vents were opened and closed during the experiments to provide passive horizontal and vertical ventilation. Additionally, a positive pressure ventilation fan was used to provide forced ventilation during some of the tests. Numerical simulations of the nine experiments were conducted using Fire Dynamics Simulator (FDS) (version 6.5.3). The simulation results were compared to the experimental data, and overall, the predicted temperatures, gas concentrations, and heat fluxes from the simulations were within the expected agreement range based on the calculated experimental and model relative standard deviations and model bias factors provided by the FDS Validation Guide for each quantity. The one significant discrepancy between expected agreement and actual agreement of the simulation data and

experimental data occurred with the gas velocity measurements, which produced a model relative standard deviation that was 0.18 larger than the value provided in the FDS Validation Guide. Overall, comparing the experimental results to the FDS simulation results suggest that there is sufficient agreement between the two and that FDS is capable of accurately modeling certain fire scenarios in one and two story, residential-sized structures.

Analysis of Propane Gas Fire Experiments and Simulations in  
Residential Scale Structures

by

Joseph Martin Willi

Thesis submitted to the Faculty of the Graduate School of the  
University of Maryland, College Park in partial fulfillment  
of the requirements for the degree of  
Master of Science  
2017

Advisory Committee:  
Professor James A. Milke, Chair  
Professor Arnaud Trouve  
Dr. Craig Weinschenk

© Copyright by  
Joseph Martin Willi  
2017

## Acknowledgments

[PLACEHOLDER]

## Table of Contents

List of Tables	v
List of Figures	vi
List of Abbreviations	ix
1 Introduction	1
2 Experimental Setup	4
2.1 Test Structures . . . . .	4
2.1.1 Construction . . . . .	4
2.1.2 Layout . . . . .	8
2.2 Instrumentation . . . . .	10
2.2.1 East Structure . . . . .	12
2.2.2 West Structure . . . . .	13
2.2.3 Measurement Uncertainty . . . . .	17
3 Experimental Procedure	20
3.1 East Structure Burner Tests . . . . .	22
3.1.1 Tests 2–4 . . . . .	22
3.1.2 Tests 5 & 6 . . . . .	24
3.2 West Structure Burner Tests . . . . .	27
3.2.1 Tests 22 & 23 . . . . .	27
3.2.2 Tests 24 & 25 . . . . .	29
4 Numerical Model Description	31
4.1 Computational Domain . . . . .	32
4.1.1 Numerical Mesh . . . . .	33
4.2 Source Fire Characterization . . . . .	35
4.3 Additional Input Parameters . . . . .	39

5	Results and Discussion	44
5.1	Mesh Sensitivity Studies	44
5.2	FDS Model Output Compared to Experimental Data	49
5.2.1	Temperature	52
5.2.2	Gas Species Concentration	61
5.2.3	Gas Velocity	65
5.2.4	Total Heat Flux	68
5.2.5	Summary	70
6	Conclusion	73
A	Channel Lists	75
A.1	East Structure	75
A.2	West Structure	79
B	Experimental and FDS Data Plots	85
B.1	Temperature	85
B.2	Gas Species Concentration	111
B.3	Gas Velocity	127
B.4	Total Heat Flux	128
	Bibliography	129

## List of Tables

3.1	Summary of Propane Gas Burner Experiments. . . . .	21
3.2	Heat Release Rates for Tests 5 and 6. . . . .	24
3.3	Heat Release Rates for Tests 22–25. . . . .	27
4.1	Tests 2–4 Estimated Heat Release Rates Using MQH Correlation. . . . .	38
4.2	Various Materials Defined Within Each FDS Input File and the Corresponding MATL Namelist Group Parameter Values. . . . .	42
4.3	Instrumentation Specified within FDS Input File and Corresponding DEVC Namelist Group Properties. . . . .	43
5.1	Calculated $\delta$ , $\sigma_E$ , and $\sigma_M$ Values Compared to Values Stated in FDS Validation Guide. . . . .	70
A.1	East Structure Channel List . . . . .	75
A.2	West Structure Channel List . . . . .	79

## List of Figures

2.1	North side of the East and West Structures . . . . .	6
2.2	Ceiling support of the West Structure . . . . .	7
2.3	Dimensioned floor plan of the East Structure . . . . .	8
2.4	Dimensioned floor plans of the West Structure . . . . .	9
2.5	Instrumentation legend . . . . .	11
2.6	Three propane burners used as the fuel source . . . . .	11
2.7	Locations and labels of instrumentation in the East Structure . . . . .	12
2.8	Bi-directional probe plus solid thermocouple arrays in East Structure	14
2.9	Locations and labels of instrumentation in the West Structure. . . . .	15
2.10	Locations and labels of instrumentation in the West Structure . . . . .	16
3.1	Tests 2–4 layout and event times. . . . .	23
3.2	Test 5 layout and event times. . . . .	25
3.3	Test 6 layout and event times. . . . .	26
3.4	Tests 22–23 layout and event times. . . . .	28
3.5	Tests 24–25 layout and event times. . . . .	30
5.1	$O_2$ concentrations for East Structure simulations of various mesh sizes.	45
5.2	Ceiling jet temperatures for East Structure simulations of various mesh sizes. . . . .	46
5.3	$O_2$ concentrations for West Structure simulations of various mesh sizes.	47
5.4	Ceiling jet temperatures for West Structure simulations of various mesh sizes. . . . .	48
5.5	Plots of measured and predicted hot gas layer temperatures during Test 22. . . . .	54
5.6	Summary of measured and predicted hot gas layer temperatures. . . . .	55
5.7	Plots of measured and predicted ceiling jet temperatures during Test 4.	57
5.8	Summary of measured and predicted ceiling jet temperatures. . . . .	58
5.9	Plots of measured and predicted thermocouple array temperatures during Test 24. . . . .	59
5.10	Summary of measured and predicted temperatures obtained from thermocouple arrays. . . . .	60

5.11	Plots of measured and predicted $O_2$ concentration during Test 3 . . . . .	61
5.12	Summary of measured and predicted $O_2$ concentrations. . . . .	62
5.13	Plots of measured and predicted $CO_2$ concentration during Test 3 . . . . .	63
5.14	Summary of measured and predicted $CO_2$ concentrations. . . . .	64
5.15	Plots of measured and predicted gas velocity through the roof vent during Test 5. . . . .	66
5.16	Summary of measured and predicted gas velocity measurements. . . . .	67
5.17	Plots of measured and predicted heat flux during Test 23. . . . .	68
5.18	Summary of measured and predicted heat flux measurements. . . . .	69
B.1	Plots of measured and predicted hot gas layer temperatures during Test 2. . . . .	85
B.2	Plots of measured and predicted hot gas layer temperatures during Test 3. . . . .	86
B.3	Plots of measured and predicted hot gas layer temperatures during Test 4. . . . .	87
B.4	Plots of measured and predicted hot gas layer temperatures during Test 5. . . . .	88
B.5	Plots of measured and predicted hot gas layer temperatures during Test 6. . . . .	89
B.6	Plots of measured and predicted hot gas layer temperatures during Test 23. . . . .	90
B.7	Plots of measured and predicted hot gas layer temperatures during Test 24. . . . .	91
B.8	Plots of measured and predicted hot gas layer temperatures during Test 25. . . . .	92
B.9	Plots of measured and predicted ceiling jet temperatures during Test 2. .	93
B.10	Plots of measured and predicted ceiling jet temperatures during Test 2. .	94
B.11	Plots of measured and predicted ceiling jet temperatures during Test 3. .	95
B.12	Plots of measured and predicted ceiling jet temperatures during Test 3. .	96
B.13	Plots of measured and predicted ceiling jet temperatures during Test 4. .	97
B.14	Plots of measured and predicted ceiling jet temperatures during Test 5. .	98
B.15	Plots of measured and predicted ceiling jet temperatures during Test 5. .	99
B.16	Plots of measured and predicted ceiling jet temperatures during Test 6. .	100
B.17	Plots of measured and predicted ceiling jet temperatures during Test 6. .	101
B.18	Plots of measured and predicted ceiling jet temperatures on the first floor during Test 22. . . . .	102
B.19	Plots of measured and predicted ceiling jet temperatures on the sec- ond floor during Test 22. . . . .	103
B.20	Plots of measured and predicted ceiling jet temperatures on the first floor during Test 23. . . . .	104
B.21	Plots of measured and predicted ceiling jet temperatures on the sec- ond floor during Test 23. . . . .	105
B.22	Plots of measured and predicted ceiling jet temperatures on the first floor during Test 24. . . . .	106

B.23 Plots of measured and predicted ceiling jet temperatures on the second floor during Test 24. . . . .	107
B.24 Plots of measured and predicted ceiling jet temperatures on the first floor during Test 25. . . . .	108
B.25 Plots of measured and predicted ceiling jet temperatures on the second floor during Test 25. . . . .	109
B.26 Plots of measured and predicted thermocouple array temperatures during Test 24. . . . .	110
B.27 Plots of measured and predicted $O_2$ concentration during Test 2. . . . .	111
B.28 Plots of measured and predicted $O_2$ concentration during Test 4. . . . .	112
B.29 Plots of measured and predicted $O_2$ concentration during Test 5. . . . .	113
B.30 Plots of measured and predicted $O_2$ concentration during Test 6. . . . .	114
B.31 Plots of measured and predicted $O_2$ concentration during Test 22. . . . .	115
B.32 Plots of measured and predicted $O_2$ concentration during Test 23. . . . .	116
B.33 Plots of measured and predicted $O_2$ concentration during Test 24. . . . .	117
B.34 Plots of measured and predicted $O_2$ concentration during Test 25. . . . .	118
B.35 Plots of measured and predicted $CO_2$ concentration during Test 2. . . . .	119
B.36 Plots of measured and predicted $CO_2$ concentration during Test 4. . . . .	120
B.37 Plots of measured and predicted $CO_2$ concentration during Test 5. . . . .	121
B.38 Plots of measured and predicted $CO_2$ concentration during Test 6. . . . .	122
B.39 Plots of measured and predicted $CO_2$ concentration during Test 22. . . . .	123
B.40 Plots of measured and predicted $CO_2$ concentration during Test 23. . . . .	124
B.41 Plots of measured and predicted $CO_2$ concentration during Test 24. . . . .	125
B.42 Plots of measured and predicted $CO_2$ concentration during Test 25. . . . .	126
B.43 Plots of measured and predicted gas velocity through the roof vent during Test 5. . . . .	127
B.44 Plots of measured and predicted heat flux during Test 23. . . . .	128

## List of Abbreviations

CFD	Computational Fluid Dynamics
FDS	Fire Dynamics Simulator
NIST	National Institute of Standards and Technology
OSB	Oriented Strand Board
TJI	Truss Joist I-beams

## Chapter 1: Introduction

The development and behavior of compartment fires, such as those inside residential-scale structures, depend greatly on the ventilation conditions within the compartment. Nine full-scale fire experiments were conducted to study how opening and closing different doors and other vents affect ventilation and the fire environment within residential-sized structures. The experiments were conducted in two experimental structures designed to replicate a single-story and a two-story dwelling. The fire source for each experiment was provided by three gas propane burners. The flow of propane to the burners was controlled by a high-precision turn valve and the total displaced gas volume was measured using a rotary gas meter. Local measurements of temperature, gas concentrations, gas velocity, and heat flux were collected at various locations throughout the structure while the ventilation within the structure was varied. During a number of the tests, a PPV fan was used in conjunction with the opening and closing of vents to further affect the ventilation conditions within the fire environment.

Numerical simulations of the nine tests were performed using the program Fire Dynamics Simulator (FDS) (version 6.5.3) [1]. FDS is a computational fluid dynamics (CFD) model of thermally-driven fluid flow that is developed and maintained by

the National Institute of Standards and Technology (NIST). FDS numerically solves a form of the Navier-Stokes equations for low-speed ( $Ma < 0.3$ ), thermally-driven flows with an emphasis on smoke and heat transport from fires. The FDS Technical Reference Guide [2] provides a complete description of the model, including the formulation of the equations and numerical algorithm utilized by the software. FDS is mathematically verified [3] and validated against a continually growing database of experimental data from a variety of fire scenarios [4].

Fire protection engineers commonly use CFD models to predict fire dynamics and smoke movement for potential fire scenarios as they are developing certain fire safety designs. FDS is the most commonly used program for this type of application. Therefore, it's crucial that the program is validated for a wide range of fire scenarios, including those within residential-scale structures. Currently, there are a limited number of experiments for which FDS has been validated that involve fires within residential-scale structures. Furthermore, there are no cases described within the FDS Validation Guide that involve multi-story residential-scale structures. So, generating FDS simulations of the nine gas burner experiments and comparing the model data to the experimental data from the burner tests will provide a crucial addition to the FDS validation database.

This report contains a thorough description of the experimental structures and instrumentation used to collect data during the nine propane burner experiments. The procedures followed during each test are also outlined in detail. Following the experimental descriptions, the methodology used to create and execute the FDS simulations of each gas burner experiment is presented. Following the model de-

scription, the data output by the models are compared to the corresponding sensor measurements of temperature;  $O_2$  and  $CO_2$  gas concentration; gas velocity; and heat flux. Plots of simulation data and experimental data over the duration of the tests are presented in addition to log/log scatter plots of the predicted data versus the corresponding sensor data. Relative standard deviation values for the model and experimental data were calculated and used to determine a model bias factor for each data type. Finally, the standard deviation values and model bias factors are compared to the values listed within the FDS Validation Guide and any discrepancies between the two are discussed.

## Chapter 2: Experimental Setup

The series of field experiments described in this report were conducted in two structures of similar design located at the Delaware County Emergency Services Training Center in Sharon Hill, Pennsylvania. Three propane burners were used to fuel the fire for all experiments, and various sensors were used to collect gas temperature, gas velocity, heat flux, and gas concentration measurements throughout the structure.

### 2.1 Test Structures

#### 2.1.1 Construction

Each test structure was built on a concrete slab as shown in Figure 2.1. The East Structure was designed to simulate a single-story residential structure, and the West Structure was designed to simulate a two-story residential structure.

#### *First Floor of Both Structures*

The first floor of each structure had outer walls composed of interlocking concrete blocks measuring 0.6 m (2.0 ft) wide, 0.6 m (2.0 ft) high, and 1.2 m (4.0 ft)

long. The joints and gaps between the blocks were filled with high temperature insulation. All doors along the outer walls were composed of steel.

The first floor interior walls of each structure were framed with steel studs set to 400 mm (16 in) centers and track. Two layers of 16 mm (0.63 in) Type X gypsum board lined the steel studs, and a layer of 13 mm (0.5 in) thick Durock cement board covered the gypsum board. The interior ceiling of each structure was covered by two layers of 13 mm (0.5 in) thick Durock cement board.

The first floor ceiling support of each structure was composed of wood truss joist I-beams (TJIs). Each TJI had a depth of 298 mm (11.75 in) and contained laminated veneer lumber flanges with a cross section of 29 mm (1.13 in) by 44 mm (1.75 in) and an 11 mm (0.43 in) thick oriented strand board (OSB) web as shown in Figure 2.2. A layer of 18.3 mm (0.72 in) thick tongue and groove OSB was attached to the top of the TJIs.

### *Second Floor of West Structure*

The second floor of the West Structure was built on the structure's first floor wood ceiling support. The two floors were connected by an interior stairwell. A door made of lauan plywood was located at the top of the stairwell. The walls on the second floor were of wood-frame with 51 mm (2 in) by 102 mm (4 in) studs set to 400 mm (16 in) centers. Two layers of 16 mm (0.63 in) Type X gypsum board lined the interior side of the wood studs, and a layer of 13 mm (0.5 in) thick Durock cement board covered the gypsum board. The interior ceiling of the second story was



Figure 2.1: North side of the East Structure (top) and West Structure (bottom).



Figure 2.2: First floor ceiling support of the West Structure composed of wood truss joist I-beams. View is of the southeast corner of the structure.

covered by two layers of 13 mm (0.5 in) thick Durock cement board. The exterior sides of the outer walls on the second floor were protected by 11 mm (0.44 in) thick OSB and 8 mm (0.31 in) fiber cement lap siding.

### *Leakage*

An air leakage measurement system was used to measure the amount of leakage associated with each structure. The amount of leakage in the East Structure was measured as  $0.024 \text{ m}^2$ . For the West Structure, the leakage was measured as  $0.027 \text{ m}^2$  when the stairway door was fully closed,  $0.054 \text{ m}^2$  when the stairway door was fully opened, and  $0.048 \text{ m}^2$  when the stairway door was in the “closed” position (having a 152 mm (6 in) gap between the door and the frame) used during Tests 24 and 25.

## 2.1.2 Layout

Dimensioned floor plans of the East and West Structures are presented in Figures 2.3 and 2.4, respectively.

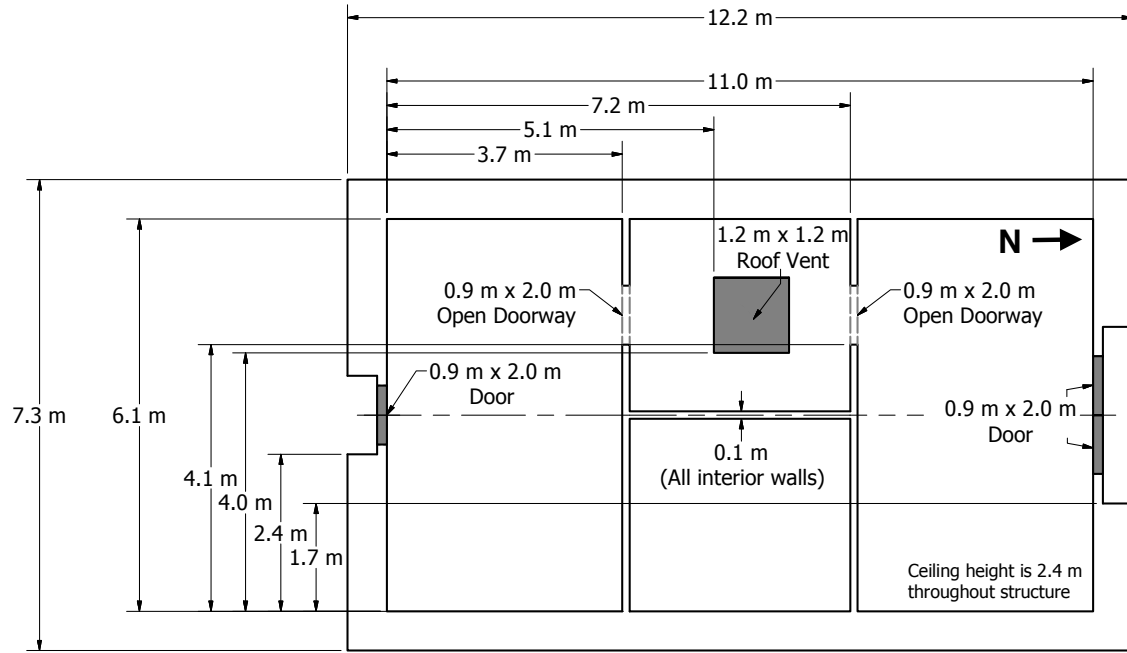


Figure 2.3: Dimensioned floor plan of the East Structure. Structure dimensions are symmetric across horizontal centerline.

The exterior doors of both structures, the stairwell door in the West Structure, and the square roof vent with a depth of 320 mm (12.75 in) in the East Structure were opened and closed at certain instances during the experiments to change the ventilation patterns within the structures.

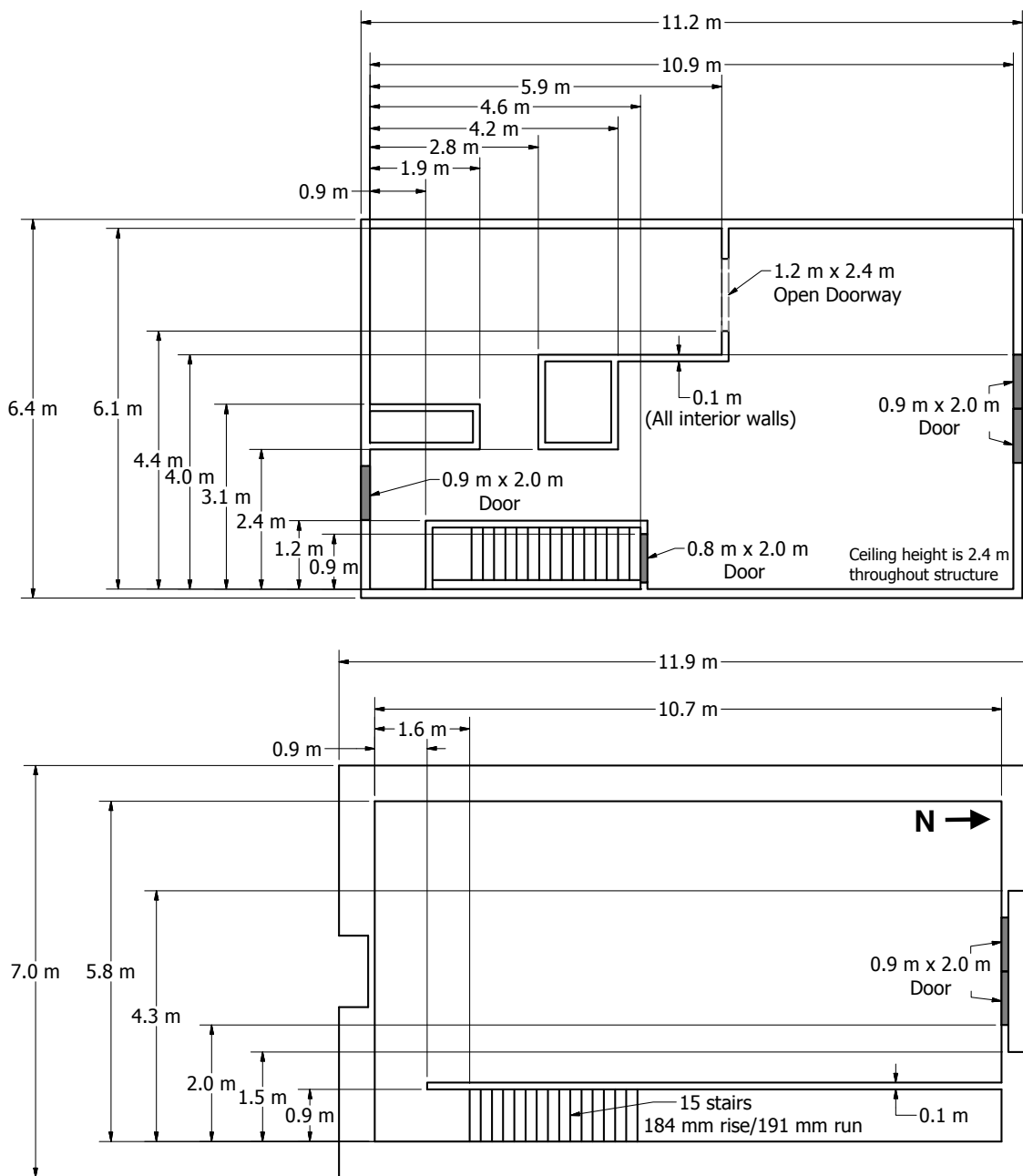


Figure 2.4: Dimensioned floor plan of the second floor (top) and first floor (bottom) of the West Structure.

## 2.2 Instrumentation

The structures were instrumented for temperature, gas velocity, heat flux, and gas concentration measurements. Gas temperatures in the burn rooms were measured with bare-bead, Chromel-Alumel (type K) thermocouples. Additional single thermocouples were installed in conjunction with bi-directional probes for gas velocity measurements. The single thermocouples were bare-bead, Chromel-Alumel (type K) thermocouples with a 1.0 mm (0.04 in) nominal diameter. The thermocouple wire was protected with a 3.2 mm (0.13 in) diameter inconel sheath. Schmidt-Boelter gauges were used to measure both total heat flux and radiant heat flux (radiometer). A radiometer is a total heat flux gauge with a zirconium plate to prevent contributions from convective heat transfer. Calibrated pumps pulled gas samples through a sample conditioning system to eliminate moisture in the sample. Then, the dry gas samples were piped to a series of gas analyzers and the concentrations of oxygen, carbon monoxide, and carbon dioxide were measured. A legend is presented in Figure 2.5 to clarify the instrumentation schematic diagrams presented in the follow sections.

Three diffusion flame burners, pictured in Figure 2.6, were used as the fuel source in each experiment. Each burner had a square opening of side length 0.6 m (2 ft) located 0.14 m (5.5 in) above the floor and were positioned 0.6 m (2 ft) from the south and west walls on the first floor of each structure. Propane was supplied to the burners during all experiments. The flow of propane to each burner was controlled by a high-precision turn valve, and the total displaced gas volume was

Thermocouple Array	
Bi-directional Probe Array	
Heat Flux Gauge	
Gas Measurement	
0.6 m x 0.6 m Propane Burner	

Figure 2.5: Legend used for schematic diagrams of instrumentation locations.

measured using a rotary gas meter.



Figure 2.6: Three propane burners located 0.6 m (2 ft) off the south and west interior walls on the first floor that provided the fire source for the experiments.

### 2.2.1 East Structure

The East Structure was instrumented with five bare-bead thermocouple arrays, four bi-directional probe plus solid thermocouple arrays, five total heat flux plus radiometer sensor pairs, and two gas sample inlet pipes at the locations shown in Figure 2.7.

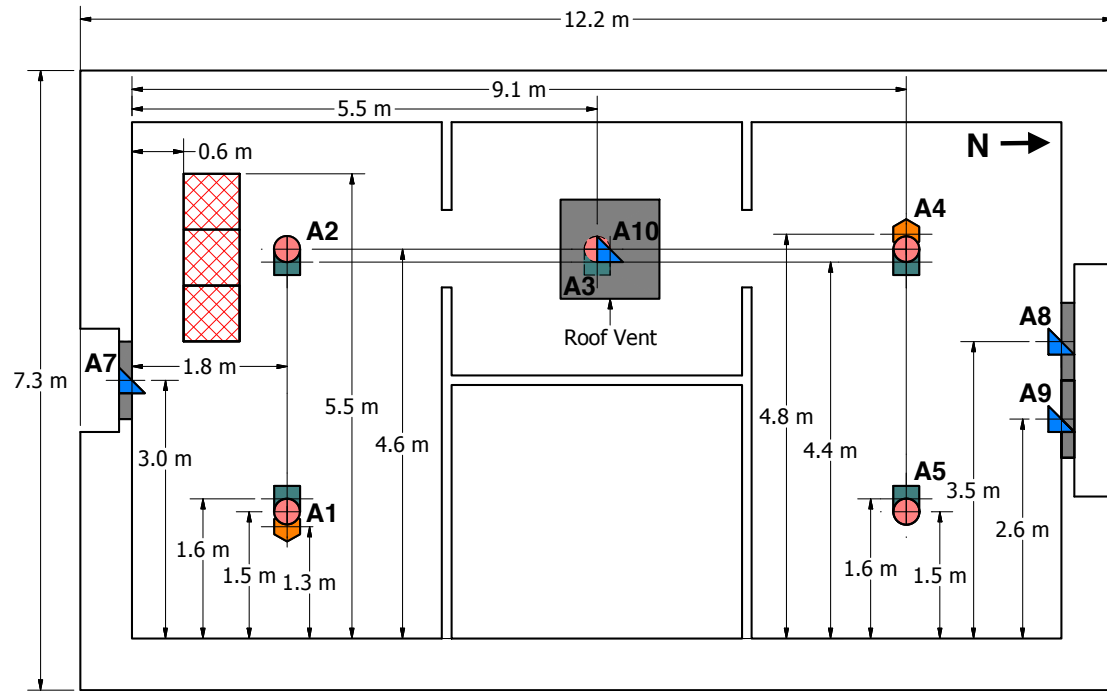


Figure 2.7: Locations and labels of instrumentation in the East Structure.

Each bare-bead thermocouple array was composed of eight thermocouples. Three bi-directional probe and solid thermocouple arrays (A7, A8, and A9) were centered in the exterior doorways of the structure and contained eight probes as shown in Figure 2.8. The fourth bi-directional probe and solid thermocouple array (A10), also presented in Figure 2.8, was located at the opening of the roof vent, 320 mm (12.75 in) above the compartment ceiling. The array contained three probes

centered between the east and west sides of the vent. The position of each probe and thermocouple pair relative to the south wall of the vent is listed in Table A.1 in Appendix A. The total heat flux gauge/radiometer pairs were aimed to view the ceiling. Gas samples were pulled through 9.5 mm (0.38 in) diameter stainless steel tubing. The height of each individual sensor in the sensor arrays is listed in Table A.1.

### 2.2.2 West Structure

The first floor of the West Structure was instrumented with three bare-bead thermocouple arrays, two bi-directional probe plus solid thermocouple arrays, and one gas sample inlet pipe. The second floor was equipped with three bare-bead thermocouple arrays, four bi-directional probe plus solid thermocouple arrays, two total heat flux sensor pairs, and one gas sample inlet pipe. The location of the instrumentation in the West Structure is shown in Figure 2.10.

The thermocouple arrays and the bi-directional probe plus solid thermocouple arrays contained eight sensors per array. Gas samples were pulled through 9.5 mm (0.38 in) diameter stainless steel tubing located 1.2 m (4 ft) above the floor. Each pair of total heat flux sensors was located 1.0 m (3.3 ft) above the floor. The pair at A16 contained one sensor facing the ceiling and another facing the north side of the room, and the pair at A17 contained one sensor facing the ceiling and another facing the stairway door. The height of each individual sensor in the sensor arrays is listed in the channel list found in Table A.2.



Figure 2.8: Bi-directional probe plus solid thermocouple array at the south exterior doorway (top) and roof vent (bottom) of the East Structure.

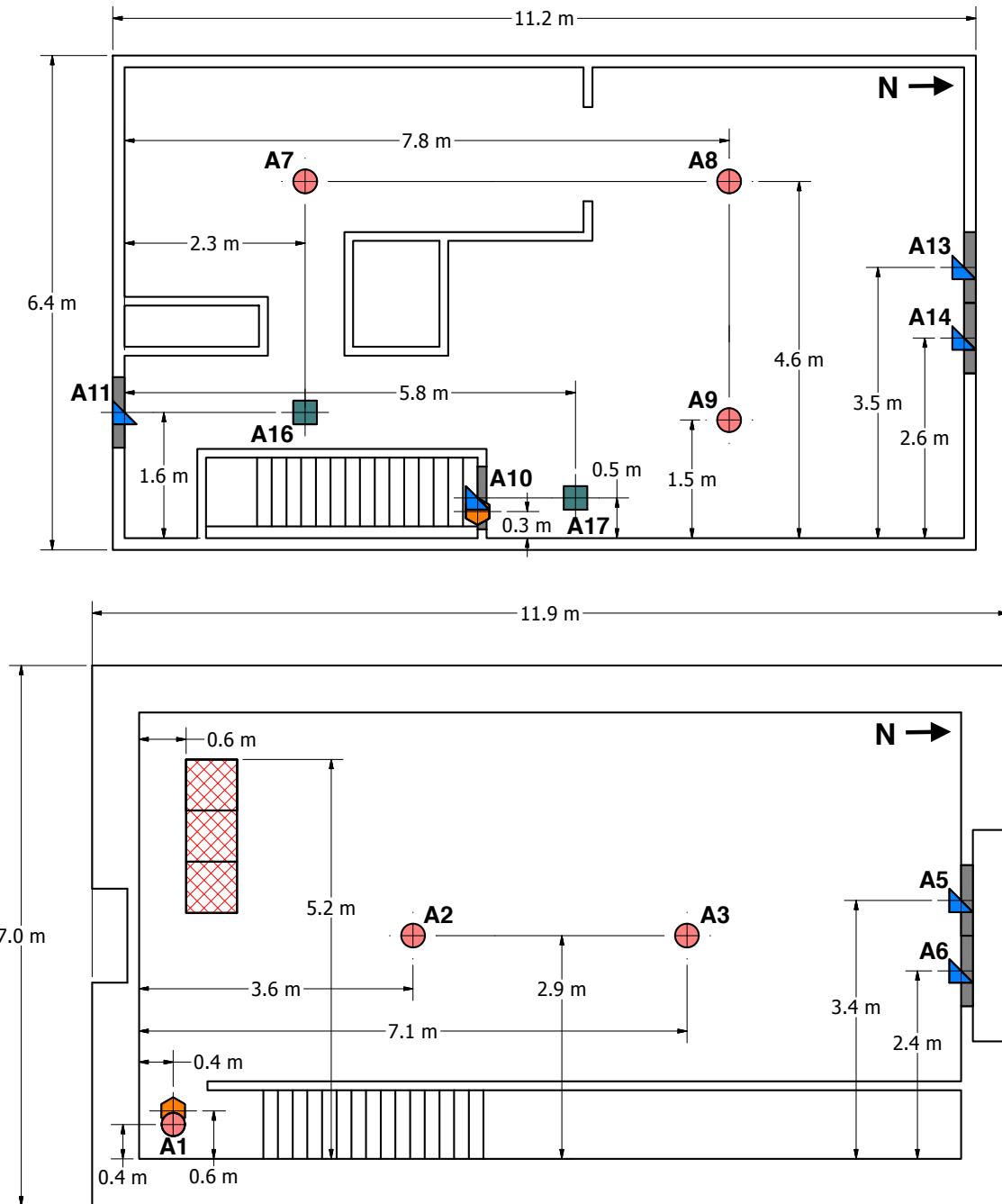


Figure 2.9: Locations and labels of instrumentation in the second floor (top) and first floor (bottom) of the West Structure.

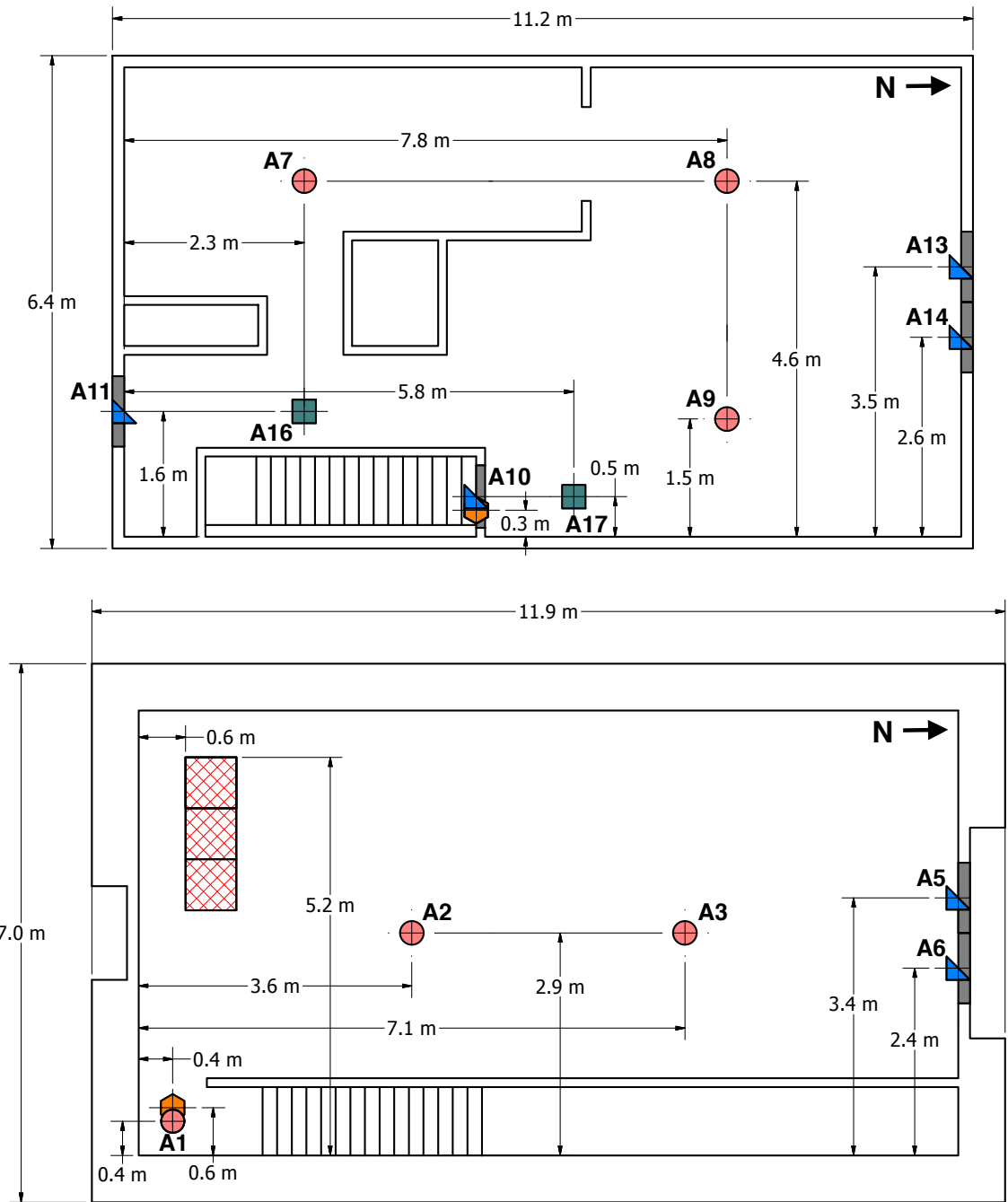


Figure 2.10: Locations and labels of instrumentation in the second floor (top) and first floor (bottom) of the West Structure.

### 2.2.3 Measurement Uncertainty

This section lists the uncertainties in the reported length, mass, temperature, heat flux, gas concentration, gas velocity, and heat release rate measurements. Uncertainty estimates are based either on manufacturer literature or analyses performed by others for similar measurement devices and techniques. In accordance with NIST guidelines [5], measurement accuracy is reported as an *expanded uncertainty* or 95 % ( $2\sigma$ ) confidence interval. Most manufacturer specifications express accuracy in terms of a *standard uncertainty* or 68 % ( $1\sigma$ ) confidence interval.

#### *Compartment Dimensions*

Room dimensions and instrumentation array locations were made with a hand held laser measurement device with a standard uncertainty of  $\pm 6.0$  mm (0.25 in) over a range of 0.6 m (2.0 ft) to 15 m (50.0 ft) according to the manufacturer [6]. Steel measuring tapes with a resolution of  $\pm 0.5$  mm (0.02 in) were used to locate measurement devices. The steel measuring tapes were manufactured in compliance with NIST Manual 44, which specifies a tolerance of  $\pm 1.6$  mm (0.06 in) for 9.1 m (30 ft) tapes and  $\pm 6.4$  mm (0.25 in) for 30.5 m (100 ft) tapes [7]. These uncertainties are all well within the precision of the reported dimensions, which are typically rounded to the nearest 10 cm (4 in).

## *Thermocouples*

The standard uncertainty in the temperature of the thermocouple wire itself as determined by the wire manufacturer, OMEGA Engineering, Inc., is  $\pm 2.2$  °C at 277 °C and increases to  $\pm 9.5$  °C at 871 °C [8]. The variation of the temperature in the environment surrounding the thermocouple is known to be much greater than that of the wire uncertainty. Expanded uncertainties as high as 20 % for upper layer temperatures measured by a 1 mm bare-bead type K thermocouple have been reported by NIST researchers [9, 10]. Small diameter thermocouples were used during these experiments to limit the impact of radiative heating and cooling. The estimated expanded uncertainty associated with the temperature measurements is  $\pm 15$  %.

## *Heat Flux Gauges*

Total heat flux measurements were made with water-cooled Schmidt-Boelter gauges. The manufacturer, MEDTHERM Corporation, reports a  $\pm 3$  % calibration expanded uncertainty for these devices [11]. Results from an international study on total heat flux gauge calibration and response demonstrated that the expanded uncertainty of a Schmidt-Boelter gauge is typically  $\pm 8$  % [12].

## *Gas Sampling*

A gas sampling system from California Analytical Instruments, Inc. (model 602P) having a relative expanded uncertainty of  $\pm 1$  % when compared to span gas

volume fractions [13] was used to make gas concentration measurements. However, according to a study by Lock et al. [14], the non-uniformity and movement of exhaust gases contribute to an estimated expanded uncertainty of  $\pm 12\%$ .

### *Bi-Directional Probes*

Bi-directional probes with Setra 264 pressure transducers from Setra Systems, Inc. were used to measure gas velocity in doorways. Bryant [15] calculated an expanded uncertainty ranging from  $\pm 14\%$  to  $\pm 22\%$  for bi-directional probes of similar design.

### Heat Release Rate

A positive displacement rotary gas meter was used to measure the volume flow rate of propane into the gas burners. The manufacturer, Romet Limited, reports a relative standard uncertainty of  $\pm 2\%$  [16] for this type of meter (model RM-3000). A volumetric flow rate was calculated from the gas meter volume readings and used in conjunction with the heat of combustion of propane to calculate the heat release rate of the fire. The total expanded uncertainty for the heat release rate obtained from this method is estimated to be  $\pm 8\%$ .

## Chapter 3: Experimental Procedure

A similar procedure was followed for all experiments described in this report.

First, three propane burners were ignited in sequential order. Next, various actions, such as opening and closing doors and roof vents or turning on a fan, were performed to change the ventilation pattern within the structure. Finally, the burners were turned off and the fire was extinguished. The nine tests were conducted in series with a variety of other experiments. In order to be consistent with the original test numbering, the gas burner experiments presented in this report are referred to as Tests 2–6 and Tests 22–25. The nine experiments and their different parameters are summarized in Table 3.1 below. Note, the heat release rates for Tests 2–4 are not reported because they were not able to be accurately measured during the tests.

Table 3.1: Summary of Propane Gas Burner Experiments.

Name	Structure	Duration of Fire (min:sec)	Heat Release Rate Rate (kW)	Ventilation
Test 2	East	16:01	N/A	Both double doors, south door, PPV after fire
Test 3	East	16:58	N/A	Both double doors, south door, PPV after fire
Test 4	East	16:59	N/A	Both double doors, south door, PPV after fire
Test 5	East	9:36	1190	Roof vent, both double doors
		10:15	1190	Roof vent, both double doors
		9:32	1190	Roof vent, both double doors
Test 6	East	5:27	1190	Roof vent, west double door
		5:03	1190	Roof vent, west double door
		5:12	1180	Roof vent, west double door
Test 22	West	16:58	1240	Both sets of double doors, 2nd floor south door, PPV fan
Test 23	West	16:58	1290	Both sets of double doors, PPV fan
Test 24	West	16:58	1270	West double door on both floors, 2nd floor south door, PPV fan
Test 25	West	16:58	1270	West double door on both floors, 2nd floor south door, PPV fan

### 3.1 East Structure Burner Tests

Five different tests, Tests 2–6, were conducted in the East Structure. Table 3.2 lists the heat release rates for Tests 5 and 6. The time between the ignition of each gas burner for Tests 5 and 6 was on the order of seconds. As a result, a single heat release rate, one for all three burners ignited, is reported.

#### 3.1.1 Tests 2–4

Tests 2–4 followed a nearly identical order of events. Figure 3.1 includes a floor plan schematic and table of event times corresponding to the data files for each test. A 0.61 cm (2.0 ft) diameter PPV fan located 1.6 m (5.2 ft) away from the south exterior door was aimed at the center of the doorway and used during Tests 2–4. During these experiments, the south exterior door was not able to completely close due to an obstruction caused by the hoses used to transport the propane to the burners. So, when the south door was in the “closed” position, a 133 mm (5.25 in) opening was present between the door and its frame. For all other experiments, however, the south exterior door was not used and the doorway remained closed for the entirety of the test. To fully close the doorway during these tests, the hinged door was removed, and gypsum board was used to cover the doorway.

Event Times (sec) for Tests 2–4 Data Files

Event	Test 2	Test 3	Test 4
(1) Corner burner on	0	0	0
(2) Middle burner on	181	181	179
(3) Center burner on	361	361	360
(4) West double door opened	418	416	415
(5) East double door opened	538	536	535
(6) South exterior door opened	604	597	597
(7) Center burner off	720	778	778
(8) Middle burner off	840	898	897
(9) Corner burner off	961	1018	1019
(10) PPV fan on	1256	1316	1319
(11) PPV fan off	1892	N/A	1380
(12) PPV fan on	N/A	N/A	1487

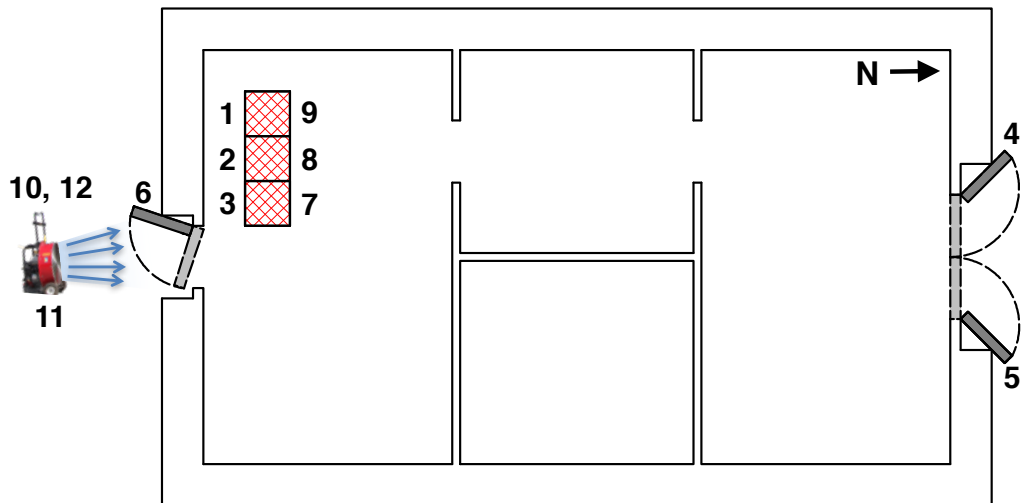


Figure 3.1: Tests 2–4 layout and event times.

### 3.1.2 Tests 5 & 6

The procedures for Tests 5 and 6 are outlined in Figure. 3.2 and 3.3, respectively. Both tests involved repeating a specific set of events three times in a row. To avoid listing the identical actions three separate times in the “event” column of the tables, each repetition of events is denoted as a “sequence” (abbreviated as “seq.”), and each table contains three columns of times — one for each sequence.

Table 3.2: Heat Release Rates for Tests 5 and 6.

Test	Heat Release Rate (kW) All Burners On
Test 5 - Seq. 1	1190
Test 5 - Seq. 2	1190
Test 5 - Seq. 3	1190
Test 6 - Seq. 1	1190
Test 6 - Seq. 2	1190
Test 6 - Seq. 3	1180

Event Times (sec) for Test 5 Data File

Event	Seq. 1	Seq. 2	Seq. 3
(1) All burners on	0	1225	2425
(2) Roof vent opened	154	1345	2545
(3) West double door opened	175	1432	2632
(4) East double door opened	361	1524	2730
(5) Roof vent closed	445	1723	2852
(6) All burners off	576	1840	2997
(7) Roof vent opened	720	1890	3086
(8) East double door closed	1148	2311	N/A
(9) West double door closed	1164	2330	N/A
(10) Roof vent closed	1179	2387	N/A

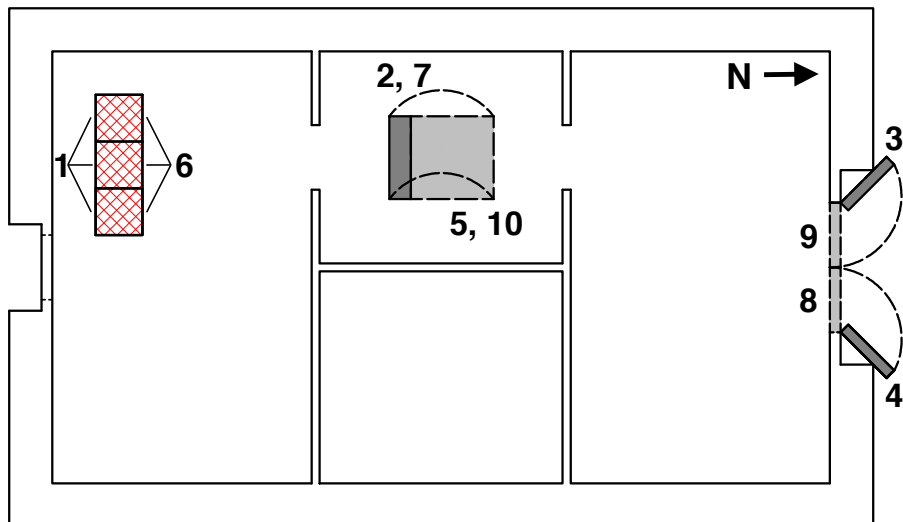


Figure 3.2: Test 5 layout and event times.

Event Times (sec) for Test 6 Data File

Event	Seq. 1	Seq. 2	Seq. 3
(1) All burners on	0	565	1075
(2) West double door opened	116	685	1195
(3) Roof vent opened	207	747	1287
(4) All burners off	327	868	1387
(5) East double door opened	369	911	1446
(6) Roof vent closed	494	1040	N/A
(7) East double door closed	522	1012	N/A
(8) West double door closed	538	1025	N/A

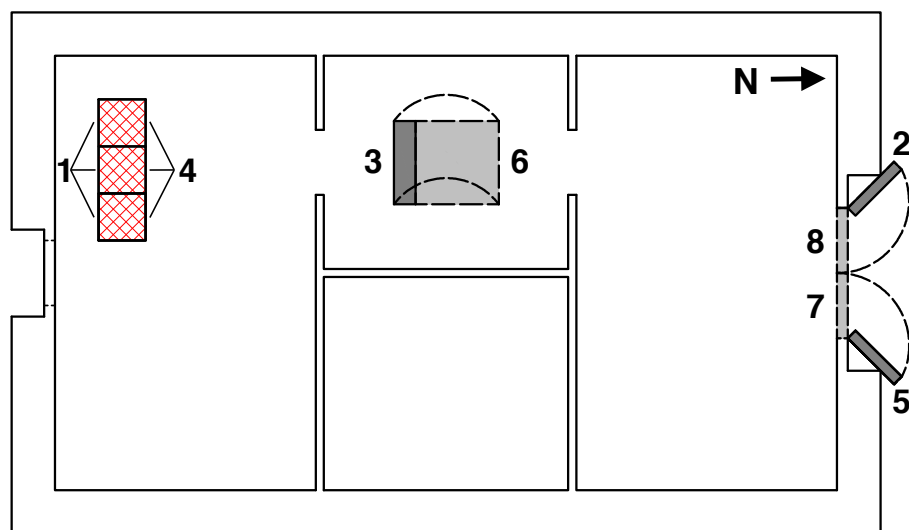


Figure 3.3: Test 6 layout and event times.

## 3.2 West Structure Burner Tests

Four different tests, Tests 22–25, were conducted in the West Structure. Table 3.3 lists the calculated heat release rate for each test. Similar to Tests 5 and 6, Tests 22–25 had a duration on the order of seconds between the ignition of each burner, so only the heat release rate for when all three burners were ignited is reported.

Table 3.3: Heat Release Rates for Tests 22–25.

Test	Heat Release Rate (kW) All Burners On
Test 22	1240
Test 23	1290
Test 24	1270
Test 25	1270

### 3.2.1 Tests 22 & 23

Tests 22 and 23 followed a nearly identical procedure. The starting configuration for Test 22 had the second story south exterior door in the opened position, while the starting configuration for Test 23 had the same door in the closed position. Figure 3.4 includes a floor plan schematic and table of event times corresponding to the data files for Tests 22 and 23. A 0.61 m (2.0 ft) diameter PPV fan located 2.3 m (7.5 ft) away from the first level double doors and aimed at the center of the two doors was used during the tests to change the ventilation pattern within the structure.

Event Times (sec) for Tests 22–23 Data Files

Event	Test 22	Test 23
(1) All burners on	0	0
(2) 2nd floor west double door opened	194	130
(3) 1st floor west double door opened	314	252
(4) 1st floor east double door opened	450	371
(5) 2nd floor south exterior door closed	511	N/A
(6) 2nd floor east double door opened	585	498
(7) PPV fan on	652	612
(8) PPV fan off	798	761
(9) All burners off	829	794
(10) 2nd floor south exterior door opened	899	849
(11) PPV fan on	1065	940
(12) 2nd floor south exterior door closed	1176	N/A

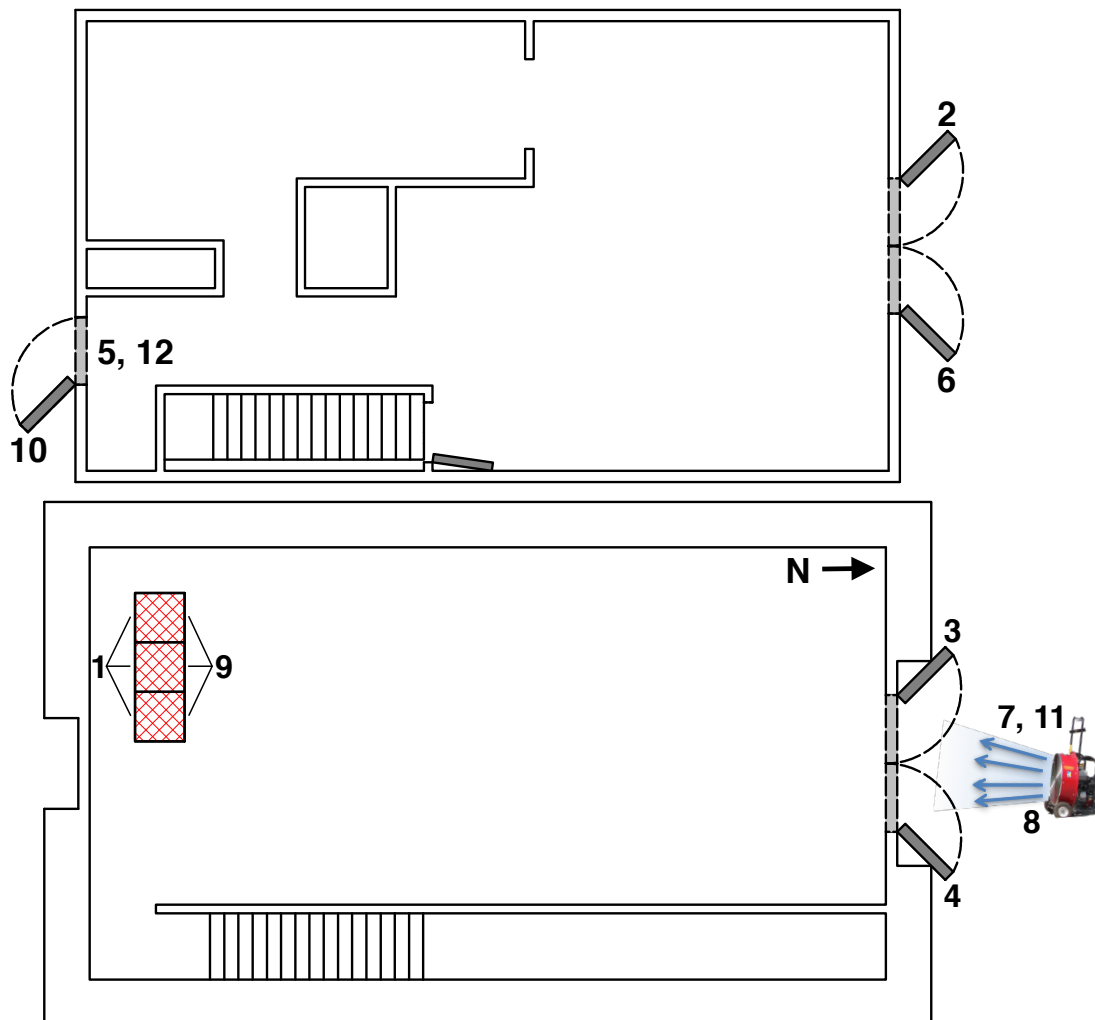


Figure 3.4: Tests 22–23 layout and event times.

### 3.2.2 Tests 24 & 25

Like Tests 22 and 23, Tests 24 and 25 followed a nearly identical procedure. The starting configuration for Test 24 had the south exterior door on the second level in the opened position, while the starting configuration for Test 25 had the same door in the closed position. During both tests, the stairwell door was unable to completely close. When it was in the “closed” position at the beginning of each test, there was a 152 mm (6.0 in) gap between the door and its frame. Figure 3.5 includes a floor plan schematic and table of event times corresponding to the data files for Tests 24 and 25. A 0.61 m (2.0 ft) diameter PPV fan located 2.3 m (7.5 ft) away from the first level double doors and aimed at the center of the west double door was used during the tests to change the ventilation pattern within the structure.

Event Times (s) for Tests 24–25 Data Files

Event	Test 24	Test 25
(1) All burners on	0	0
(2) Interior stairwell door opened	144	112
(3) 1st floor west double door opened	265	244
(4) 2nd floor west double door opened	383	353
(5) 2nd floor south exterior door closed	452	N/A
(6) 2nd floor south exterior door opened	502	474
(7) PPV fan on	624	594
(8) All burners off	746	721
(9) 2nd floor east double door opened	877	N/A
(10) 1st floor east double door opened	N/A	836

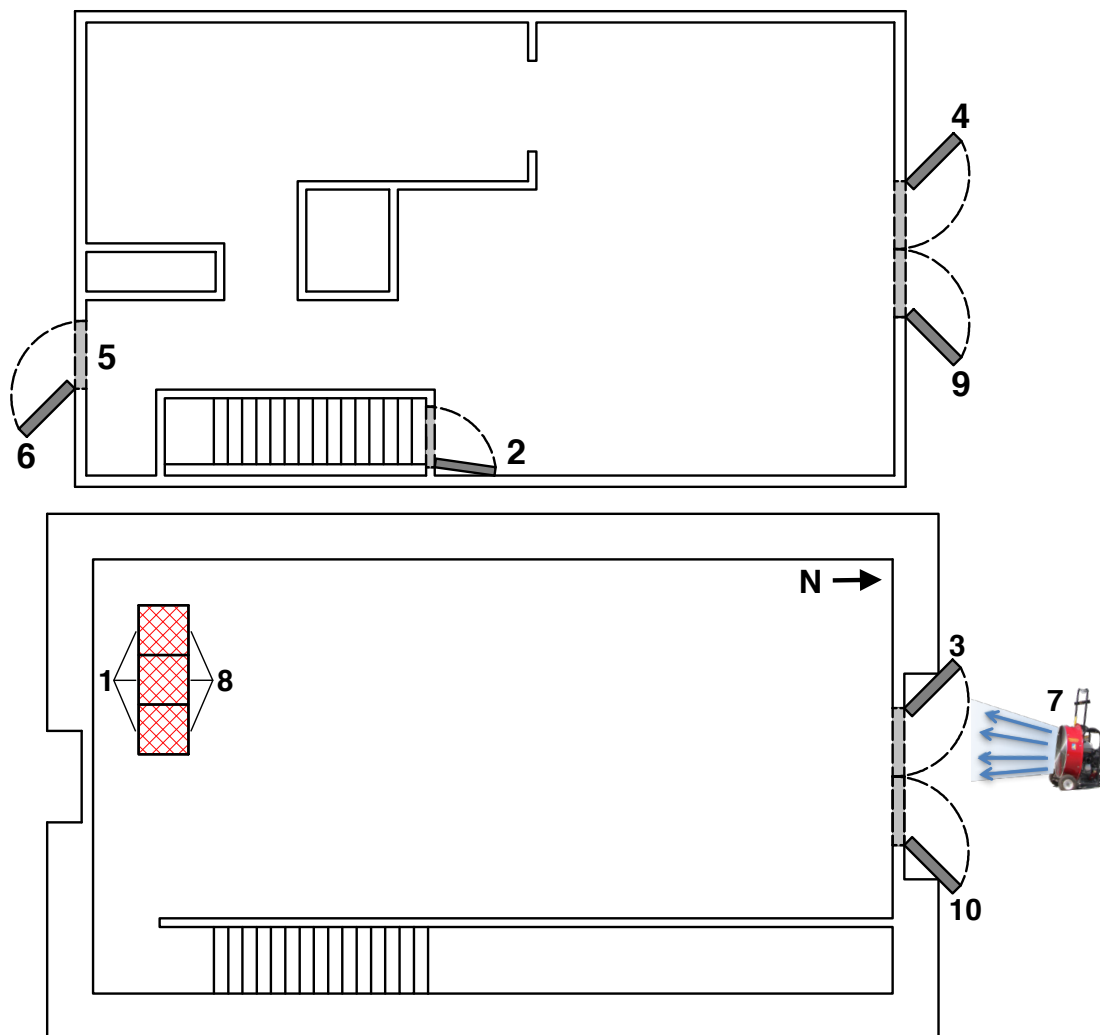


Figure 3.5: Tests 24–25 layout and event times.

## Chapter 4: Numerical Model Description

Fire Dynamics Simulator (FDS) (version 6.5.3) [1], a computational fluid dynamics (CFD) model of thermally-driven fluid flow that is developed and maintained by the National Institute of Standards and Technology (NIST), was used to numerically model the burner experiments described in Chapter 3. FDS numerically solves a form of the Navier-Stokes equations for low-speed ( $Ma < 0.3$ ), thermally-driven flows with an emphasis on smoke and heat transport from fires. The FDS Technical Reference Guide [2] provides a complete description of the model, including the formulation of the equations and numerical algorithm utilized by the software. FDS is mathematically verified [3] and validated against a continually growing database of experimental data from different fire scenarios [4].

FDS performs calculations within a computational domain that is composed of rectilinear volumes called meshes. Each mesh is divided into three-dimensional rectangular computational cells. Using the laws of mass, momentum, and energy conservation, FDS calculates the gas density, velocity, temperature, pressure, and species concentration within each grid cell and determines the generation and movement of fire gases within the domain. In general, the number of cells within each mesh (i.e., the grid cell size) determines the resolution of the mesh: the smaller the

size of the cells, the higher the resolution of the simulation. However, increasing the resolution of a simulation increases the need for more computational resources and produces a longer simulation run time. Thus, it's critical to determine a proper grid cell size for the meshes within an FDS computational domain based on the resources available. In order to select an appropriate cell size for the simulations of the gas burner experiments, a mesh sensitivity analysis, described in Section 4.1.1, was performed.

In addition to defining the meshes and cells within the computational domain, other types of input data must be known and considered to properly formulate a fire model. Key input parameters that were specified within the FDS input files of the gas burner experiment simulations and additional characteristics of the model setup are described throughout the sections of this chapter.

## 4.1 Computational Domain

The entire computational domain for the East Structure simulations was set to 14 m in the  $x$  direction, 8 m in the  $y$  direction, and 3 m in the  $z$  direction, and the computational domain for the West Structure simulations spanned 14 m in the  $x$  direction, 8 m in the  $y$  direction, and 5.4 m in the  $z$  direction. Each structure was centered between the  $x$  and  $y$  boundaries of its respective domain, and the ground of the first floor was set at  $z = 0$  m. The structures were modeled with the same dimensions shown in the floor plan drawings presented in Figures 2.3 and 2.4 of Chapter 2.

The entire computational domain for each simulation was divided into eight different meshes to utilize the Message-Passing Interface (MPI) feature of FDS that allows multiple computers, or multiple cores on one computer, to run a multi-mesh FDS job with each mesh as its own process. All simulations were executed by utilizing MPI parallel processing on a multi-processor Linux machine.

#### 4.1.1 Numerical Mesh

According to the FDS User Guide, a measure of how well the flow field is resolved for a simulation involving buoyant plumes is provided by the result of the expression  $D^*/\delta x$ , known as the resolution index (RI), in which  $D^*$  is the characteristic fire diameter defined as

$$D^* = \left( \frac{\dot{Q}}{\rho_\infty c_p T_\infty \sqrt{g}} \right)^{2/5} \quad (4.1)$$

where  $\dot{Q}$  is the total heat release rate of the fire (kW),  $\delta x$  is the nominal size of each grid cell (m),  $\rho_\infty$  is the density ( $\text{kg}/\text{m}^3$ ) of the surrounding gas (air),  $c_p$  is the specific heat ( $\text{kJ}/(\text{kg}\cdot\text{K})$ ) surrounding air,  $T_\infty$  is the temperature (K) surrounding air, and  $g$  is gravity ( $\text{m}/\text{s}^2$ ).

To determine the grid cell size to prescribe to the meshes within the model simulations, a mesh sensitivity study was performed for the Test 4 simulation in the East Structure and the Test 25 simulation in the West Structure. Three different grid cell sizes corresponding to the coarse, medium, and fine meshes were used in the mesh sensitivity study: 14 cm, 10 cm, and 5 cm for the East Structure

and 7 cm for the West Structure, respectively. These corresponded to RI values ranging from 5–7 for the coarse grid, 8–11 for the medium grid, and 15–20 for the fine grid. Previous FDS validation work from the U.S. Nuclear Regulatory Commission suggest that RI values from 4 to 16 generated adequate results in terms of engineering calculations [17].

The characteristic fire diameter and resulting RI values were similar for all the FDS simulations, so the results from the mesh sensitivity analysis of one simulation was used to determine and justify the grid cell size for all burner experiment simulations conducted within the same structure. The full results from the sensitivity studies are presented in Section 5.1 of Chapter 5. As a result of the study, the medium grid with cell size 10 cm was chosen for all simulations. This cell size results in a domain with 336,000 computational grid cells for the East Structure and a domain with 604,800 computational grid cells for the West Structure.

As previously mentioned, the computational domain was divided into eight equally sized meshes. The first mesh was defined by the MESH namelist group and was assigned a MULT\_ID quantity corresponding to a multiplier utility defined by the MULT namelist group. For example, the mesh in the Test 2 input file was defined by the following

```
&MESH IJK=35,40,30, XB=-1.5,2.0,-0.8,3.2,0.0,3.0,  
      MULT_ID='mesh' /
```

with the assigned MULT\_ID defined as

```
&MULT_ID='mesh', DX=3.5, DY=4.0, I_UPPER=3, J_UPPER=1 /
```

This creates an array of eight meshes with identical  $z1$  and  $z2$  bounds from 0.0 to 3.0 and  $x1$ ,  $x2$ ,  $y1$ ,  $y2$  bounds that vary according to the following:

$$x1' = -1.5 + 3.5i \quad \text{for } 0 \leq i \leq 3$$

$$x2' = 2.0 + 3.5i \quad \text{for } 0 \leq i \leq 3$$

$$y1' = -0.8 + 4j \quad \text{for } 0 \leq j \leq 1$$

$$y2' = 3.2 + 4j \quad \text{for } 0 \leq j \leq 1$$

where  $i$  and  $j$  are integers.

## 4.2 Source Fire Characterization

Each propane burner in the simulations was modeled as having steel sides and a 0.6 m x 0.6 m surface held at a constant temperature of 500 °C at 0.1 m above the ground with a specified mass flux (kg/(m<sup>2</sup>s)) of propane corresponding to the burner's heat release rate in the positive  $z$  direction. In order to provide an example of the exact lines that were included in the input files to define the burners and propane fires in this manner, the following lines were used in the Test 2 FDS input file to define surfaces with propane mass fluxes corresponding to the heat release rate of each burner:

```
&SURF ID='BURNER 1', MASS_FLUX(1)=0.0264, SPEC_ID(1)='PROPANE',
COLOR='RED', RAMP_MF(1)='burner1', TMP_FRONT=500. /
&SURF ID='BURNER 2', MASS_FLUX(1)=0.0246, SPEC_ID(1)='PROPANE',
COLOR='RED', RAMP_MF(1)='burner2', TMP_FRONT=500. /
```

```

&SURF ID='BURNER 3', MASS_FLUX(1)=0.0060, SPEC_ID(1)='PROPANE',
      COLOR='RED', RAMP_MF(1)='burner3', TMP_FRONT=500. /

```

Additionally, the following lines were used in the Test 2 input file to define each gas burner as having steel sides and a top surface with the specified propane mass flux from above:

```

&OBST XB= 0.60, 1.20, 4.90, 5.50, 0.00, 0.10,
      SURF_IDS='BURNER 1','STEEL PLATE','STEEL PLATE' /

&OBST XB= 0.60, 1.20, 4.30, 4.90, 0.00, 0.10,
      SURF_IDS='BURNER 2','STEEL PLATE','STEEL PLATE' /

&OBST XB= 0.60, 1.20, 3.70, 4.30, 0.00, 0.10,
      SURF_IDS='BURNER 3','STEEL PLATE','STEEL PLATE' /

&OBST XB= 0.60, 0.60, 3.70, 5.50, 0.10, 0.20,
      SURF_ID='STEEL PLATE' /

&OBST XB= 1.20, 1.20, 3.70, 5.50, 0.10, 0.20,
      SURF_ID='STEEL PLATE' /

&OBST XB= 0.60, 1.20, 3.70, 3.70, 0.10, 0.20,
      SURF_ID='STEEL PLATE' /

&OBST XB= 0.60, 1.20, 5.50, 5.50, 0.10, 0.20,
      SURF_ID='STEEL PLATE' /

```

The heat release rates listed in Table 3.1 from Chapter 3 were used to determine the values of propane mass flux to prescribe to the burners defined in the FDS input files for Tests 5–6 and Tests 22–25. The propane mass flux,  $\dot{m}_{C_3H_8}''$ , was calculated

using the equation

$$\dot{m}_{C_3H_8}'' = \frac{\dot{Q}}{A\Delta h_c} \quad (4.2)$$

in which  $\dot{Q}$  is the burner heat release rate;  $A$  is the area of the top surface of the burner,  $0.36 \text{ m}^2$  for all burners; and  $\Delta h_c$  is the effective heat of combustion of the fuel (propane), which was taken to be  $46334.6 \text{ kJ/kg}$  [REF?].

As mentioned in Chapter 3, the rate of propane flow to the burners was not able to be accurately measured for Tests 2–4. So, the heat release rates associated with the periods in which one, two, and three burners were ignited during Tests 2–4 were estimated using the fire room hot gas layer temperature in conjunction with the following correlation derived by McCaffrey, Quintiere, and Harkleroad (MQH) for compartment fires [?]:

$$T_g = 6.85 \left( \frac{\dot{Q}^2}{A_0 \sqrt{H_0} h_k A_T} \right)^{1/3} + T_\infty \quad (4.3)$$

$$\Rightarrow \dot{Q} = \left[ A_0 \sqrt{H_0} h_k A_T \left( \frac{T_g - T_\infty}{6.85} \right)^3 \right]^{1/2}$$

in which  $\dot{Q}$  is the heat release rate of the fire (kW),  $A_0$  is the area of the compartment opening ( $\text{m}^2$ ),  $H_0$  is the height of the compartment opening (m),  $h_k$  is the effective heat transfer coefficient ( $\text{kW}/(\text{m}^2\text{K})$ ),  $A_T$  is the total area of the compartment enclosing surfaces ( $\text{m}^2$ ),  $T_g$  is the temperature of the upper gas layer (K), and  $T_\infty$  is the ambient temperature (K). The hot gas layer temperatures were calculated using the data from the thermocouple arrays located in the fire room. The exact methodology of obtaining the hot gas layer temperature from the thermocouple data

is outlined in Chapter 5.

Using Equation 4.3, the estimated heat release rates for the periods with one, two, and three burners ignited were calculated and used to determine the propane mass flux values to assign to each burner in the FDS input files for Tests 2–4. Table 4.1 lists the heat release rates obtained from this method, rounded to the nearest 10.

Table 4.1: Tests 2–4 Heat Release Rates Estimated using the Average Hot Gas Layer Temperature and MQH Correlation.

<b>Test #</b>	<b>1 Burner Ignited</b>	<b>2 Burners Ignited</b>	<b>3 Burners Ignited</b>
2	440	850	950
3	520	940	1110
4	550	970	1130

The reaction mechanisms for combustion in all simulations were modeled using the default mixing-controlled, simple chemistry model (reaction rate is infinite and limited only by species concentrations) and specified via the following code:

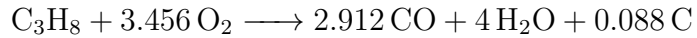
```
&REAC ID = 'R1'

FUEL = 'PROPANE'

SPEC_ID_NU='PROPANE','OXYGEN','CARBON MONOXIDE',
'WATER VAPOR','SOOT'

NU= -1,-3.456,2.912,4.0,0.088
```

which corresponds to the single-step reaction mechanism of



for propane. Additionally, the production of carbon dioxide was tracked via

```
&REAC ID = 'R2'

FUEL = 'CARBON MONOXIDE'

SPEC_ID_NU='CARBON MONOXIDE', 'OXYGEN', 'CARBON DIOXIDE'

NU= -1,-0.5,1{}

RADIATIVE_FRACTION=0.30
```

FDS has built-in properties for a number of different fuels, including PROPANE and CARBON MONOXIDE. Thus, it was not necessary to explicitly list thermophysical properties for the prescribed fuels. Nitrogen was used as the background species. Because of the presence of multiple chemical reactions, gas phase combustion was eliminated by setting SUPPRESSION=.FALSE. on the MISC line.

### 4.3 Additional Input Parameters

In addition to those presented in the previous sections of this chapter, a variety of other parameters were specified within the simulation input files. These include the ambient temperature, timing information, thermophysical properties of materials that weren't already predefined by FDS, leakage throughout the structure, and different devices to model the various types of instrumentation used during the physical experiments.

The ambient temperature was explicitly set in each input file based on the average temperature throughout the test structure before ignition, obtained by averaging the temperatures measured by the thermocouple arrays throughout the structure.

The ambient temperatures ranged from 35 °C to 62 °C. The variation in ambient temperatures is a result of the fact that some of the tests were conducted shortly after another fire experiment in the same structure, and thus some residual heat from the first test was present within the structure at the start of the next test.

The timing information that was specified within the FDS input files consisted of the simulation run time and event times presented in Figures 3.1–3.5 of Chapter 3, such as when different burners were ignited and vents opened or closed. The vents were modeled by first defining a hole via the **HOLE** namelist group at the location of the vent, setting an obstruction via the **OBST** namelist group to cover the hole at the start of the simulation, and assigning a control to the obstruction using the **CTRL** namelist group. The control was set to a timer **DEVC** and used a ramp function defined by the **RAMP** namelist group to change the **PERMIT\_HOLE** value for the obstruction from **.FALSE.** to **.TRUE.** at the time of the vent opening. For example, the following lines were included within the Test 2 FDS input file to initially define the north side, east double door as closed and then open the door at 538 s:

```

&HOLE XB=10.99,11.11, 2.10, 3.00, 0.00, 2.00
  / Cut-out for North-East Door

&OBST XB=11.00,11.10, 2.10, 3.00, 0.00, 2.00, SURF_ID='DOOR',
  PERMIT_HOLE=.FALSE., CTRL_ID='east controller'
  / North-East Door

&CTRL ID='east controller', FUNCTION_TYPE='CUSTOM',
  INPUT_ID='east timer', RAMP_ID='east cycle' /

```

```

&DEVC ID='east timer', QUANTITY='TIME', XYZ=0,0,0 /
&RAMP ID='east cycle', T= 0., F= 1 /
&RAMP ID='east cycle', T= 537., F= 1 /
&RAMP ID='east cycle', T= 538., F=-1 /

```

Four materials were explicitly defined via the **MATL** namelist group to assign to different surfaces within the simulation input files. The specific heat, thermal conductivity, and density of each material was defined by assigning appropriate values to the **SPECIFIC\_HEAT** (kJ/(kg·K)), **CONDUCTIVITY** (W/(m·K)), and **DENSITY** (kg/m<sup>3</sup>) parameters, respectively, within the corresponding **MATL** namelist group. For example, steel was defined by the lines

```

&MATL ID          = 'STEEL'
SPECIFIC_HEAT = 0.465
CONDUCTIVITY = 54.
DENSITY      = 7833. /

```

A complete list of the defined materials and corresponding properties are listed in Table 4.2. \*\*\*ADD REFs TO TABLE\*\*\*

Table 4.2: Various Materials Defined Within Each FDS Input File and the Corresponding MATL Namelist Group Parameter Values.

Material ID	SPECIFIC_HEAT (kJ/(kg·K))	CONDUCTIVITY (W/(m·K))	DENSITY (kg/m <sup>3</sup> )
Steel	0.465	54.0	7833
Gypsum	1.09	0.17	650
Concrete	1.04	1.8	2280
Fiber Cement	1.0	0.15	1300

The materials listed in Table 4.2 were explicitly specified within the FDS input files to ensure that the solid boundary surfaces throughout the model were properly defined to match the surface materials described in Chapter 2. For example, based on the description of the exterior walls from Chapter 2:

“The first floor of each structure had outer walls composed of interlocking concrete blocks measuring 0.6 m (2.0 ft) wide... Two layers of 16 mm (0.63 in) Type X gypsum board lined the steel studs, and a layer of 13 mm (0.5 in) thick Durock cement board covered the gypsum board.”

the surface of the exterior walls were defined in the FDS input file as

```

&SURF_ID          = 'EXTERIOR WALL'
DEFAULT           = .TRUE.
RGB               = 150,150,150
MATL_ID           = 'FIBER CEMENT', 'GYPSUM', 'CONCRETE'
THICKNESS         = 0.013,0.03,0.610 /

```

To account for the structure leakage described in Chapter 2, the pressure zone leakage approach outlined in the FDS User Guide [1] in which a leakage flow is

computed via the program’s HVAC model to capture bulk leakage through structure walls. This approach involves defining a pressure zone using the `ZONE` namelist group and assigning a leakage area via the `LEAK_AREA` quantity of the zone.

Various instrumentation devices can be modeled within FDS through the `DEVC` namelist group. Different devices were specified in the FDS input files at the sensor locations described in Chapter 2. The `QUANTITY` parameter within the `DEVC` namelist group was set based on the type of sensor being modeled. Table 4.3 lists each type of sensor that was modeled, its corresponding `QUANTITY` parameter, and the combined uncertainty associated with the `QUANTITY` parameter as given by the FDS Validation Guide.

Table 4.3: Instrumentation Specified within FDS Input File and Corresponding `DEVC` Namelist Group Properties.

Instrumentation Type	Assigned QUANTITY	Combined Uncertainty
Thermocouple	<code>'THERMOCOUPLE'</code>	7 %
Gas Concentration	<code>'VOLUME FRACTION'</code>	8 %
BDP	<code>'VELOCITY'</code>	8 %
Heat Flux Gauge	<code>'GAUGE HEAT FLUX'</code>	11 %

Finally, to model the PPV fan that was used after the burners were extinguished in Tests 2–4 and during Tests 22–25, an obstruction was created at the fan location and a surface was assigned to the front of the fan with a specified velocity normal to the side of the structure that was controlled by a timer and ramp, similar to the vent openings.

## Chapter 5: Results and Discussion

The plots presented in the following sections compare the predicted quantities output by FDS to the experimental data measured by instrumentation. First, the results of the mesh sensitivity study that was performed to determine an appropriate grid size for the simulations are presented and discussed. Then, the data from the FDS simulations are compared to the sensor data from the nine experiments. Two types of plots are included with the discussion for each type of measured quantity: one that shows the experimental data and FDS simulation data plotted over the duration of an experiment and a log/log scatter plot of the FDS data vs. the experimental data from all experiments along with some additional statistics to express the accuracy of the FDS models in predicting the specific quantity of interest. All plotted data were time-averaged over 10 seconds in order to smooth the raw data.

### 5.1 Mesh Sensitivity Studies

Figures 5.1–5.4 show the  $O_2$  volume fractions and ceiling jet temperatures output by FDS models with coarse, medium, and fine grid sizes for simulations of Tests 4 and 25.

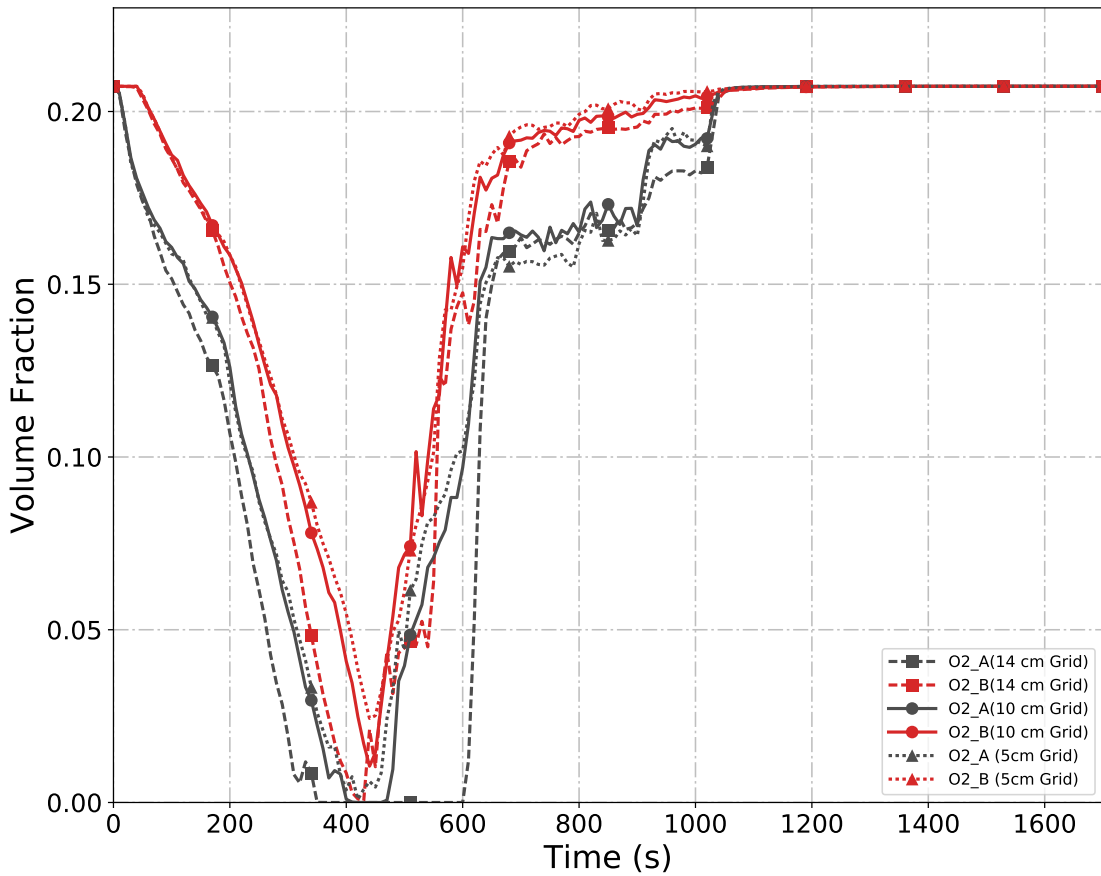


Figure 5.1:  $O_2$  concentrations output by the FDS simulations with various mesh sizes for Test 4 in the East Structure.

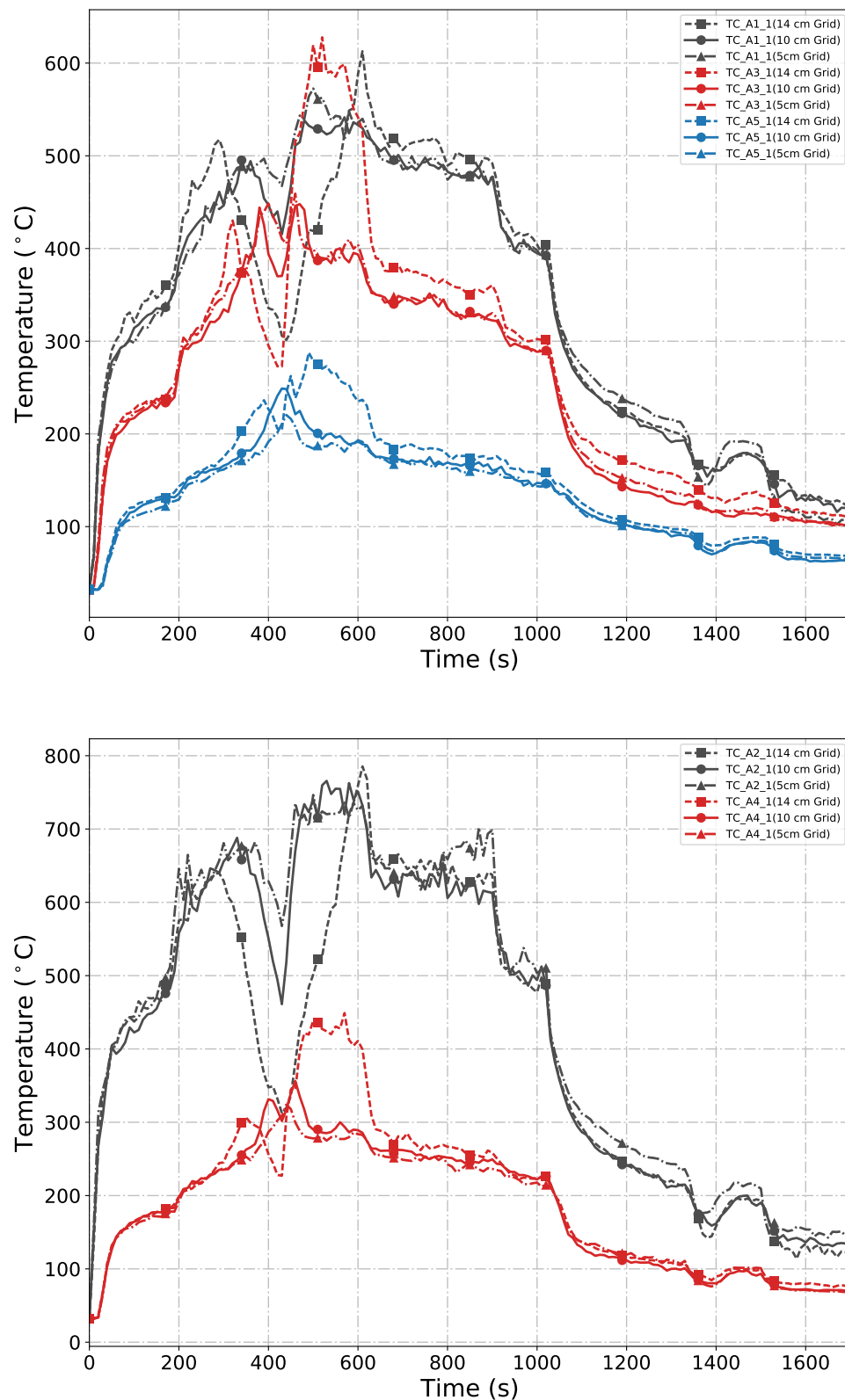


Figure 5.2: Ceiling jet temperatures output by the FDS simulations with various mesh sizes for Test 4 in the East Structure.

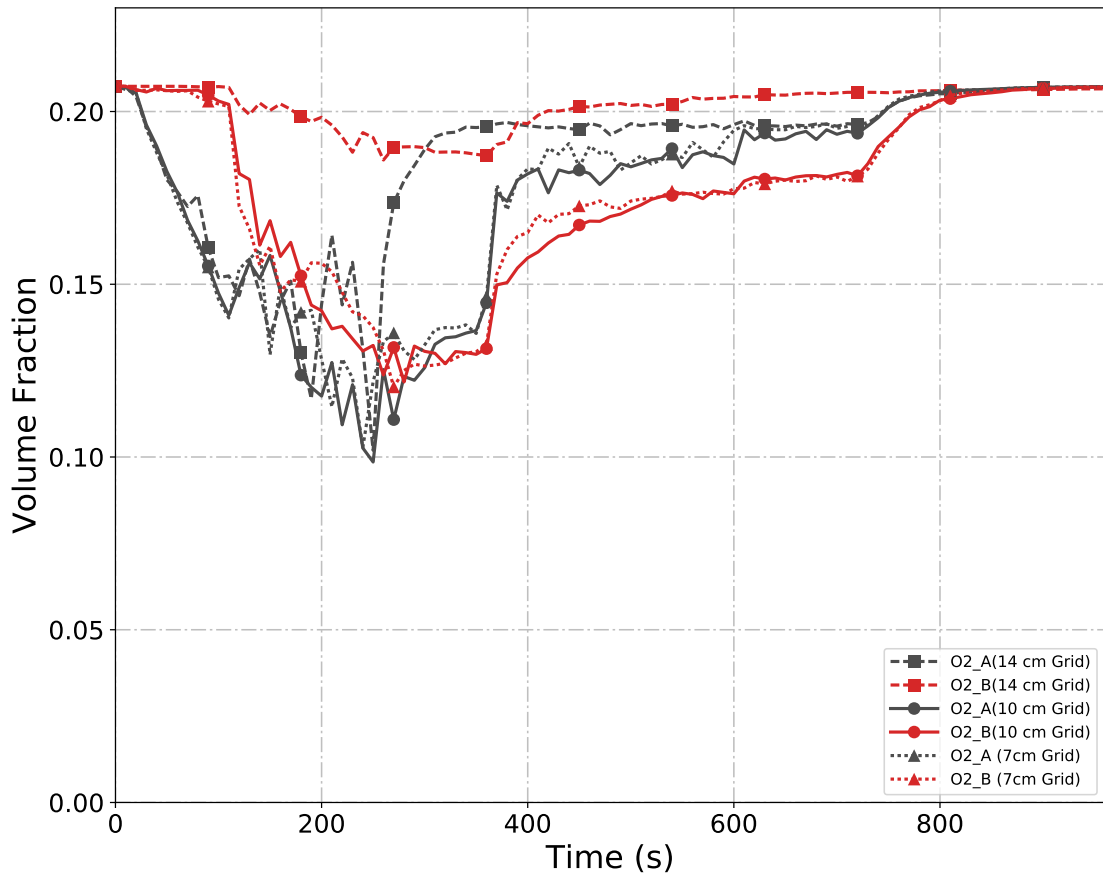


Figure 5.3:  $O_2$  concentrations output by the FDS simulations with various mesh sizes for Test 25 in the West Structure.

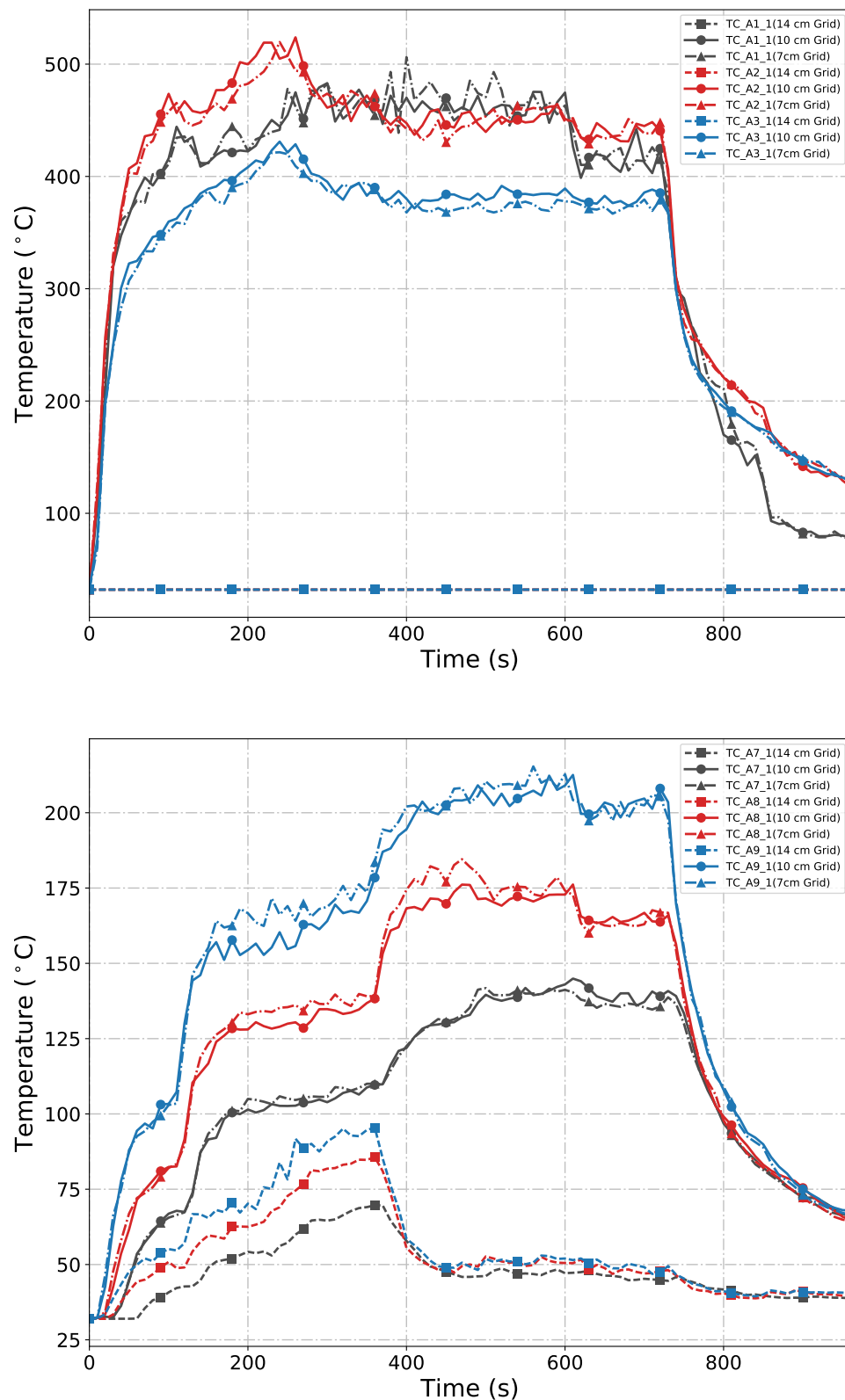


Figure 5.4: Ceiling jet temperatures output by the FDS simulations with various mesh sizes for Test 25 in the West Structure.

Looking at the plots presented above, significant changes in the model data exist when the grid size is reduced from 14 cm to 10 cm. Notice in Figure 5.4, the 14 cm grid was not refined enough to define the thermocouple locations at 0.03 m below the ceiling. Insignificant changes occur in the output data between the 10 cm grid size and the finer grid size of 5 cm for Test 4 and 7 cm for Test 25. These results suggest that a mesh size of 10 cm is appropriate for the FDS simulations of experiments in both the East and West Structures.

## 5.2 FDS Model Output Compared to Experimental Data

In the following subsections, the temperature, gas species concentration, gas velocity, and heat flux measurements predicted by the FDS simulations are compared to the corresponding sensor data measured during the propane burner experiments. Two different types of plots are presented in each section below.

First, a figure is presented in each section to show a comparison of sensor data from a specific test (solid line with circle markers) and the corresponding data output by FDS (dashed line with triangle markers). These types of plots were generated for data collected at each of the various measurement locations described in Chapter 2 for each experiment. Appendix B contains the remaining plots that compare the experimental data to the FDS data over the duration of each experiment.

The second type of plot that was generated for each discussed quantity is a log/log scatter plot designed to evaluate the model uncertainty in predicting the respective quantity. The plot is similiar to those found within the FDS Validation

guide [4]. The procedure followed to generate the plots and statistical data is briefly outlined below. Full details of the analysis are described in detail in by McGrattan and Toman in Ref. [18].

Taking  $M_i$  and  $E_i$  to represent the change in the value of a quantity from its ambient at a specific time based on the data output by the FDS simulation and measured by instrumentation during the experiment, respectively, the mean and standard deviation of the distribution can be estimated by first calculating

$$\overline{\ln(M/E)} = \frac{1}{n} \sum_{i=1}^n \ln\left(\frac{M_i}{E_i}\right) \quad (5.1)$$

Note, the natural log is used so that the variance of the random variable can be expressed in terms of the relative uncertainty. The assumption that  $\ln(M/E)$  is normally distributed has been tested for each data type of interest by the developers of FDS, and the results are shown in the FDS Validation Guide. The standard deviation of the logarithm of a normally distributed random variable is approximately equal to the standard deviation divided by its mean, the relative standard deviation. The least squares estimate of the standard deviation of the combined distribution is defined as:

$$\tilde{\sigma}_m^2 + \tilde{\sigma}_E^2 \approx \frac{1}{n-1} \sum_{i=1}^n \left[ \ln(M_i/E_i) - \overline{\ln(M/E)} \right]^2 \quad (5.2)$$

Using the pair of measured and predicted values with the known  $\tilde{\sigma}_E$ , the expression on the right can be evaluated. Eq. 5.2 imposes a constraint on the experimental

uncertainty value,  $\tilde{\sigma}_E$ , and in combination with a second constraint that  $\tilde{\sigma}_M$  cannot be less than  $\tilde{\sigma}_E$  because it's impossible to show that the model is more accurate than the measurements against which it's compared, the following is produced:

$$\tilde{\sigma}_E^2 \leq \frac{1}{2} \text{Var}(\ln(M/E)) \quad (5.3)$$

Using the mean of the distribution, an estimate of a bias factor,  $\delta$ , which expresses the tendency of the model to over or under-predict the measured quantity, can be found:

$$\delta \approx \exp\left(\overline{\ln(M/E)} + \frac{\tilde{\sigma}_M^2}{2} - \frac{\tilde{\sigma}_E^2}{2}\right) \quad (5.4)$$

The values of  $\delta$ ,  $\sigma_M$ , and  $\sigma_E$  are reported with each log/log plot in the following sections. For each plot, the solid red line and solid black line represent the expected values for  $M$  and  $E$ , respectively, and the dashed lines represent  $\pm\sigma$ , or standard deviations, of the corresponding color. Each plotted gray point on the log/log scatter plots was plotted based on the average values across the same 30 second experimental period calculated using the model (predicted) data and the experimental (measured) data. The only 30 second time periods for which points were plotted are those during which natural ventilation was the only type of ventilation (i.e., periods for which there was no PPV fan) and at least one gas burner was ignited. Table 5.1 in the final section of this chapter summarizes the calculated statistical values for each data type and how they compare to the same statistics contained in the FDS Validation Guide.

### 5.2.1 Temperature

#### *Hot Gas Layer*

A quantity that is commonly estimated for compartment fire scenarios is the location of the interface between the hot, smoke-laden upper layer and cooler, lower layer. Some fire models, such as two-zone models, calculate this value directly, along with the average temperature of the upper (hot gas) layer and lower layer. Being that it's a CFD model, FDS computes a continuous profile of temperature and thus, does not directly calculate the interface location or the average temperature of each layer. However, numerous techniques exist to estimate the layer height and average temperatures from a continuous vertical profile of temperature. The temperatures measured by the thermocouples in the vertical arrays throughout the experimental structures were used to define a vertical profile of temperature,  $T(z)$ , in which  $z$  is the height above the floor ( $z = 0$  at the floor and  $z = H$  at the room's ceiling). Then, the vertical temperature profile was used to estimate the hot gas layer temperature by a method developed by Janssens and Tran [19]. Taking  $T_u$  as the upper layer temperature,  $T_l$  as the lower layer temperature, and  $z_{int}$  as the hot gas layer interface height, the method is outlined below, starting with the calculation of the quantities  $I_1$  and  $I_2$

$$I_1 = \int_0^H T(z)dz = (H - z_{int})T_u + z_{int}T_l$$

$$I_2 = \int_0^H \frac{1}{T(z)}dz = (H - z_{int})\frac{1}{T_u} + z_{int}\frac{1}{T_l}$$

$I_1$  and  $I_2$  are then used to solve for  $z_{int}$  as follows

$$z_{int} = \frac{T_l(I_1 I_2 - H^2)}{I_1 + I_2 T_l^2 - 2T_l H} \quad (5.5)$$

$T_l$  is the temperature in the lowest mesh cell (or thermocouple) and  $T_u$  is the average upper layer temperature defined by

$$(H - z_{int})T_u = \int_{z_{int}}^H T(z)dz \quad (5.6)$$

Figure 5.5 shows the hot gas layer temperature derived from experimental data plotted with the same quantity derived from the FDS simulation data for Test 22, and Figure 5.6 shows the log/log scatter plot of the hot gas layer temperatures obtained from the predicted data from the FDS simulations compared to the values obtained by the measured data for the six applicable gas burner experiments.

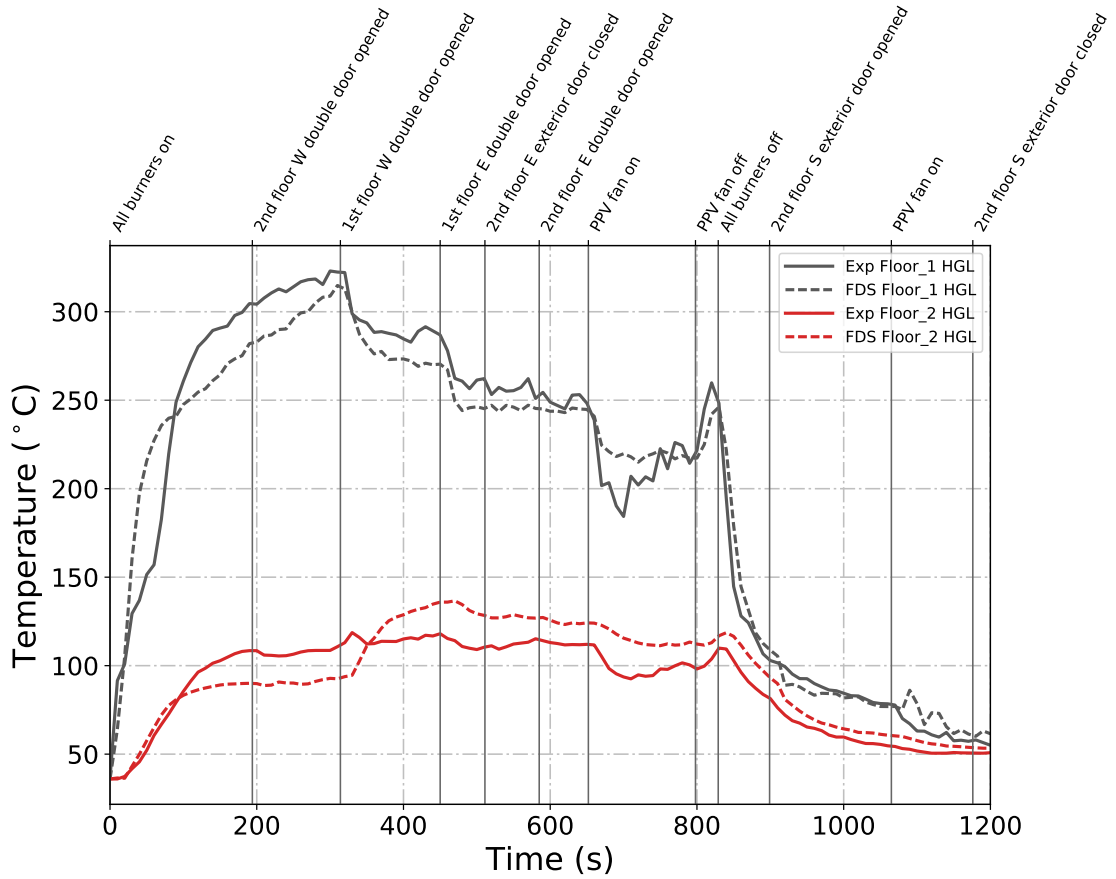


Figure 5.5: Plots of measured and predicted hot gas layer temperatures on the first and second floors of the West Structure during Test 22.

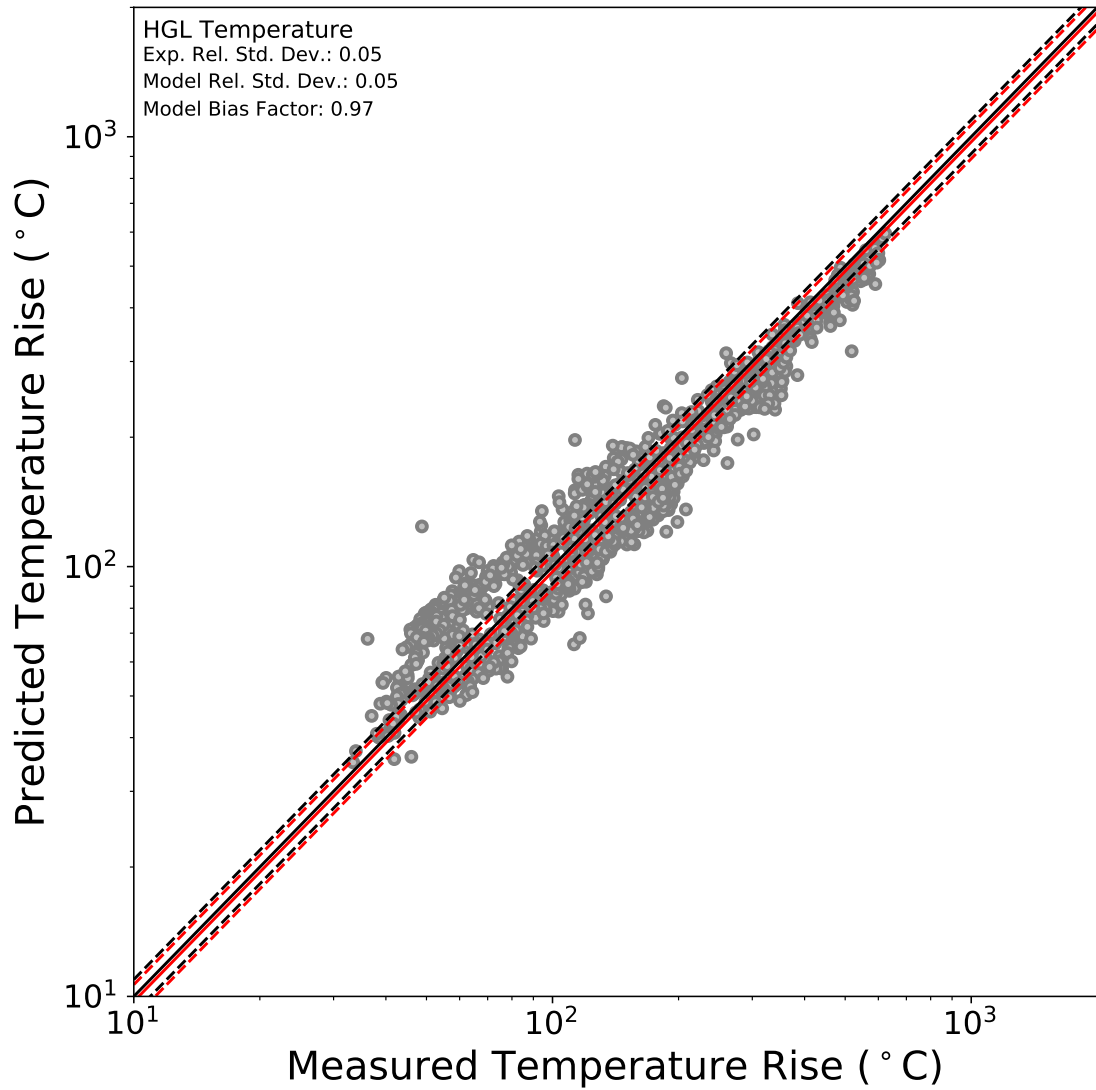


Figure 5.6: Summary of measured and predicted hot gas layer temperatures.

## *Ceiling Jet*

The temperature near the ceiling can be used to evaluate a model's ability to predict the activation times of sprinklers, smoke detectors, and other fire protection devices at ceiling height. The "ceiling jet" temperature used throughout this report refers to the temperature measured by the top thermocouple (closest to the ceiling) of the various thermocouple arrays located throughout the experimental structures. Figure 5.7 shows the ceiling jet temperatures measured during Test 4 plotted with the ceiling jet temperatures predicted by the FDS model for the same duration. Figure 5.8 shows the log/log scatter plot of the ceiling jet temperatures predicted by the FDS simulations compared to the corresponding measured ceiling jet temperatures for the six applicable gas burner experiments.

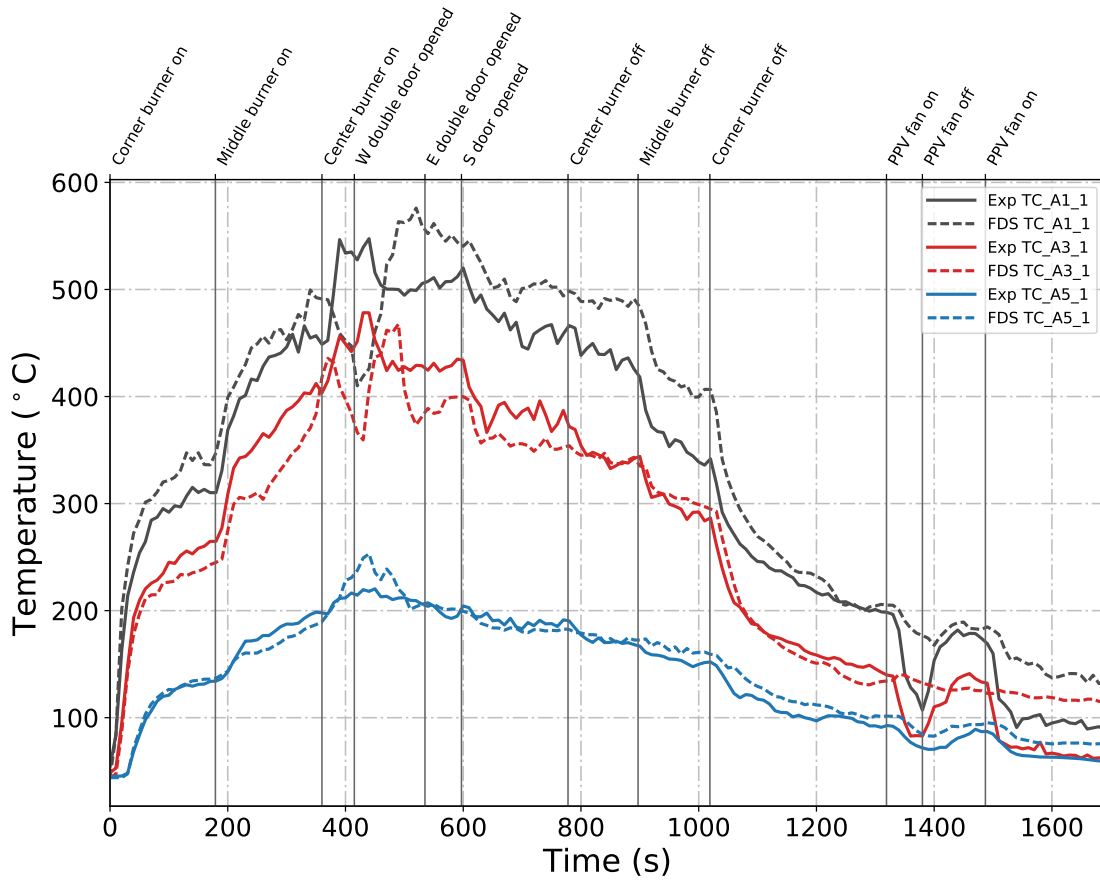


Figure 5.7: Plots of measured and predicted ceiling jet temperatures during Test 4 obtained from thermocouple arrays A1, A3, and A5 located in the fire room, middle room, and north room, respectively.

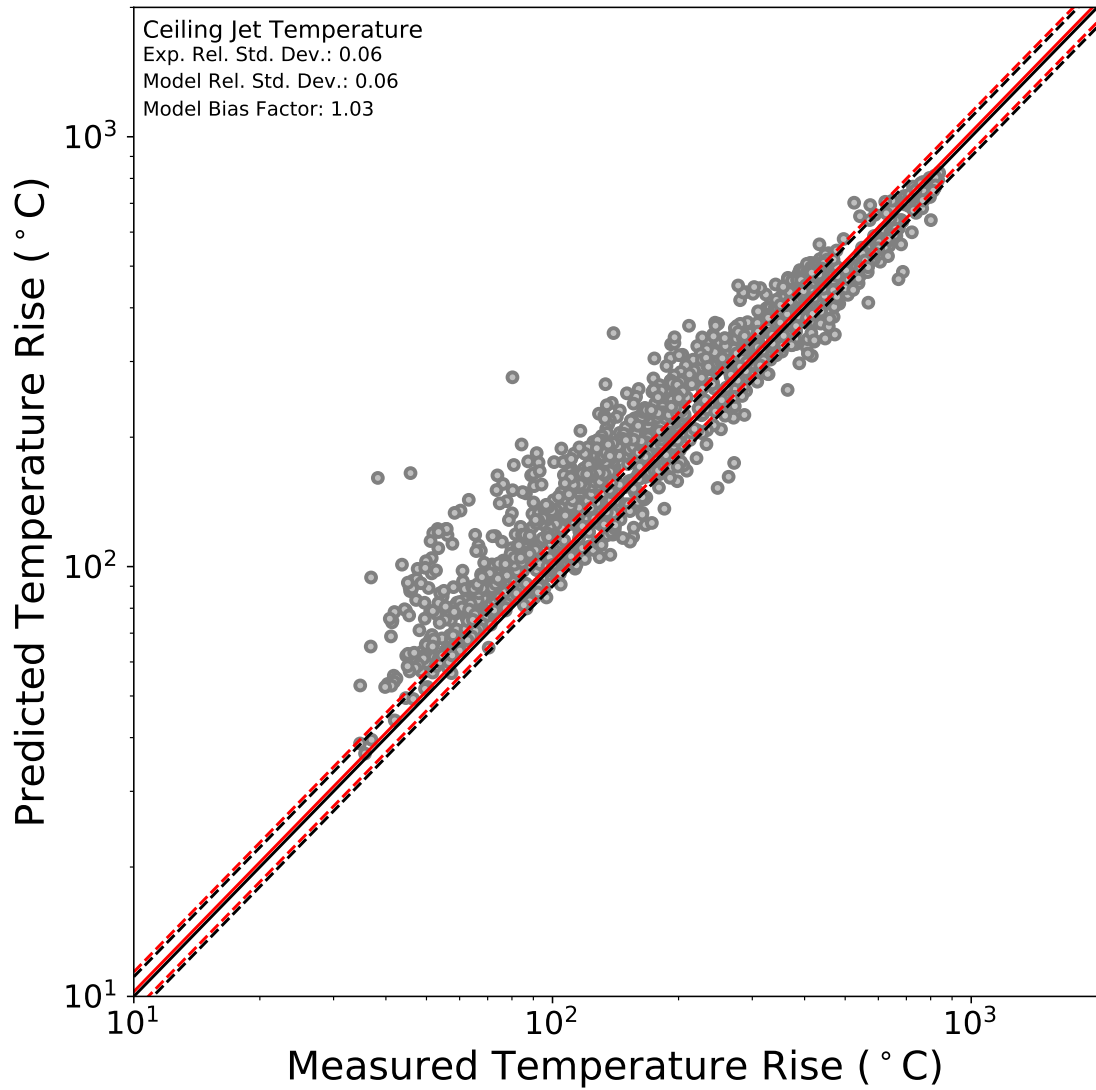


Figure 5.8: Summary of measured and predicted ceiling jet temperatures.

## *Thermocouple Arrays*

[PRESENT PLOTS SIMILAR TO HGL AND CEILING JET SECTIONS]

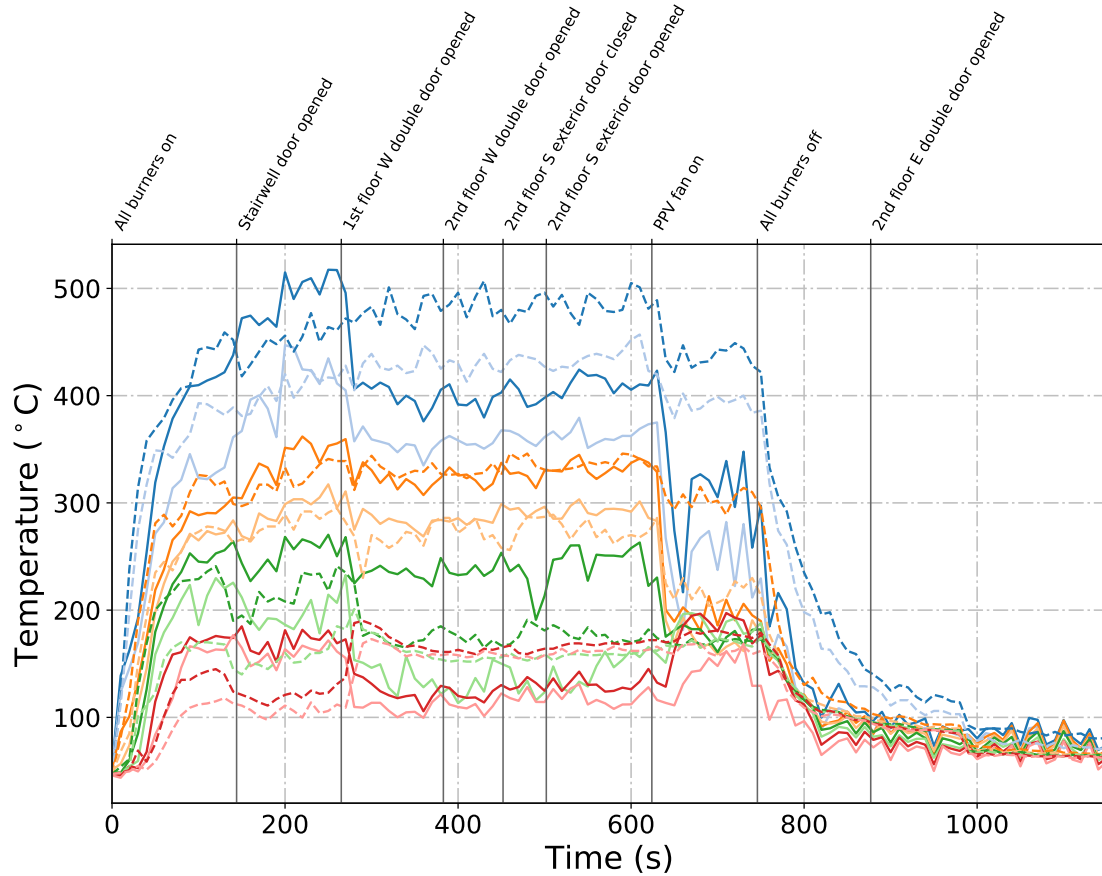


Figure 5.9: Plots of measured and predicted temperatures during Test 24 obtained from thermocouple array A1.

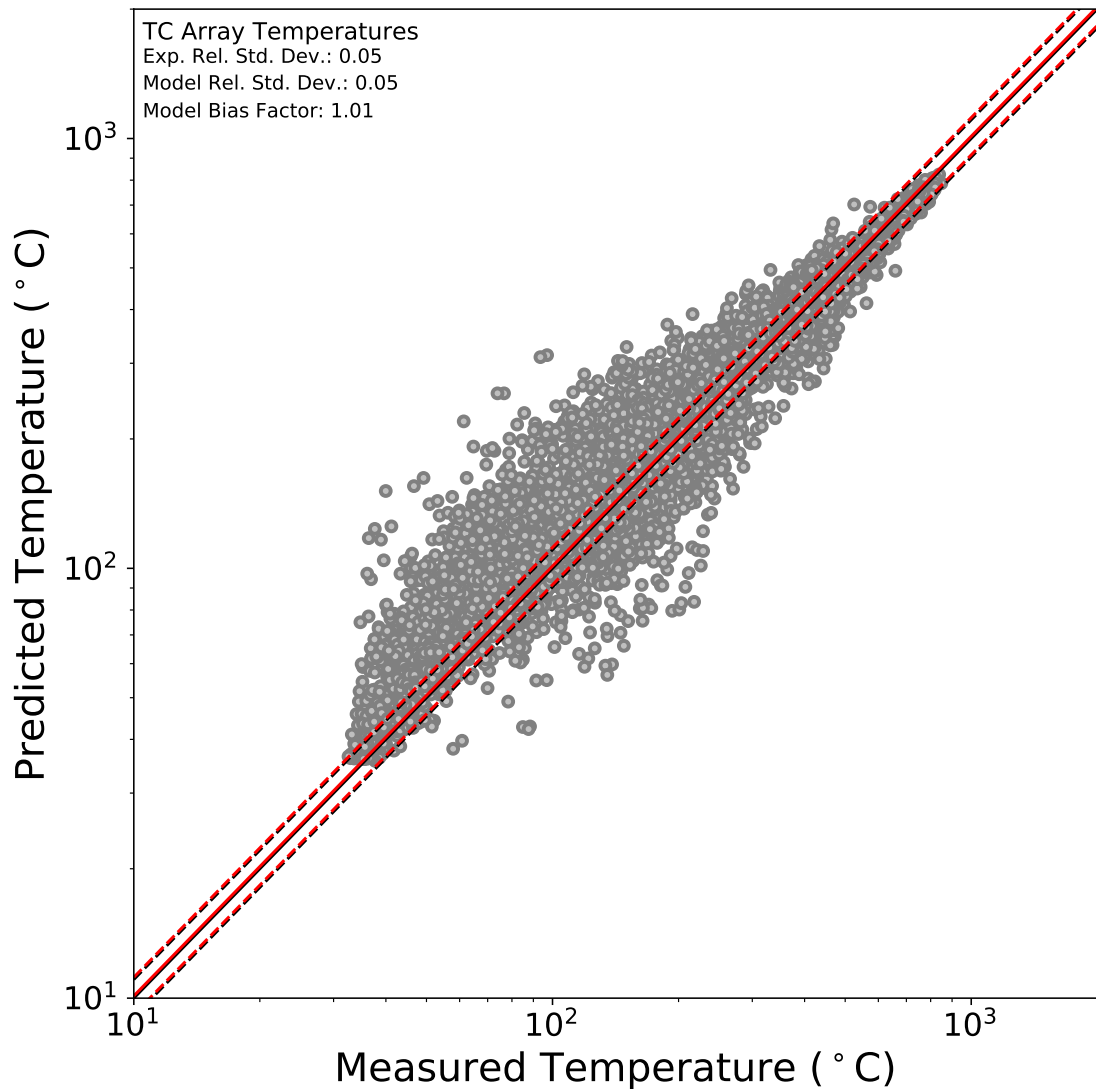


Figure 5.10: Summary of measured and predicted temperatures obtained from thermocouple arrays.

## 5.2.2 Gas Species Concentration

### $O_2$ Concentration

[PRESENT PLOTS SIMILAR TO HGL AND CEILING JET SECTIONS]

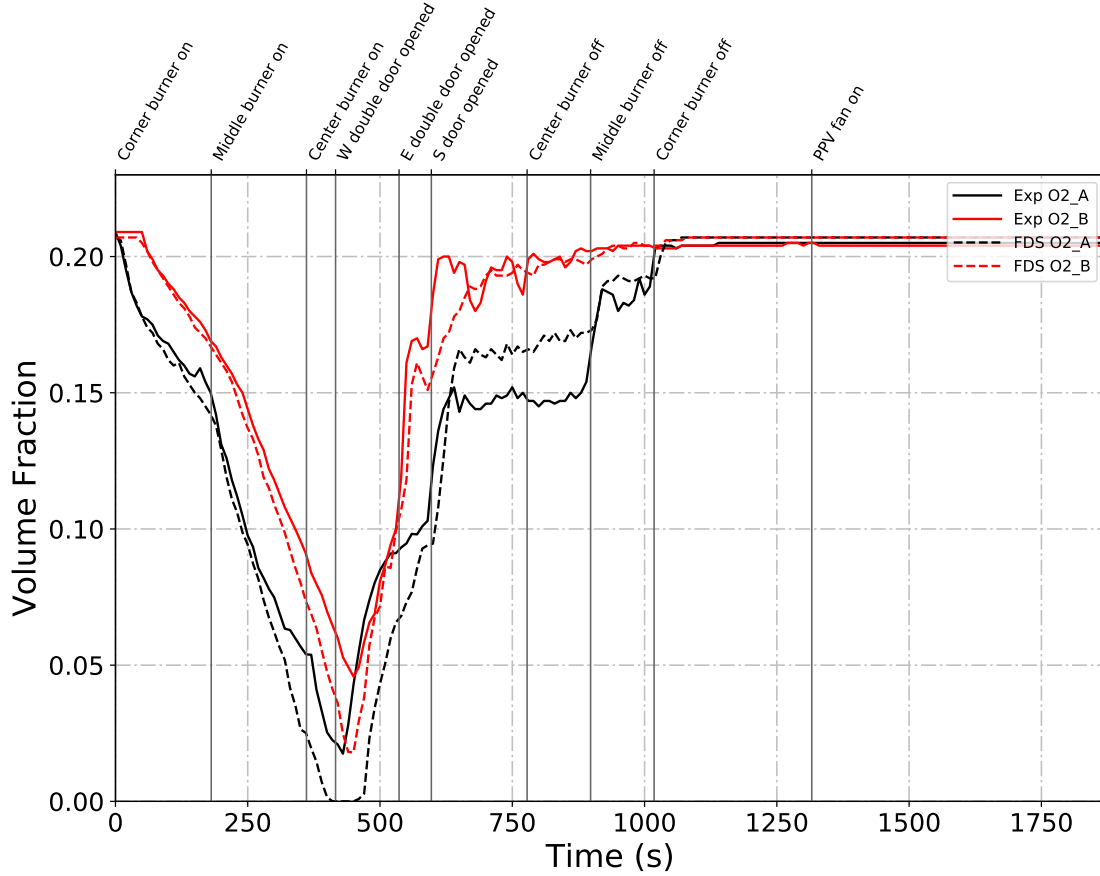


Figure 5.11: Plots of measured and predicted  $O_2$  concentration in the fire room (black plots) and north room (red plots) during Test 3.

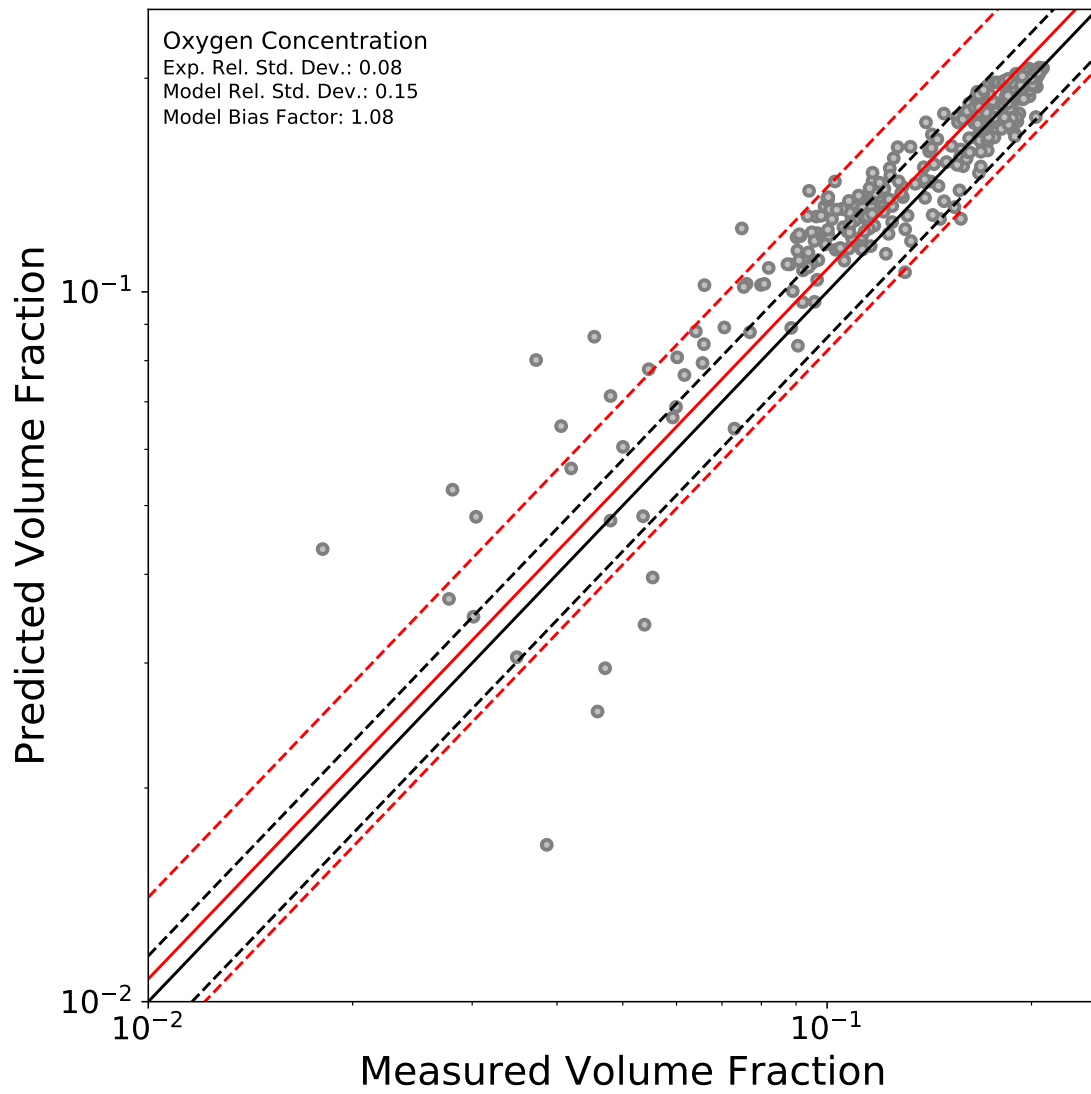


Figure 5.12: Summary of measured and predicted  $O_2$  concentrations.

## $CO_2$ Concentration

Note about maximum reading of 0.10 due to instrumentation. [PRESENT PLOTS SIMILAR TO HGL AND CEILING JET SECTIONS]

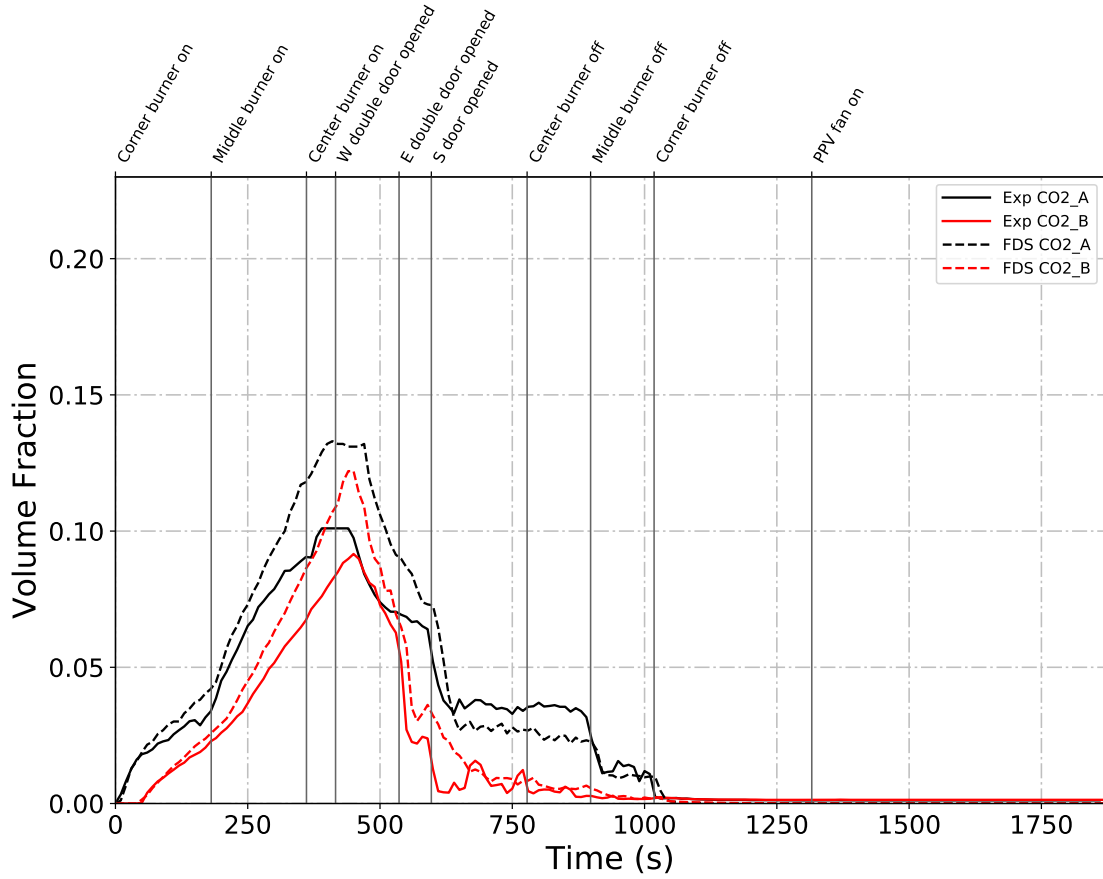


Figure 5.13: Plots of measured and predicted  $CO_2$  concentration in the fire room (black plots) and north room (red plots) during Test 3.

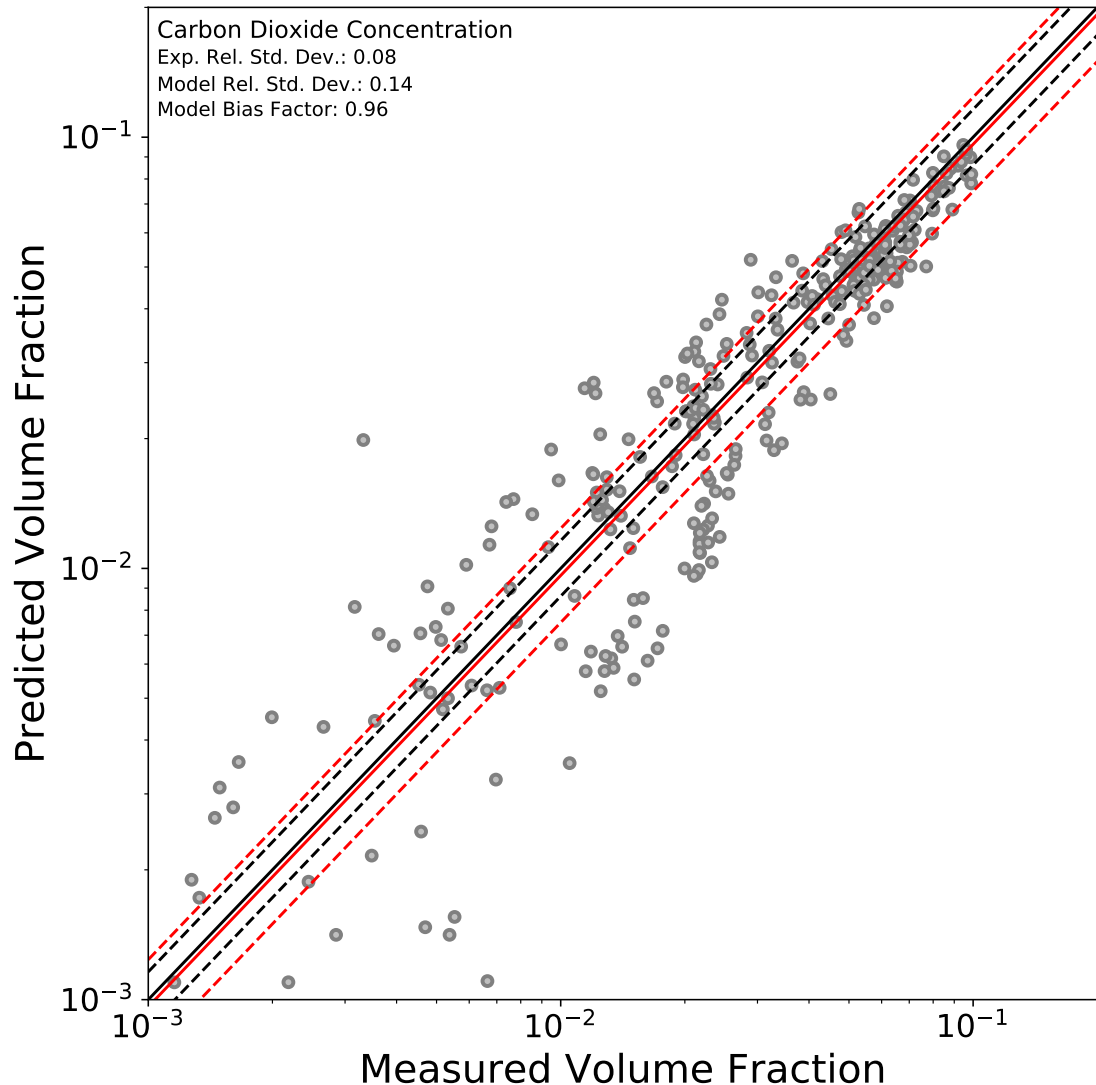


Figure 5.14: Summary of measured and predicted  $CO_2$  concentrations.

### 5.2.3 Gas Velocity

Because the gas burner experiments were conducted outdoors, they were subject to environmental conditions, such as wind. To minimize the effect such environmental conditions could have on the analysis of the results, the only gas velocity measurements that are considered in this section are those that were indoors, or well-protected from the exterior. The one gas velocity measurement location in the East Structure that was well-protected from the effects of environmental conditions is the location at the roof vent, the set of three BDPs at the location A10. Tests 5 and 6 were the only East Structure tests that incorporated the roof vent as a ventilation opening. Similarly, there was only one set of BDPs in the West Structure that was well protected from the exterior environment: the set of eight BDPs at the top of the stairs at measurement location A10. All four tests conducted in the West Structure used the stairwell door as a ventilation opening. For Tests 22 and 23, the door was in the open position the entire duration of the experiments, and for Tests 24 and 25, the door was opened at a point during the test. Only the measured and predicted data corresponding to when the door was in the open position is considered in the analysis below.

[PRESENT PLOTS SIMILAR TO HGL AND CEILING JET SECTIONS]

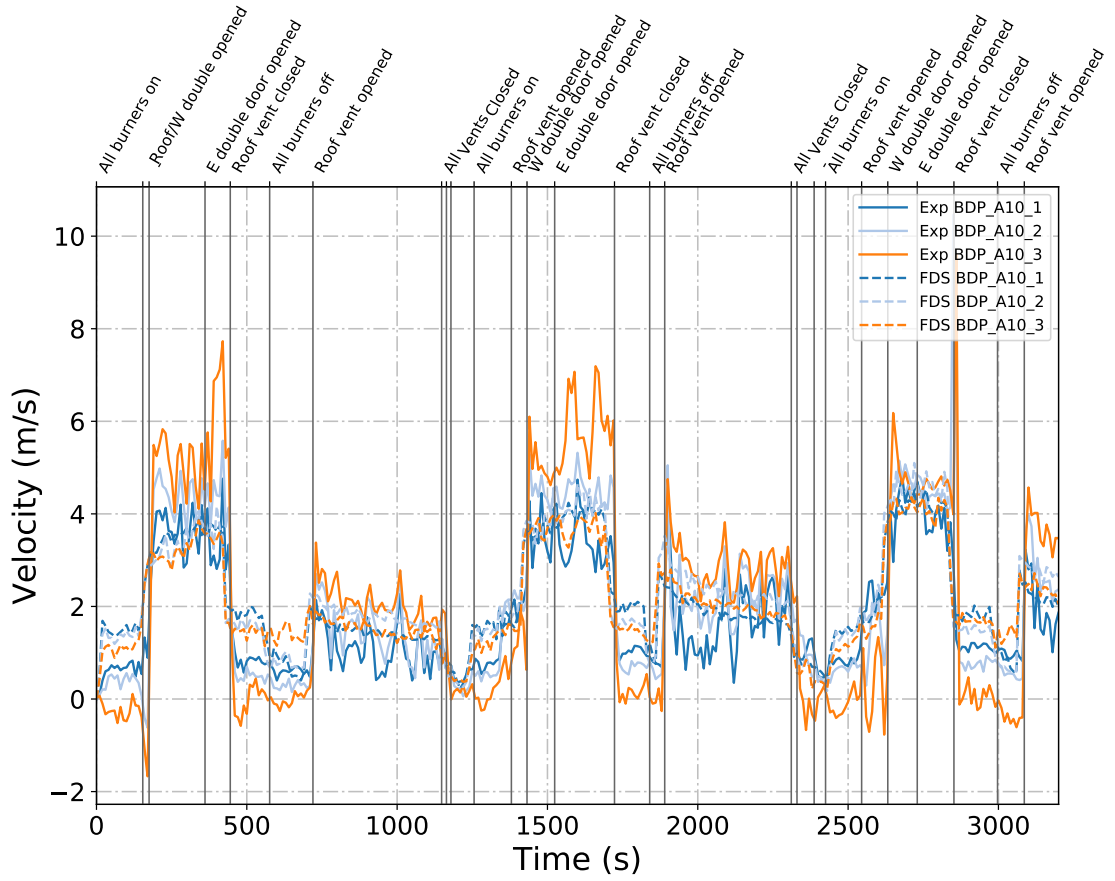


Figure 5.15: Plots of measured and predicted gas velocity through the roof vent during Test 5.

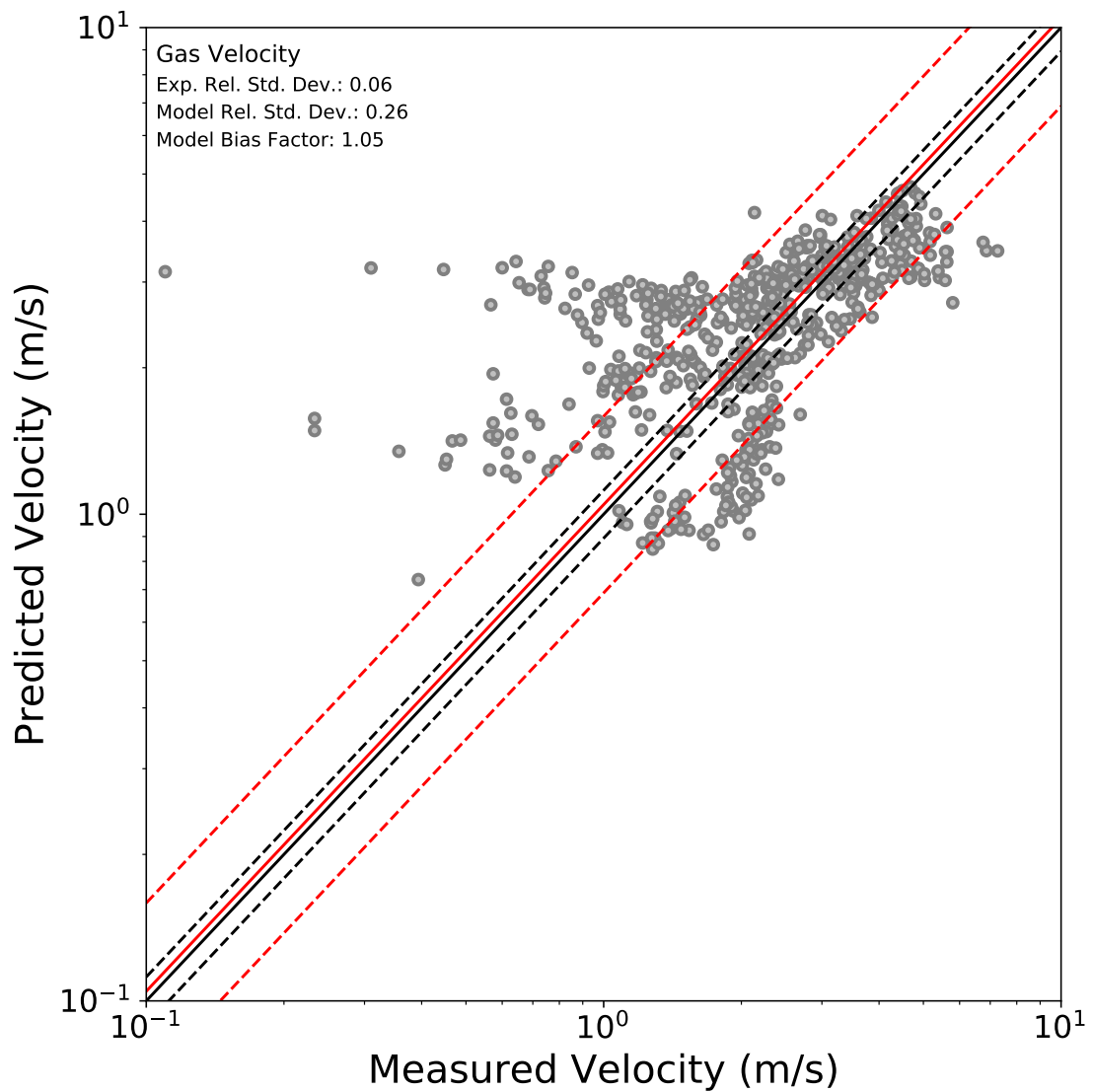


Figure 5.16: Summary of measured and predicted gas velocity measurements.

### 5.2.4 Total Heat Flux

[PRESENT PLOTS SIMILAR TO HGL AND CEILING JET SECTIONS]

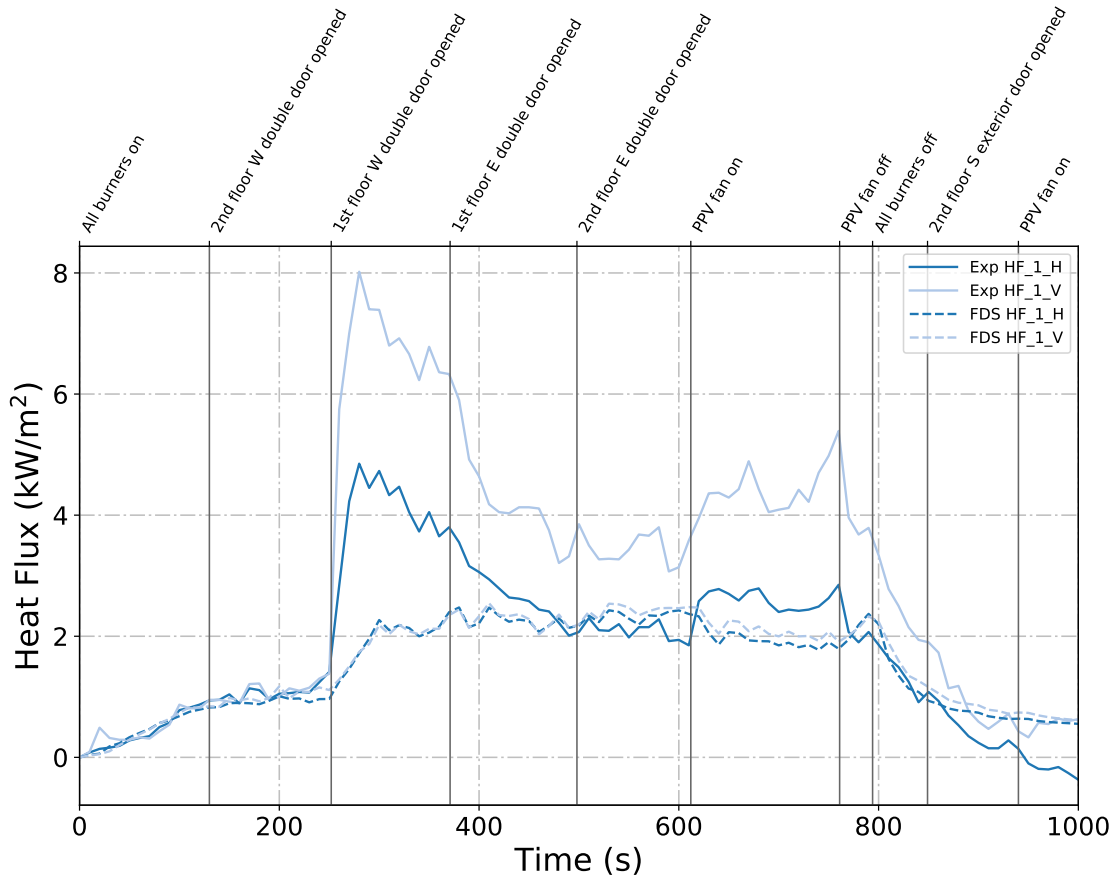


Figure 5.17: Plots of measured and predicted heat flux measured by total heat flux gauges at the top of the stairs facing the stair doorway ('H') and facing the ceiling ('V').

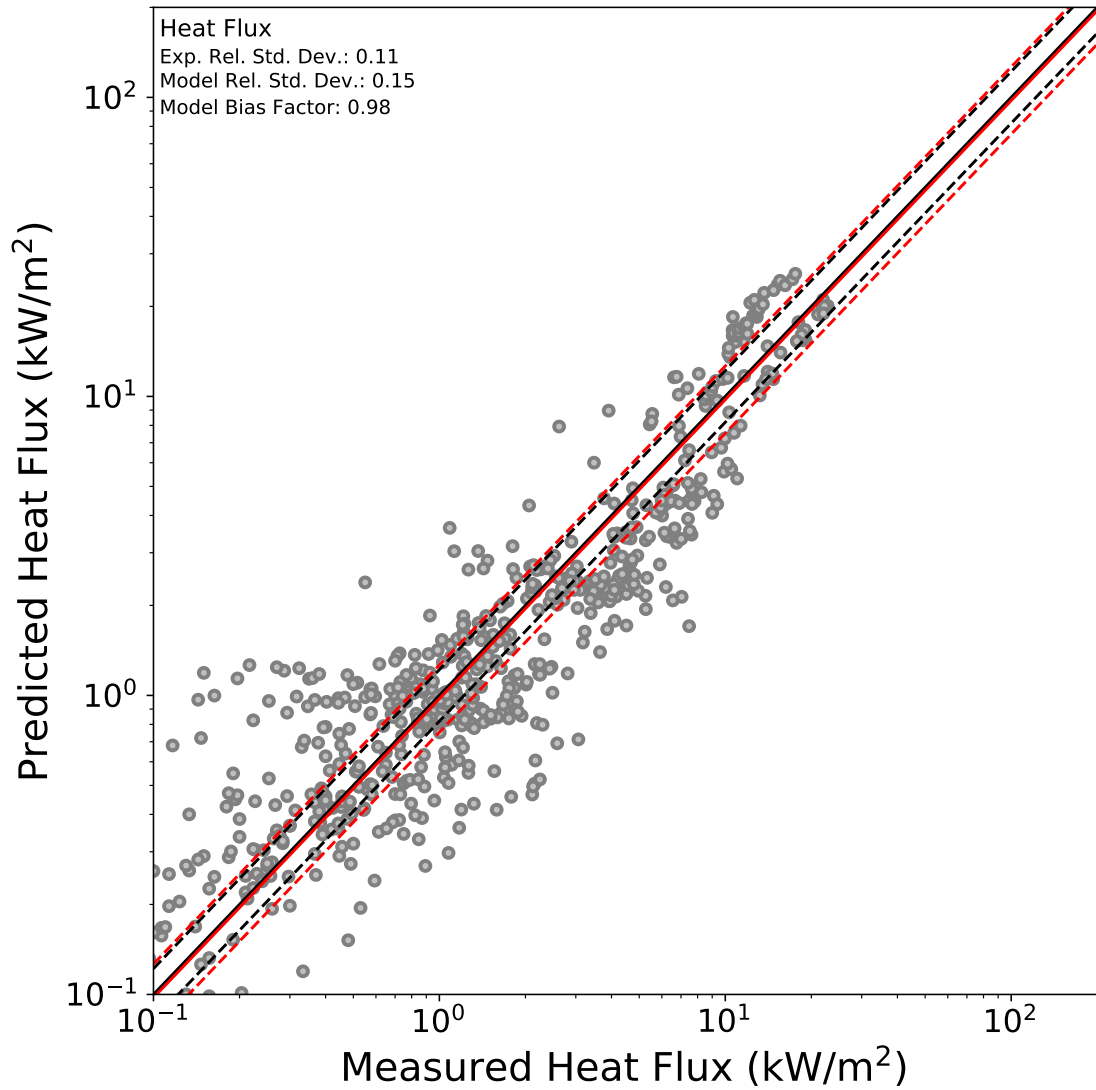


Figure 5.18: Summary of measured and predicted heat flux measurements.

### 5.2.5 Summary

Table 5.1 compares the model bias factor ( $\delta$ ), the experimental relative standard deviation ( $\sigma_E$ ), and model relative standard deviation ( $\sigma_M$ ) for each data quantity discussed above calculated across all appropriate time durations of the burner experiments to the same values that are listed in FDS Validation Guide for the corresponding data type based on all data within the FDS validation database.

Table 5.1: Comparison of Model Bias Factor ( $\delta$ ) and Relative Standard Deviation of Experimental Data ( $\sigma_E$ ) and Model Data ( $\sigma_M$ ) from all Tests and Same Values Listed in FDS Validation Guide for Each Data Type.

Quantity	<u>Calculated Values</u>			<u>FDS Validation Guide</u>		
	$\delta$	$\sigma_E$	$\sigma_M$	$\delta$	$\sigma_E$	$\sigma_M$
Hot Gas Layer Temperature	0.97	0.05	0.05	1.04	0.07	0.07
Ceiling Jet Temperature	1.03	0.06	0.06	1.04	0.07	0.13
Oxygen Concentration	1.08	0.08	0.15	0.99	0.08	0.14
Carbon Dioxide Concentration	0.96	0.08	0.14	1.00	0.08	0.12
Gas Velocity	1.05	0.06	0.26	0.99	0.08	0.09
Heat Flux	0.98	0.11	0.15	0.98	0.11	0.24

Overall, the agreement between the FDS simulation data and experimental data for the gas burner experiments is consistent with the statistical values given

by the FDS Validation Guide. For the hot gas layer temperature, ceiling jet temperature, and heat flux, the model bias calculated for the gas burner simulations is equal to or better than (closer to the ideal value of 1) the overall model bias values given by the FDS Validation Guide. Additionally, the relative standard deviations of the experimental data and model data for these three quantities are equal to or less than (better than) the corresponding values for the same data types listed in the validation guide.

The  $\delta$ ,  $\sigma_E$ , and  $\sigma_M$  values produced by the gas burner model and experimental data for both the  $O_2$  and  $CO_2$  gas concentrations were very close to the values documented in the FDS Validation Guide. The  $\sigma_E$  values are equal in both comparisons and the  $\sigma_M$  values are greater in magnitude by only 0.01 and 0.02 compared to the validation guide values for oxygen and carbon dioxide concentration, respectively. Finally, based on the data from gas burner simulations, the oxygen concentration model bias is worse (further from the ideal value of 1) by 7 % and carbon dioxide concentration model bias is worse by 4 % compared to the documented values in the FDS Validation Guide.

The most significant discrepancy between the documented values and values from the gas burner models is seen in the gas velocity comparison, in which  $\sigma_M$  was calculated as being greater than the  $\sigma_M$  from the validation guide by a value 0.18. This discrepancy may exist for a few of reasons. First, gas velocity was one of the quantities with the highest uncertainty associated with the experimental measurements. Also, as previously mentioned, the experiments were conducted outdoors, so environmental conditions may have affected the measurements, even

though only data from BDPs that were fully inside the structures were considered. Almost all ([CHECK VALIDATION GUIDE FOR EXACT NUMBER]) the tests used to calculate the  $\delta$ ,  $\sigma_E$ , and  $\sigma_M$  within the validation guide were conducted in a laboratory setting, which could explain the significantly smaller model relative standard deviation. Finally, due to the nature of the fire environment at the time of the measurements, it's possible that turbulent flow was occurring through the vents (especially the roof vent in Tests 5 and 6) at the time of the measurements. LES CFD models, like FDS, tend to be limited more in terms of accurately measuring turbulent flow than compared to measurements during other conditions.

## Chapter 6: Conclusion

Nine full-scale fire tests were conducted in two residential-sized structures. Five of the experiments occurred in a single-story structure with three different rooms, and the other four experiments were performed in a two-story structure with the ground level having an open floor plan and the second level having two rooms and a hallway. The fire source for each experiment was provided by a set of three diffusion flame burners with propane as the fuel. Various doors and vents were opened and closed during each test to change ventilation within the structure. Local measurements of temperature, gas velocity, heat flux, and gas concentrations were collected at various locations throughout the structure during the experiments.

The dimensions of each structure were carefully measured, and their construction materials were well-defined. The locations of the experimental instrumentation were also measured and the times of different experimental events were recorded. Additionally, the total volume of propane delivered to the burners was measured by a rotary gas meter and was used to calculate the heat release rate of the fire during each test. Using this information as input data, simulations of the experiments were created and executed using the CFD program Fire Dynamics Simulator developed by NIST. The simulation results were compared to the experimental data from the

experiments.

The agreement between the FDS simulation data and experimental data for the gas burner experiments is consistent with the statistical values given by the FDS Validation Guide. For the quantities of hot gas layer temperature, ceiling jet temperature, and heat flux, the model bias value was equal to or better than (closer to the ideal value of 1) the overall model bias values given by the FDS Validation Guide. Similarly, the relative standard deviations of the experimental data and model data were equal to or less than (more accurate) the corresponding values for the same data types listed in the validation guide. The model bias and experimental and model relative standard deviations produced for both the  $O_2$  and  $CO_2$  gas concentrations were very close to or better than the values documented in the FDS Validation Guide. The most significant discrepancy between the documented values and values from the gas burner models was seen in the gas velocity comparison. The difference could be a result of the fact that the tests were conducted outdoors, that the instrumentation used to measure gas velocity had a relatively large uncertainty range, and/or the limitations of LES models like FDS to model turbulent gas flow at a fine resolution.

Overall, the comparison of the simulation data to the experimental data suggests that the accuracy of the FDS models of the gas burner experiments in residential-scale structures is sufficient and comparable to the accuracy of other FDS models of different fire scenarios described in the FDS Validation Guide.

## Appendix A: Channel Lists

### A.1 East Structure

Table A.1: East Structure Channel List

<b>Device Location</b>	<b>Channel Name</b>	<b>Channel Location</b>	<b>Measurement Type</b>
<b>A1</b>	TC_A1_1	0.03 m below ceiling	Temperature
	TC_A1_2	0.30 m below ceiling	Temperature
	TC_A1_3	0.61 m below ceiling	Temperature
	TC_A1_4	0.91 m below ceiling	Temperature
	TC_A1_5	1.22 m below ceiling	Temperature
	TC_A1_6	1.52 m below ceiling	Temperature
	TC_A1_7	1.83 m below ceiling	Temperature
	TC_A1_8	2.13 m below ceiling	Temperature
	HF_A1	0.15 m above floor	Total heat flux
	RAD_A1	0.15 m above floor	Radiative heat flux
<b>A2</b>	CO_A	1.22 m above floor	CO concentration
	CO2_A	1.22 m above floor	CO <sub>2</sub> concentration
	O2_A	1.22 m above floor	O <sub>2</sub> concentration
	TC_A2_1	0.03 m below ceiling	Temperature
	TC_A2_2	0.30 m below ceiling	Temperature
	TC_A2_3	0.61 m below ceiling	Temperature
	TC_A2_4	0.91 m below ceiling	Temperature
	TC_A2_5	1.22 m below ceiling	Temperature
	TC_A2_6	1.52 m below ceiling	Temperature
	TC_A2_7	1.83 m below ceiling	Temperature
	TC_A2_8	2.13 m below ceiling	Temperature
	HF_A2	0.15 m above floor	Total heat flux
	RAD_A2	0.15 m above floor	Radiative heat flux

Table A.1: East Structure Channel List (continued)

Device Location	Channel Name	Channel Location	Measurement Type
A3	TC_A3_1	0.03 m below ceiling	Temperature
	TC_A3_2	0.30 m below ceiling	Temperature
	TC_A3_3	0.61 m below ceiling	Temperature
	TC_A3_4	0.91 m below ceiling	Temperature
	TC_A3_5	1.22 m below ceiling	Temperature
	TC_A3_6	1.52 m below ceiling	Temperature
	TC_A3_7	1.83 m below ceiling	Temperature
	TC_A3_8	2.13 m below ceiling	Temperature
	HF_A3	0.15 m above floor	Total heat flux
	RAD_A3	0.15 m above floor	Radiative heat flux
A4	TC_A4_1	0.03 m below ceiling	Temperature
	TC_A4_2	0.30 m below ceiling	Temperature
	TC_A4_3	0.61 m below ceiling	Temperature
	TC_A4_4	0.91 m below ceiling	Temperature
	TC_A4_5	1.22 m below ceiling	Temperature
	TC_A4_6	1.52 m below ceiling	Temperature
	TC_A4_7	1.83 m below ceiling	Temperature
	TC_A4_8	2.13 m below ceiling	Temperature
	HF_A4	0.15 m above floor	Total heat flux
	RAD_A4	0.15 m above floor	Radiative heat flux
A5	CO_B	1.22 m above floor	CO concentration
	CO2_B	1.22 m above floor	CO <sub>2</sub> concentration
	O2_B	1.22 m above floor	O <sub>2</sub> concentration
	TC_A5_1	0.03 m below ceiling	Temperature
	TC_A5_2	0.30 m below ceiling	Temperature
	TC_A5_3	0.61 m below ceiling	Temperature
	TC_A5_4	0.91 m below ceiling	Temperature
	TC_A5_5	1.22 m below ceiling	Temperature
	TC_A5_6	1.52 m below ceiling	Temperature
	TC_A5_7	1.83 m below ceiling	Temperature
	TC_A5_8	2.13 m below ceiling	Temperature
A5	HF_A5	0.15 m above floor	Total heat flux
	RAD_A5	0.15 m above floor	Radiative heat flux

Table A.1: East Structure Channel List (continued)

Device Location	Channel Name	Channel Location	Measurement Type
A7	TC_A7_1	0.08 m below soffit	Temperature
	TC_A7_2	0.34 m below soffit	Temperature
	TC_A7_3	0.61 m below soffit	Temperature
	TC_A7_4	0.88 m below soffit	Temperature
	TC_A7_5	1.15 m below soffit	Temperature
	TC_A7_6	1.42 m below soffit	Temperature
	TC_A7_7	1.68 m below soffit	Temperature
	TC_A7_8	1.95 m below soffit	Temperature
	BDP_A7_1	0.08 m below soffit	Velocity
	BDP_A7_2	0.34 m below soffit	Velocity
	BDP_A7_3	0.61 m below soffit	Velocity
	BDP_A7_4	0.88 m below soffit	Velocity
	BDP_A7_5	1.15 m below soffit	Velocity
	BDP_A7_6	1.42 m below soffit	Velocity
	BDP_A7_7	1.68 m below soffit	Velocity
	BDP_A7_8	1.95 m below soffit	Velocity
A8	TC_A8_1	0.08 m below soffit	Temperature
	TC_A8_2	0.34 m below soffit	Temperature
	TC_A8_3	0.61 m below soffit	Temperature
	TC_A8_4	0.88 m below soffit	Temperature
	TC_A8_5	1.15 m below soffit	Temperature
	TC_A8_6	1.42 m below soffit	Temperature
	TC_A8_7	1.68 m below soffit	Temperature
	TC_A8_8	1.95 m below soffit	Temperature
	BDP_A8_1	0.08 m below soffit	Velocity
	BDP_A8_2	0.34 m below soffit	Velocity
	BDP_A8_3	0.61 m below soffit	Velocity
	BDP_A8_4	0.88 m below soffit	Velocity
	BDP_A8_5	1.15 m below soffit	Velocity
	BDP_A8_6	1.42 m below soffit	Velocity
	BDP_A8_7	1.68 m below soffit	Velocity
	BDP_A8_8	1.95 m below soffit	Velocity

Table A.1: East Structure Channel List (continued)

Device Location	Channel Name	Channel Location	Measurement Type
A9	TC_A9_1	0.08 m below soffit	Temperature
	TC_A9_2	0.34 m below soffit	Temperature
	TC_A9_3	0.61 m below soffit	Temperature
	TC_A9_4	0.88 m below soffit	Temperature
	TC_A9_5	1.15 m below soffit	Temperature
	TC_A9_6	1.42 m below soffit	Temperature
	TC_A9_7	1.68 m below soffit	Temperature
	TC_A9_8	1.95 m below soffit	Temperature
	BDP_A9_1	0.08 m below soffit	Velocity
	BDP_A9_2	0.34 m below soffit	Velocity
	BDP_A9_3	0.61 m below soffit	Velocity
	BDP_A9_4	0.88 m below soffit	Velocity
	BDP_A9_5	1.15 m below soffit	Velocity
	BDP_A9_6	1.42 m below soffit	Velocity
	BDP_A9_7	1.68 m below soffit	Velocity
	BDP_A9_8	1.95 m below soffit	Velocity
A10	TC_A10_1	0.91 m from S side of vent	Temperature
	TC_A10_2	0.61 m from S side of vent	Temperature
	TC_A10_3	0.30 m from S side of vent	Temperature
	BDP_A10_1	0.91 m from S side of vent	Velocity
	BDP_A10_2	0.61 m from S side of vent	Velocity
	BDP_A10_3	0.30 m from S side of vent	Velocity

## A.2 West Structure

Table A.2: West Structure Channel List

<b>Device Location</b>	<b>Channel Name</b>	<b>Channel Location</b>	<b>Measurement Type</b>
<b>A1</b>	TC_A1_1	0.03 m below ceiling	Temperature
	TC_A1_2	0.30 m below ceiling	Temperature
	TC_A1_3	0.61 m below ceiling	Temperature
	TC_A1_4	0.91 m below ceiling	Temperature
	TC_A1_5	1.22 m below ceiling	Temperature
	TC_A1_6	1.52 m below ceiling	Temperature
	TC_A1_7	1.83 m below ceiling	Temperature
	TC_A1_8	2.13 m below ceiling	Temperature
	CO_A	1.22 m above floor	CO concentration
	CO2_A	1.22 m above floor	CO <sub>2</sub> concentration
	O2_A	1.22 m above floor	O <sub>2</sub> concentration
<b>A2</b>	TC_A2_1	0.03 m below ceiling	Temperature
	TC_A2_2	0.30 m below ceiling	Temperature
	TC_A2_3	0.61 m below ceiling	Temperature
	TC_A2_4	0.91 m below ceiling	Temperature
	TC_A2_5	1.22 m below ceiling	Temperature
	TC_A2_6	1.52 m below ceiling	Temperature
	TC_A2_7	1.83 m below ceiling	Temperature
	TC_A2_8	2.13 m below ceiling	Temperature
<b>A3</b>	TC_A3_1	0.03 m below ceiling	Temperature
	TC_A3_2	0.30 m below ceiling	Temperature
	TC_A3_3	0.61 m below ceiling	Temperature
	TC_A3_4	0.91 m below ceiling	Temperature
	TC_A3_5	1.22 m below ceiling	Temperature
	TC_A3_6	1.52 m below ceiling	Temperature
	TC_A3_7	1.83 m below ceiling	Temperature
	TC_A3_8	2.13 m below ceiling	Temperature

Table A.2: West Structure Channel List (continued)

Device Location	Channel Name	Channel Location	Measurement Type
A5	TC_A5_1	0.08 m below soffit	Temperature
	TC_A5_2	0.34 m below soffit	Temperature
	TC_A5_3	0.61 m below soffit	Temperature
	TC_A5_4	0.88 m below soffit	Temperature
	TC_A5_5	1.15 m below soffit	Temperature
	TC_A5_6	1.42 m below soffit	Temperature
	TC_A5_7	1.68 m below soffit	Temperature
	TC_A5_8	1.95 m below soffit	Temperature
	BDP_A5_1	0.08 m below soffit	Velocity
	BDP_A5_2	0.34 m below soffit	Velocity
	BDP_A5_3	0.61 m below soffit	Velocity
	BDP_A5_4	0.88 m below soffit	Velocity
	BDP_A5_5	1.15 m below soffit	Velocity
	BDP_A5_6	1.42 m below soffit	Velocity
	BDP_A5_7	1.68 m below soffit	Velocity
	BDP_A5_8	1.95 m below soffit	Velocity
A6	TC_A6_1	0.08 m below soffit	Temperature
	TC_A6_2	0.34 m below soffit	Temperature
	TC_A6_3	0.61 m below soffit	Temperature
	TC_A6_4	0.88 m below soffit	Temperature
	TC_A6_5	1.15 m below soffit	Temperature
	TC_A6_6	1.42 m below soffit	Temperature
	TC_A6_7	1.68 m below soffit	Temperature
	TC_A6_8	1.95 m below soffit	Temperature
	BDP_A6_1	0.08 m below soffit	Velocity
	BDP_A6_2	0.34 m below soffit	Velocity
	BDP_A6_3	0.61 m below soffit	Velocity
	BDP_A6_4	0.88 m below soffit	Velocity
	BDP_A6_5	1.15 m below soffit	Velocity
	BDP_A6_6	1.42 m below soffit	Velocity
	BDP_A6_7	1.68 m below soffit	Velocity
	BDP_A6_8	1.95 m below soffit	Velocity

Table A.2: West Structure Channel List (continued)

Device Location	Channel Name	Channel Location	Measurement Type
A7	TC_A7_1	0.03 m below ceiling	Temperature
	TC_A7_2	0.30 m below ceiling	Temperature
	TC_A7_3	0.61 m below ceiling	Temperature
	TC_A7_4	0.91 m below ceiling	Temperature
	TC_A7_5	1.22 m below ceiling	Temperature
	TC_A7_6	1.52 m below ceiling	Temperature
	TC_A7_7	1.83 m below ceiling	Temperature
	TC_A7_8	2.13 m below ceiling	Temperature
A8	TC_A8_1	0.03 m below ceiling	Temperature
	TC_A8_2	0.30 m below ceiling	Temperature
	TC_A8_3	0.61 m below ceiling	Temperature
	TC_A8_4	0.91 m below ceiling	Temperature
	TC_A8_5	1.22 m below ceiling	Temperature
	TC_A8_6	1.52 m below ceiling	Temperature
	TC_A8_7	1.83 m below ceiling	Temperature
	TC_A8_8	2.13 m below ceiling	Temperature
A9	TC_A9_1	0.03 m below ceiling	Temperature
	TC_A9_2	0.30 m below ceiling	Temperature
	TC_A9_3	0.61 m below ceiling	Temperature
	TC_A9_4	0.91 m below ceiling	Temperature
	TC_A9_5	1.22 m below ceiling	Temperature
	TC_A9_6	1.52 m below ceiling	Temperature
	TC_A9_7	1.83 m below ceiling	Temperature
	TC_A9_8	2.13 m below ceiling	Temperature

Table A.2: West Structure Channel List (continued)

Device Location	Channel Name	Channel Location	Measurement Type
A10	TC_A10_1	0.08 m below soffit	Temperature
	TC_A10_2	0.34 m below soffit	Temperature
	TC_A10_3	0.61 m below soffit	Temperature
	TC_A10_4	0.88 m below soffit	Temperature
	TC_A10_5	1.15 m below soffit	Temperature
	TC_A10_6	1.42 m below soffit	Temperature
	TC_A10_7	1.68 m below soffit	Temperature
	TC_A10_8	1.95 m below soffit	Temperature
	BDP_A10_1	0.08 m below soffit	Velocity
	BDP_A10_2	0.34 m below soffit	Velocity
	BDP_A10_3	0.61 m below soffit	Velocity
	BDP_A10_4	0.88 m below soffit	Velocity
	BDP_A10_5	1.15 m below soffit	Velocity
	BDP_A10_6	1.42 m below soffit	Velocity
	BDP_A10_7	1.68 m below soffit	Velocity
	BDP_A10_8	1.95 m below soffit	Velocity
A11	CO_B	1.22 m above floor	CO concentration
	CO2_B	1.22 m above floor	CO <sub>2</sub> concentration
	O2_B	1.22 m above floor	O <sub>2</sub> concentration
A11	TC_A11_1	0.08 m below soffit	Temperature
	TC_A11_2	0.34 m below soffit	Temperature
	TC_A11_3	0.61 m below soffit	Temperature
	TC_A11_4	0.88 m below soffit	Temperature
	TC_A11_5	1.15 m below soffit	Temperature
	TC_A11_6	1.42 m below soffit	Temperature
	TC_A11_7	1.68 m below soffit	Temperature
	TC_A11_8	1.95 m below soffit	Temperature
	BDP_A11_1	0.08 m below soffit	Velocity
	BDP_A11_2	0.34 m below soffit	Velocity
	BDP_A11_3	0.61 m below soffit	Velocity
	BDP_A11_4	0.88 m below soffit	Velocity
	BDP_A11_5	1.15 m below soffit	Velocity
	BDP_A11_6	1.42 m below soffit	Velocity
	BDP_A11_7	1.68 m below soffit	Velocity
	BDP_A11_8	1.95 m below soffit	Velocity

Table A.2: West Structure Channel List (continued)

Device Location	Channel Name	Channel Location	Measurement Type
A13	TC_A13_1	0.08 m below soffit	Temperature
	TC_A13_2	0.34 m below soffit	Temperature
	TC_A13_3	0.61 m below soffit	Temperature
	TC_A13_4	0.88 m below soffit	Temperature
	TC_A13_5	1.15 m below soffit	Temperature
	TC_A13_6	1.42 m below soffit	Temperature
	TC_A13_7	1.68 m below soffit	Temperature
	TC_A13_8	1.95 m below soffit	Temperature
	BDP_A13_1	0.08 m below soffit	Velocity
	BDP_A13_2	0.34 m below soffit	Velocity
	BDP_A13_3	0.61 m below soffit	Velocity
	BDP_A13_4	0.88 m below soffit	Velocity
	BDP_A13_5	1.15 m below soffit	Velocity
	BDP_A13_6	1.42 m below soffit	Velocity
	BDP_A13_7	1.68 m below soffit	Velocity
	BDP_A13_8	1.95 m below soffit	Velocity
A14	TC_A14_1	0.08 m below soffit	Temperature
	TC_A14_2	0.34 m below soffit	Temperature
	TC_A14_3	0.61 m below soffit	Temperature
	TC_A14_4	0.88 m below soffit	Temperature
	TC_A14_5	1.15 m below soffit	Temperature
	TC_A14_6	1.42 m below soffit	Temperature
	TC_A14_7	1.68 m below soffit	Temperature
	TC_A14_8	1.95 m below soffit	Temperature
	BDP_A14_1	0.08 m below soffit	Velocity
	BDP_A14_2	0.34 m below soffit	Velocity
	BDP_A14_3	0.61 m below soffit	Velocity
	BDP_A14_4	0.88 m below soffit	Velocity
	BDP_A14_5	1.15 m below soffit	Velocity
	BDP_A14_6	1.42 m below soffit	Velocity
	BDP_A14_7	1.68 m below soffit	Velocity
	BDP_A14_8	1.95 m below soffit	Velocity

Table A.2: West Structure Channel List (continued)

Device Location	Channel Name	Channel Location	Measurement Type
<b>A16</b>	HF_2_H	1 m above floor, facing N wall (horizontal)	Total heat flux
	HF_2_V	1 m above floor, facing ceiling (vertical)	Total heat flux
<b>A17</b>	HF_1_H	1 m above floor, facing doorway (horizontal)	Total heat flux
	HF_1_V	1 m above floor, facing ceiling (vertical)	Total heat flux

## Appendix B: Experimental and FDS Data Plots

### B.1 Temperature

#### *Hot Gas Layer Temperatures*

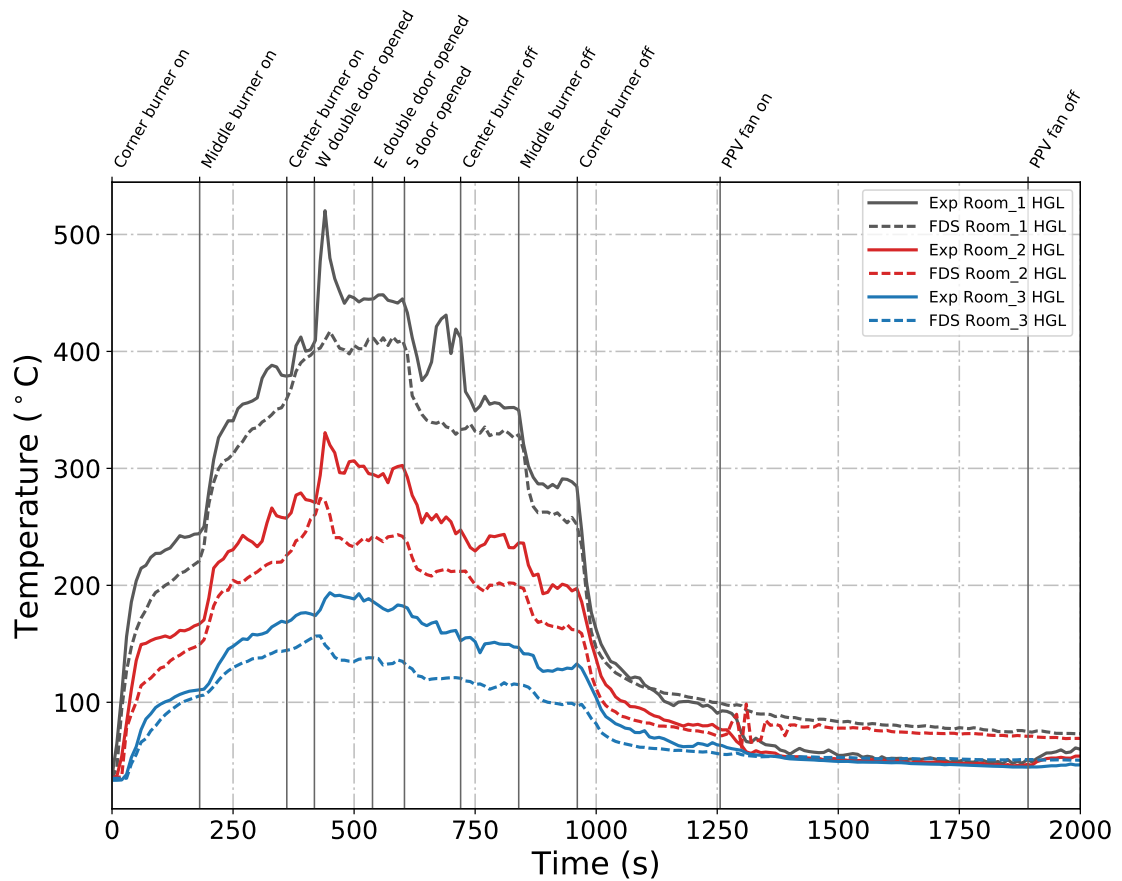


Figure B.1: Plots of measured and predicted hot gas layer temperatures in the three rooms of the East Structure during Test 2.

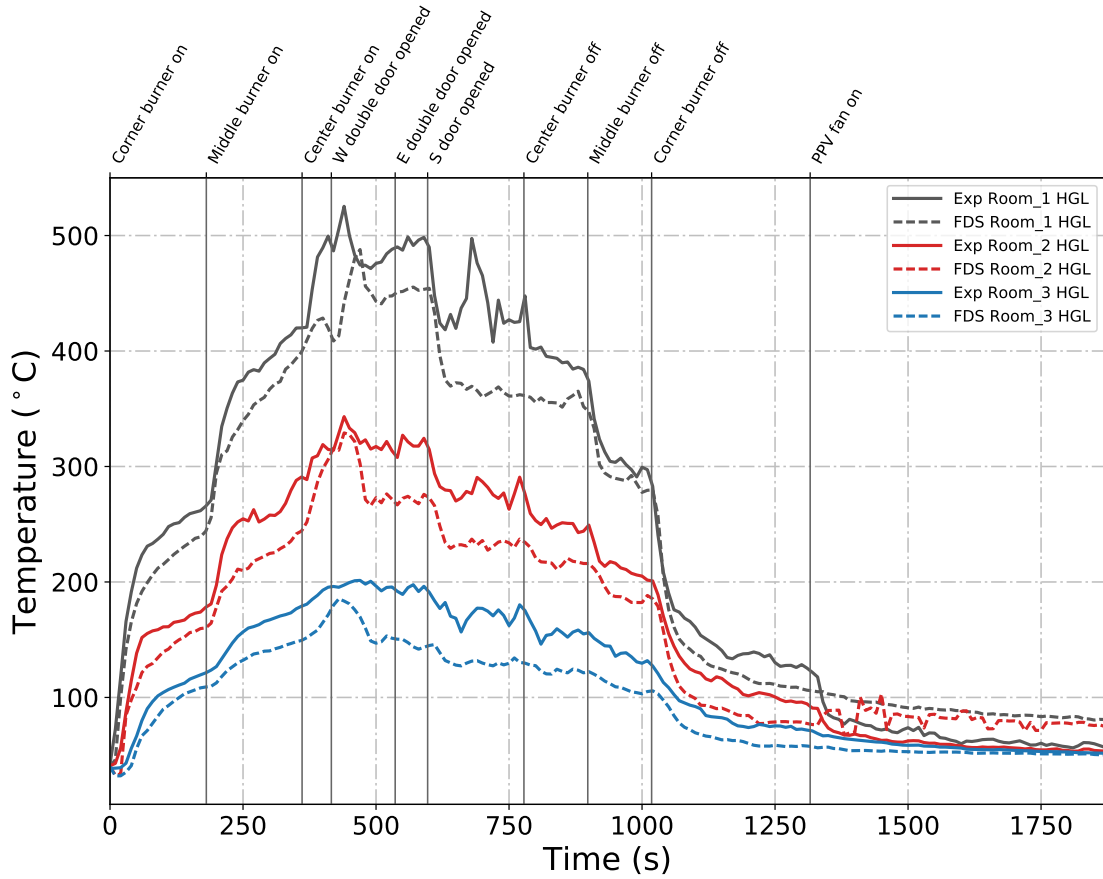


Figure B.2: Plots of measured and predicted hot gas layer temperatures in the three rooms of the East Structure during Test 3.

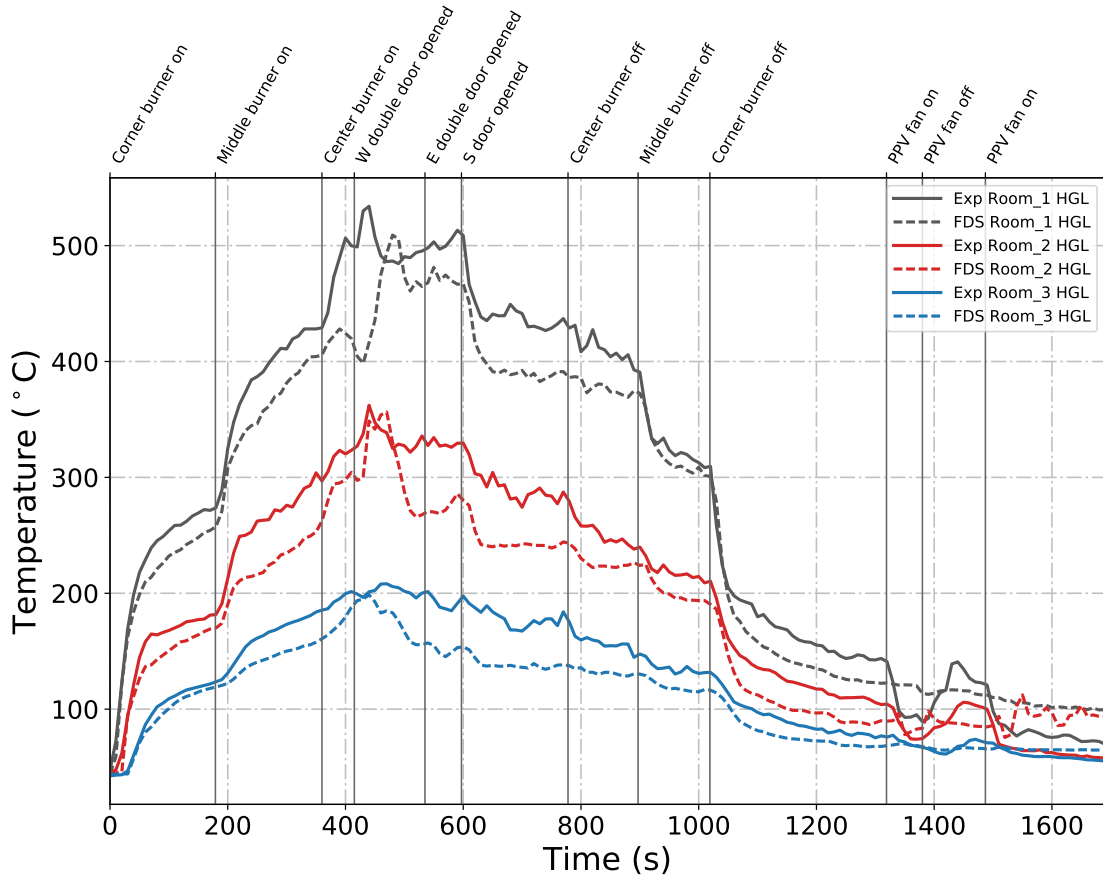


Figure B.3: Plots of measured and predicted hot gas layer temperatures in the three rooms of the East Structure during Test 4.

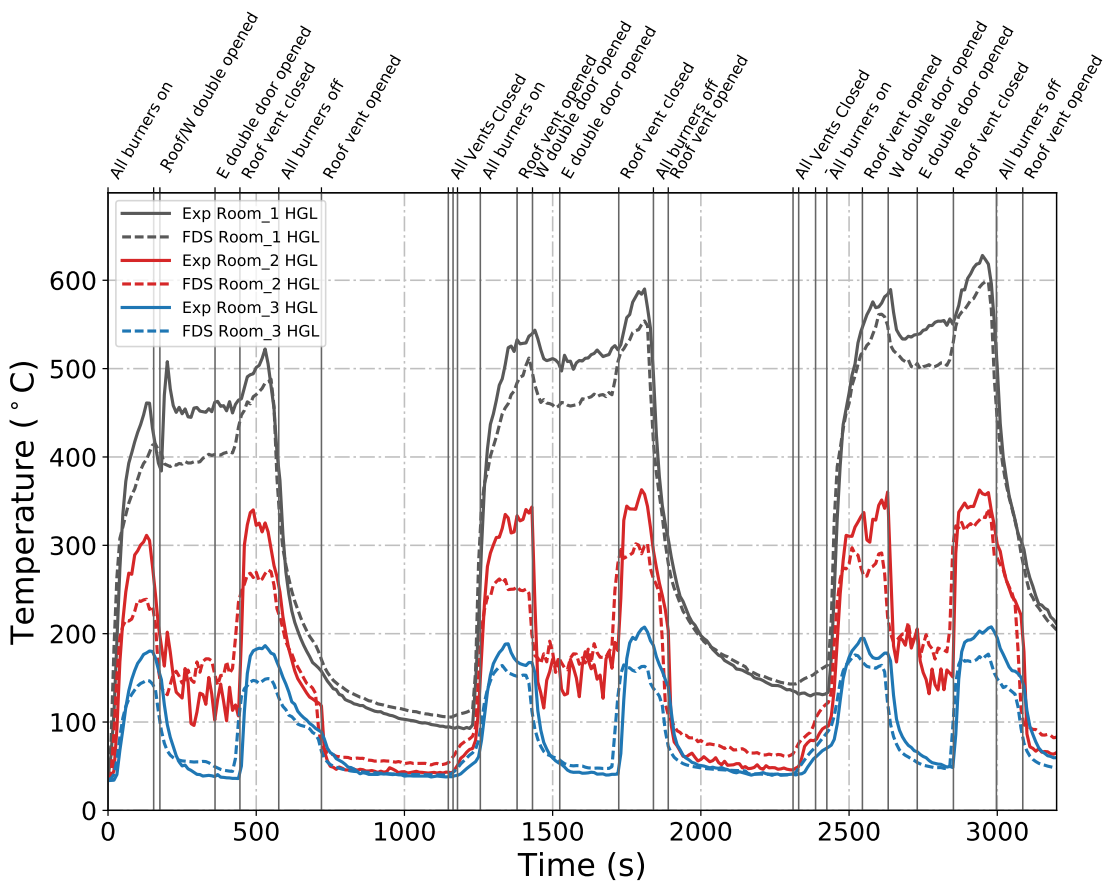


Figure B.4: Plots of measured and predicted hot gas layer temperatures in the three rooms of the East Structure during Test 5.

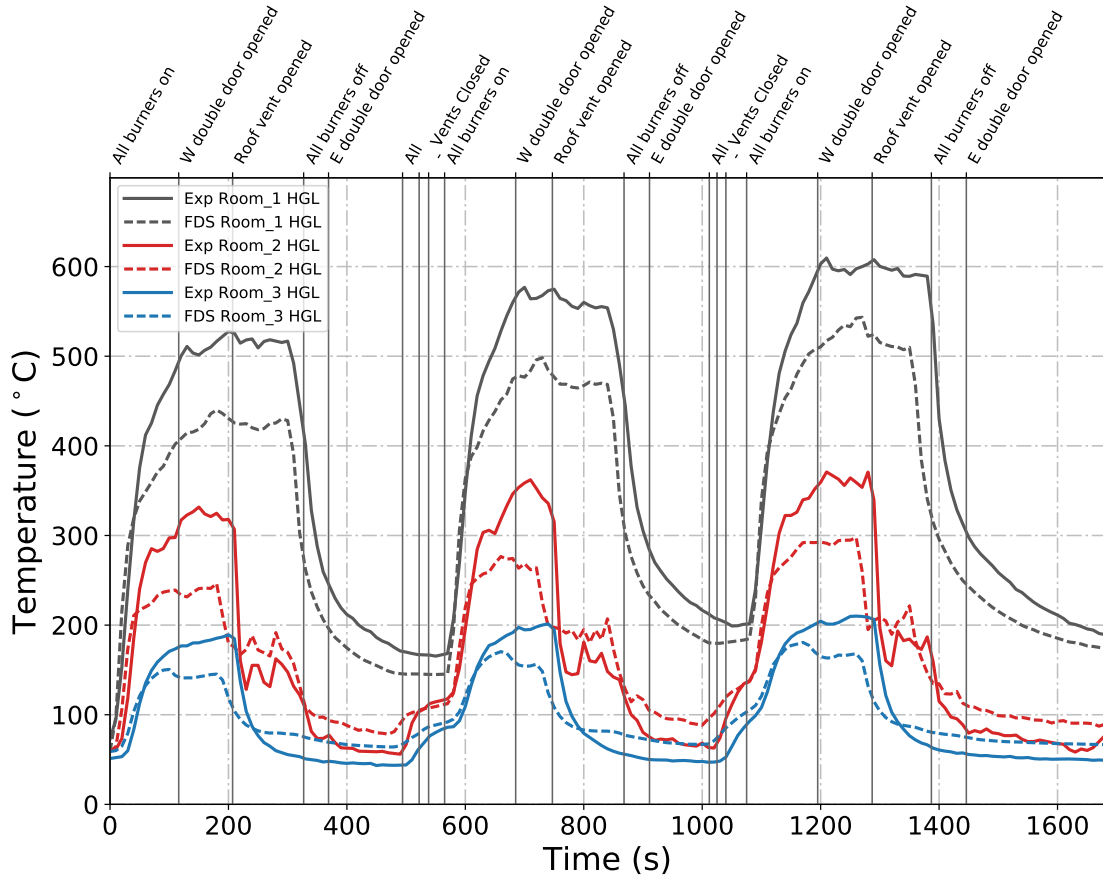


Figure B.5: Plots of measured and predicted hot gas layer temperatures in the three rooms of the East Structure during Test 6.

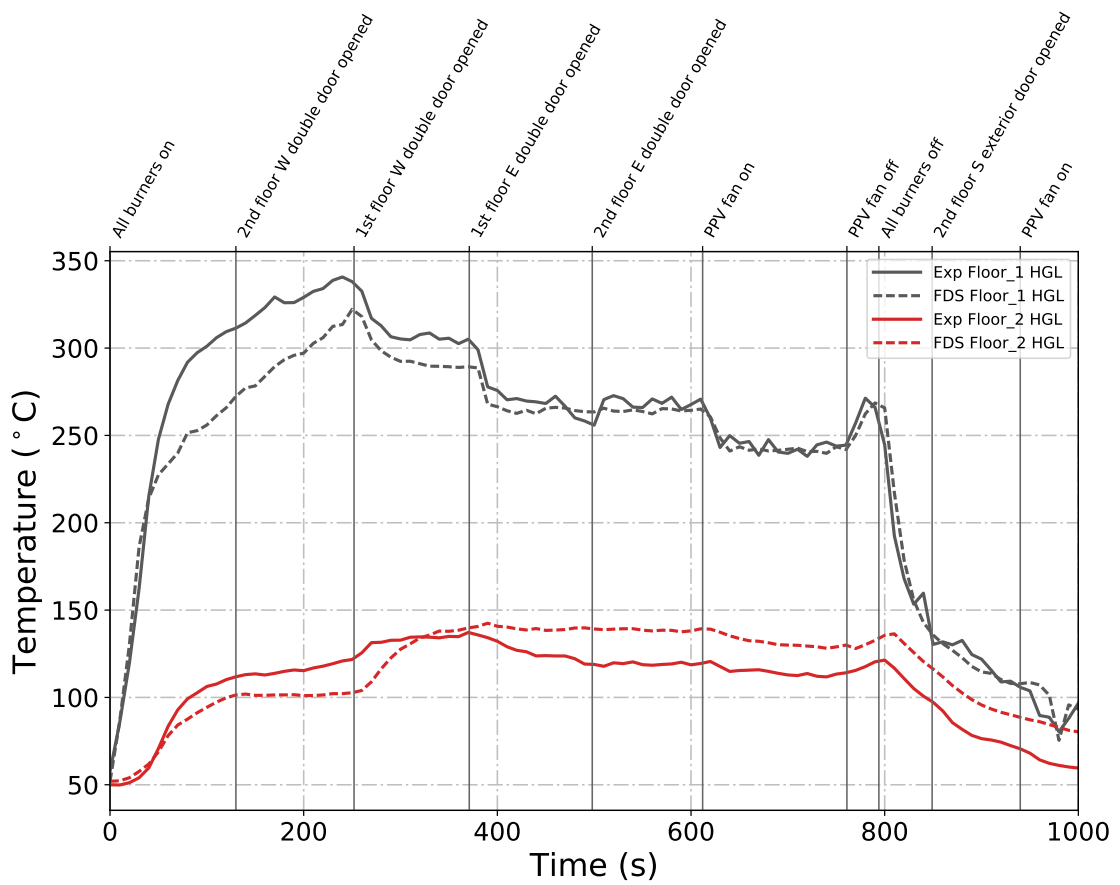


Figure B.6: Plots of measured and predicted hot gas layer temperatures on the first and second floors of the West Structure during Test 23.

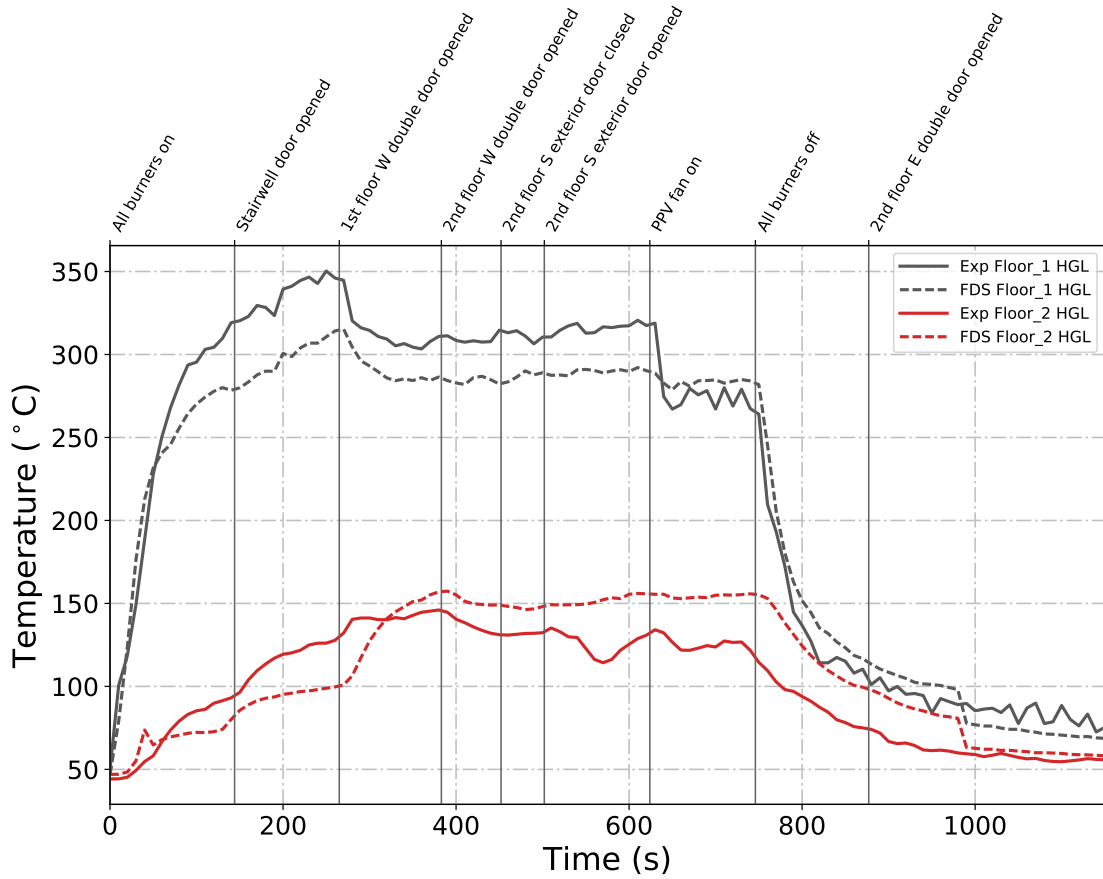


Figure B.7: Plots of measured and predicted hot gas layer temperatures on the first and second floors of the West Structure during Test 24.

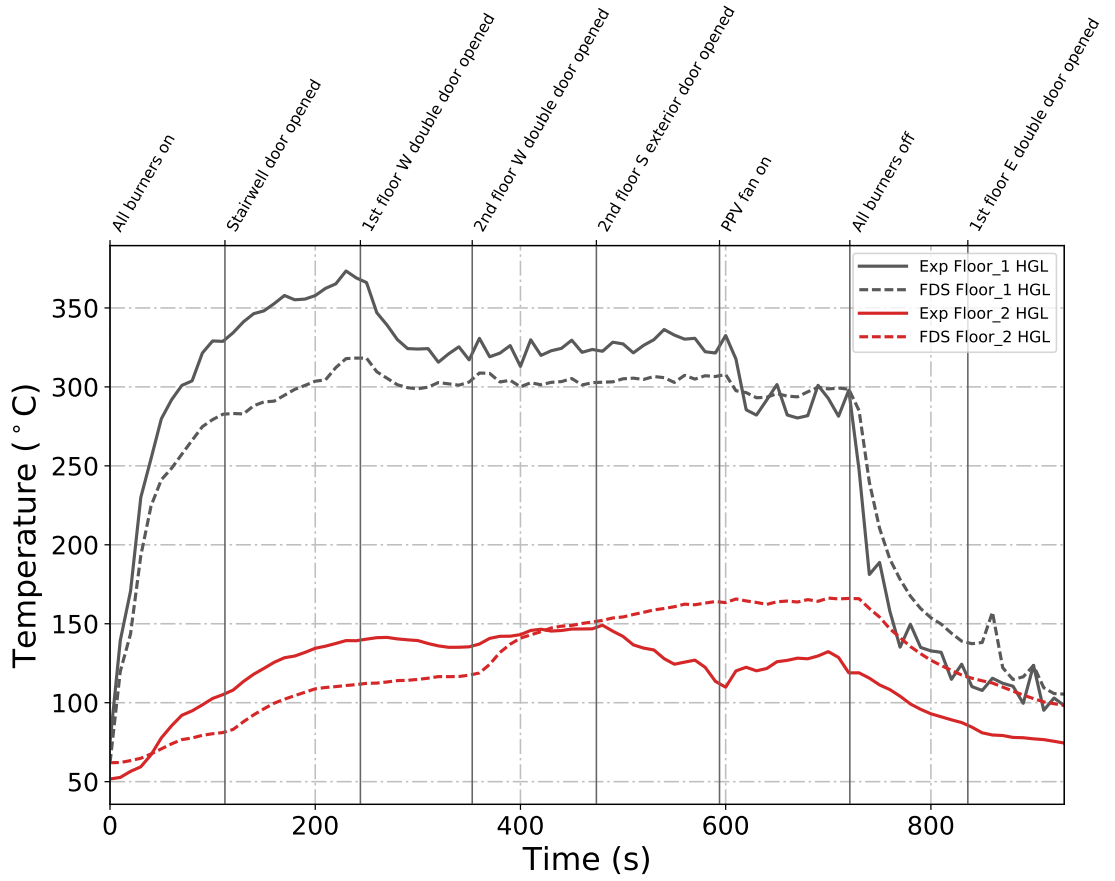


Figure B.8: Plots of measured and predicted hot gas layer temperatures on the first and second floors of the West Structure during Test 25.

## Ceiling Jet Temperatures

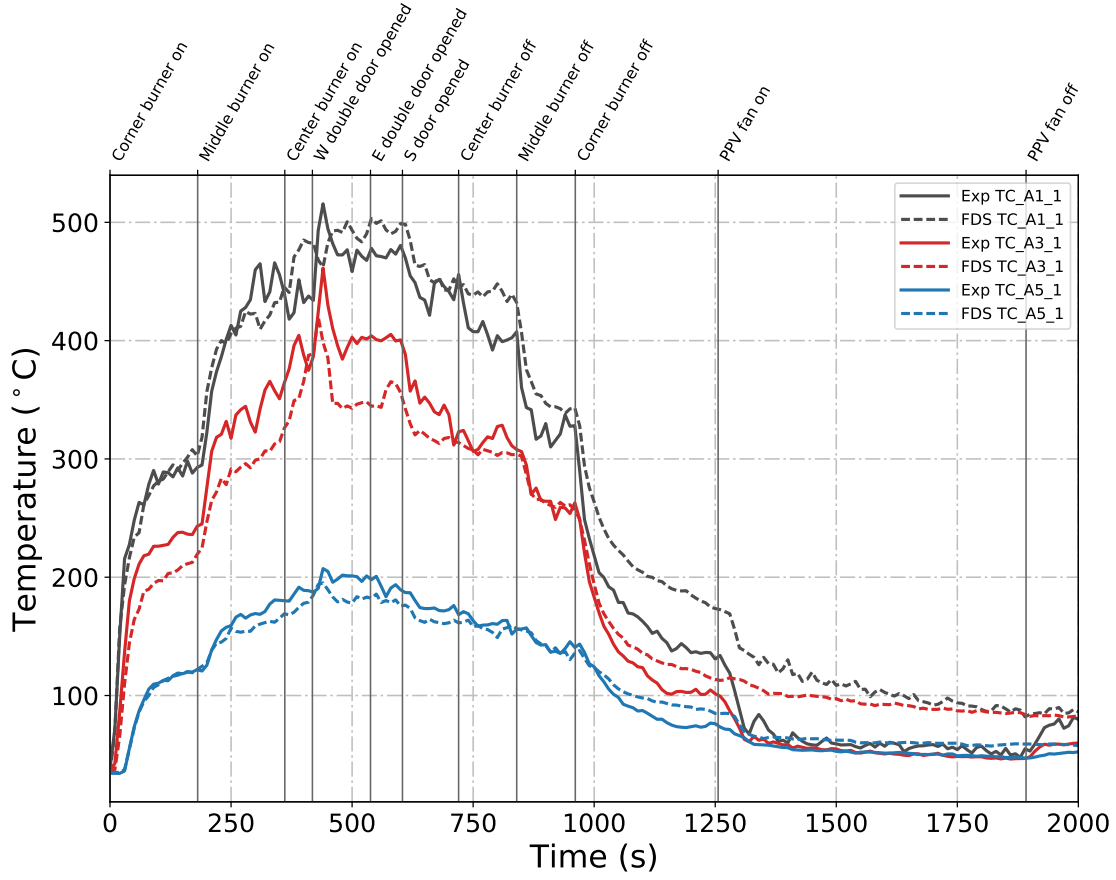


Figure B.9: Plots of measured and predicted ceiling jet temperatures during Test 2 obtained from thermocouple arrays A1, A3, and A5 located in the fire room, middle room, and north room of the East Structure, respectively.

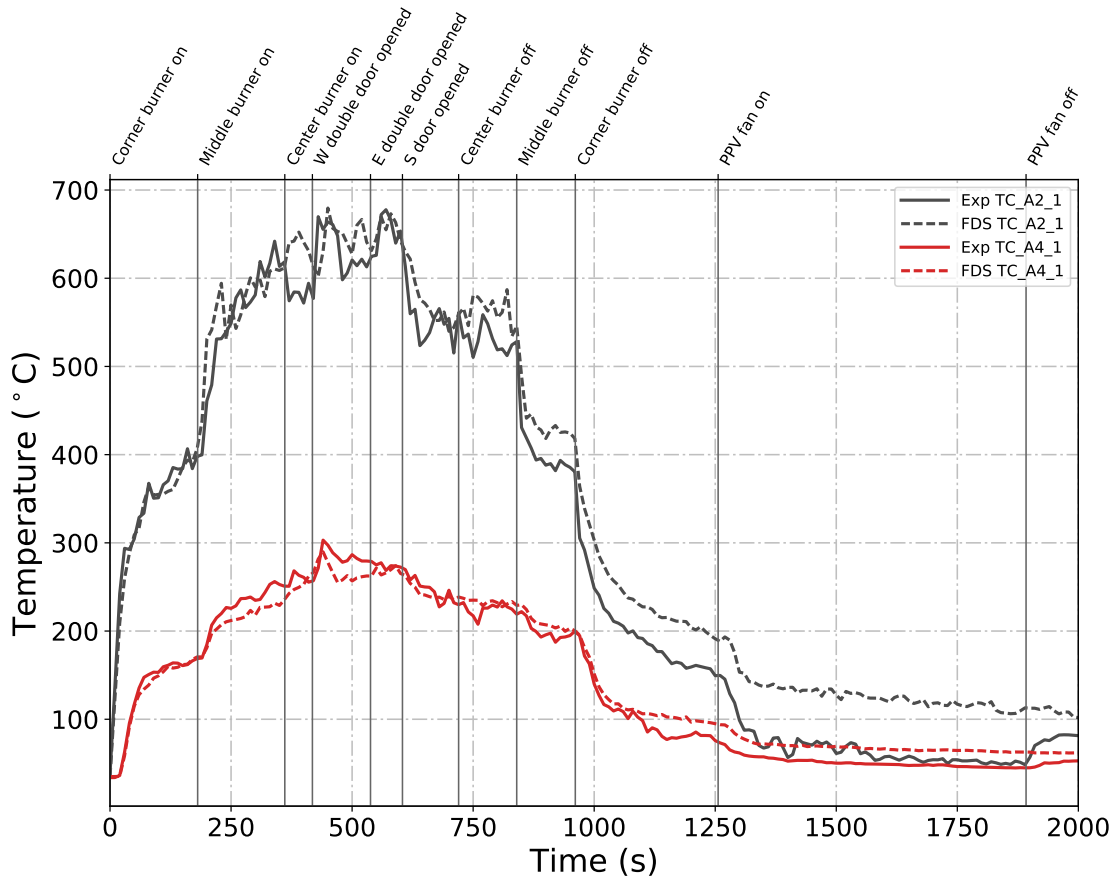


Figure B.10: Plots of measured and predicted ceiling jet temperatures during Test 2 obtained from thermocouple arrays A2 and A4 located in the fire room and north room of the East Structure, respectively.

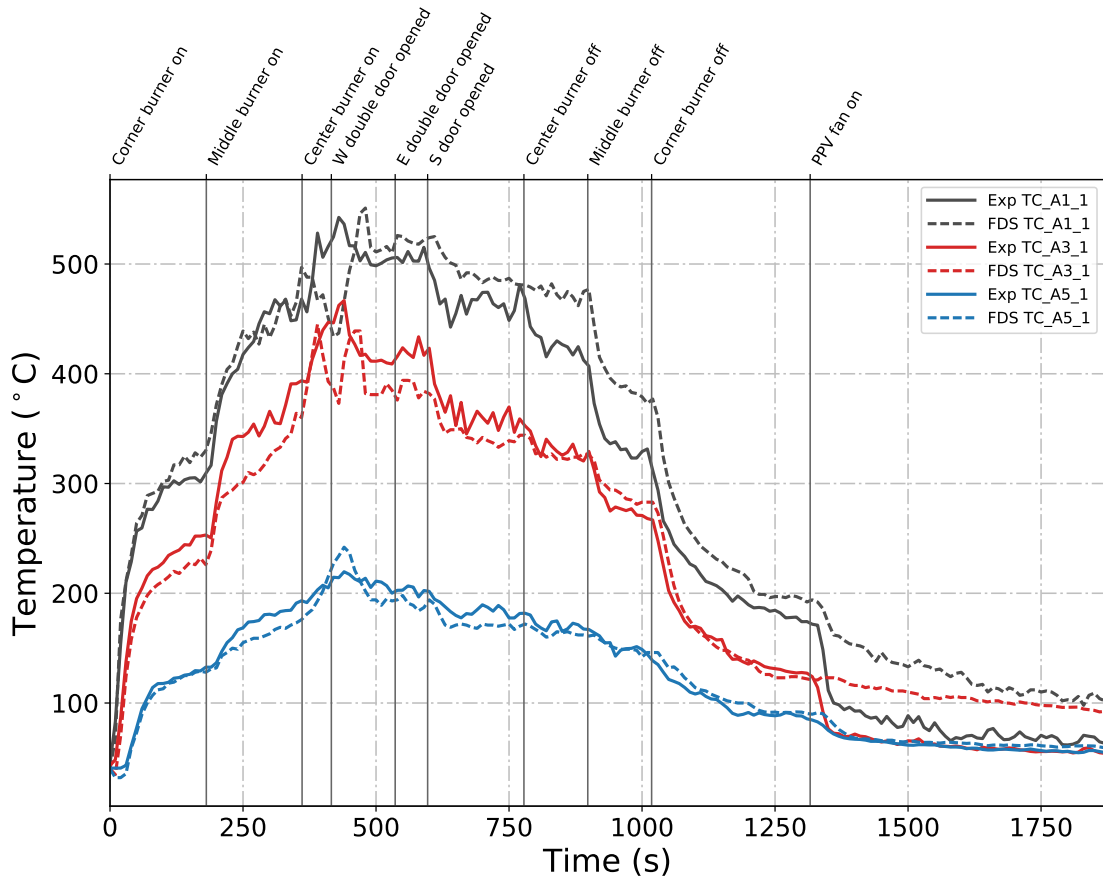


Figure B.11: Plots of measured and predicted ceiling jet temperatures during Test 3 obtained from thermocouple arrays A1, A3, and A5 located in the fire room, middle room, and north room of the East Structure, respectively.

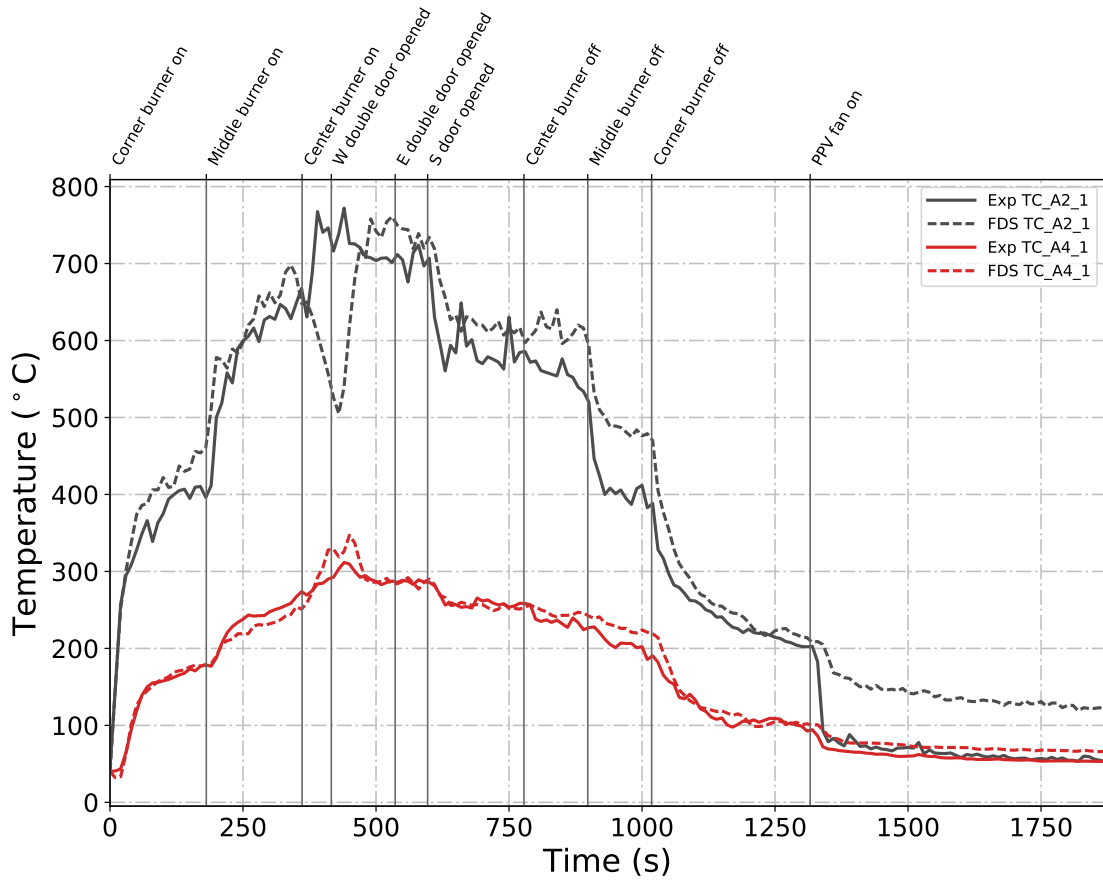


Figure B.12: Plots of measured and predicted ceiling jet temperatures during Test 3 obtained from thermocouple arrays A2 and A4 located in the fire room and north room of the East Structure, respectively.

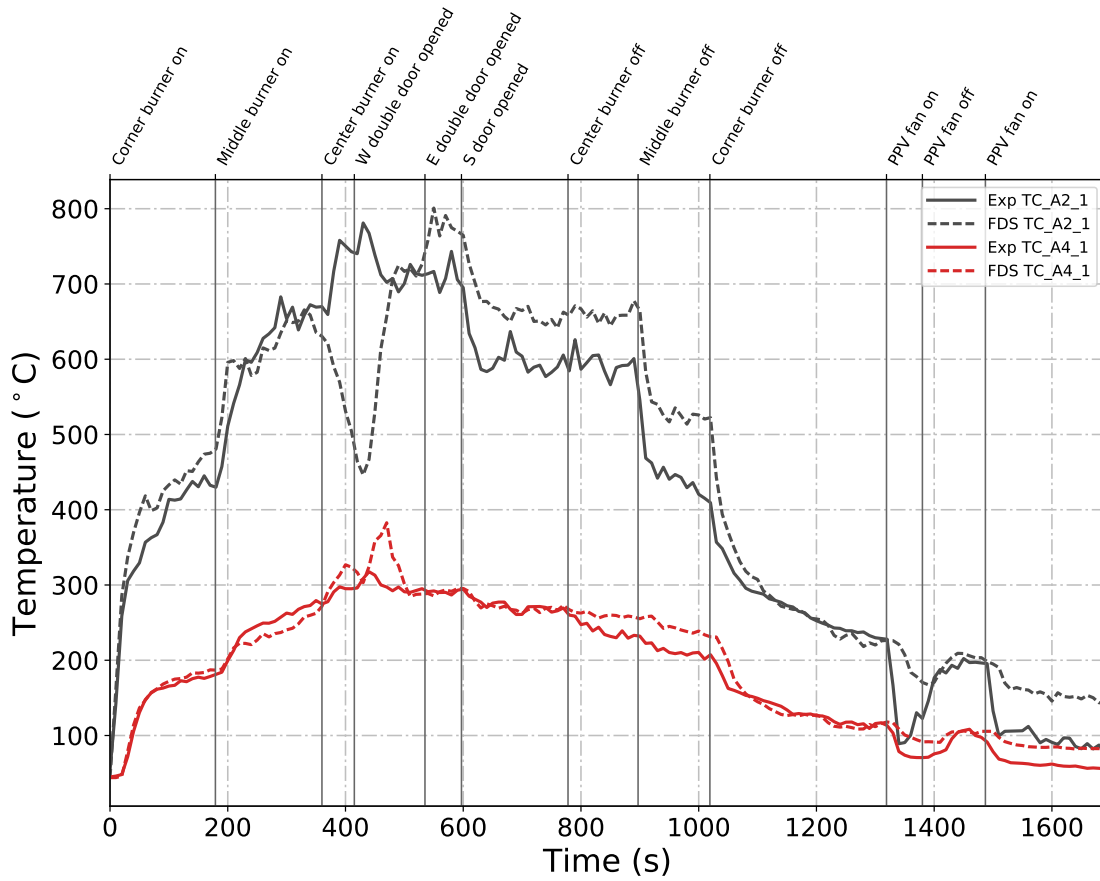


Figure B.13: Plots of measured and predicted ceiling jet temperatures during Test 4 obtained from thermocouple arrays A2 and A4 located in the fire room and north room of the East Structure, respectively.

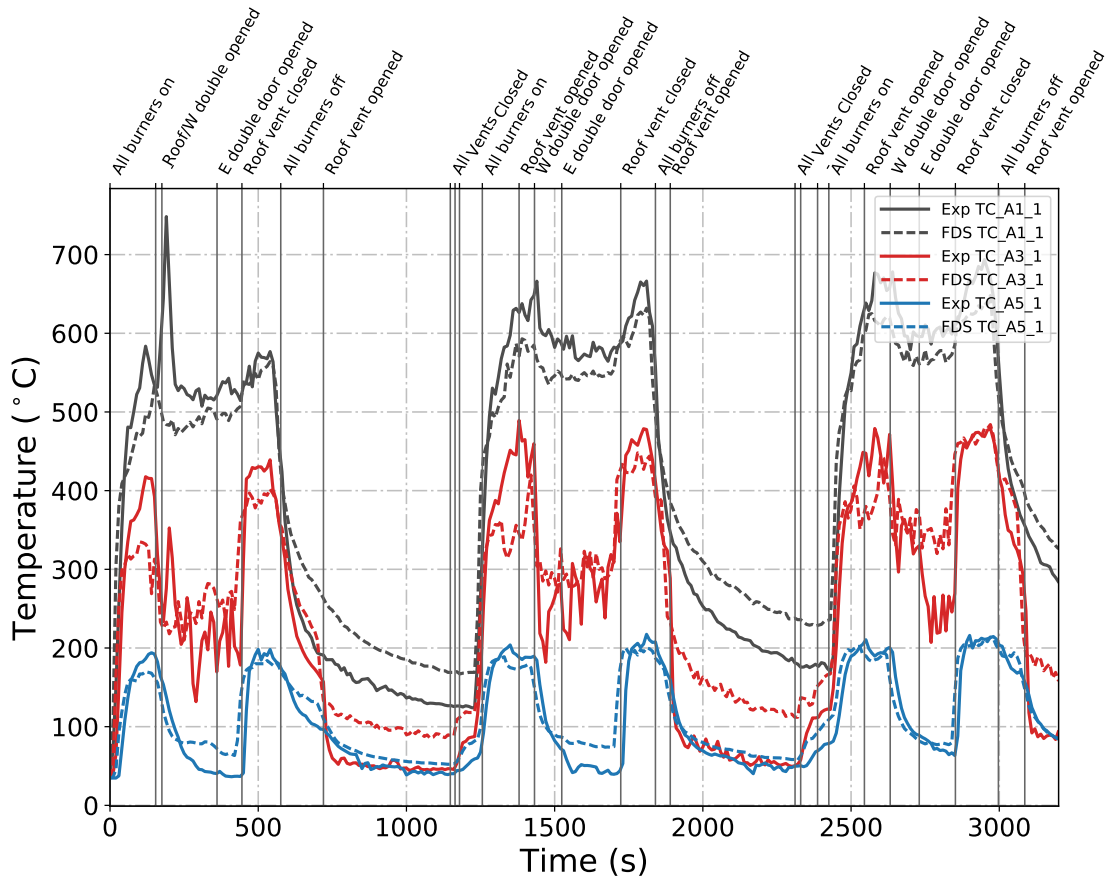


Figure B.14: Plots of measured and predicted ceiling jet temperatures during Test 5 obtained from thermocouple arrays A1, A3, and A5 located in the fire room, middle room, and north room of the East Structure, respectively.

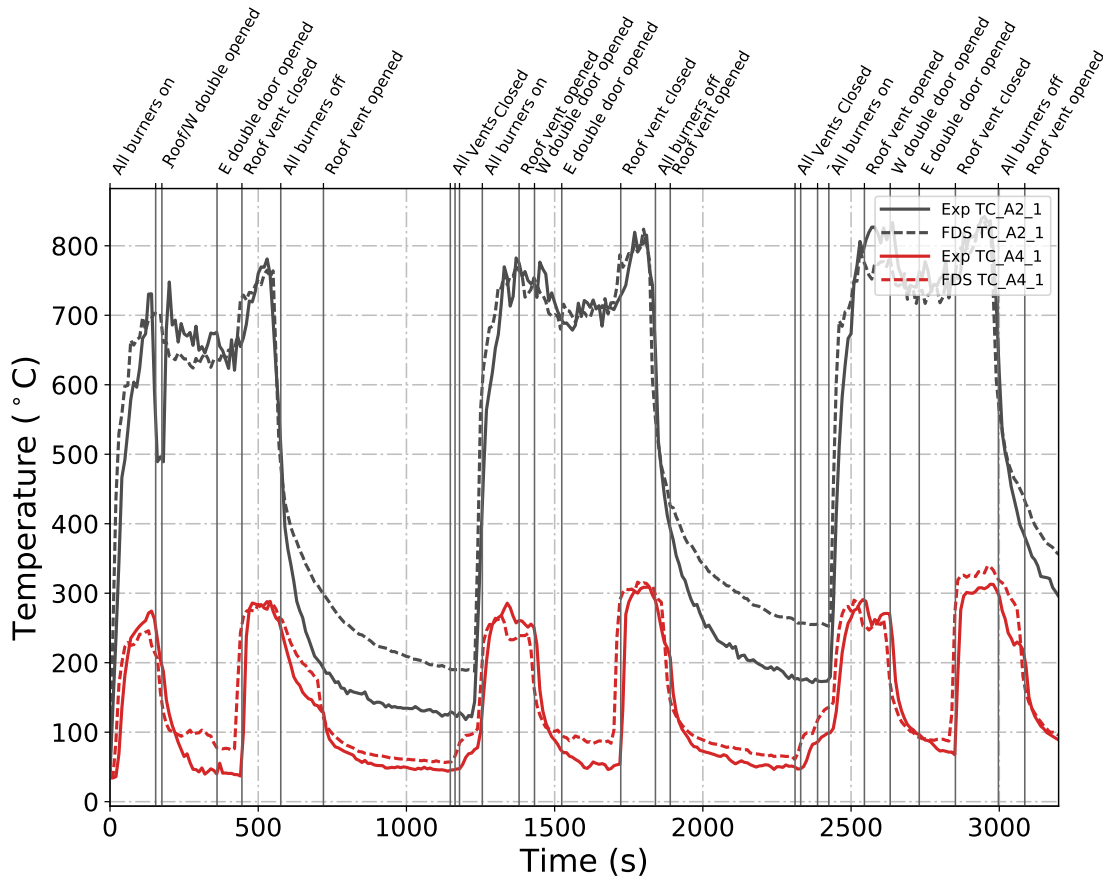


Figure B.15: Plots of measured and predicted ceiling jet temperatures during Test 5 obtained from thermocouple arrays A2 and A4 located in the fire room and north room of the East Structure, respectively.

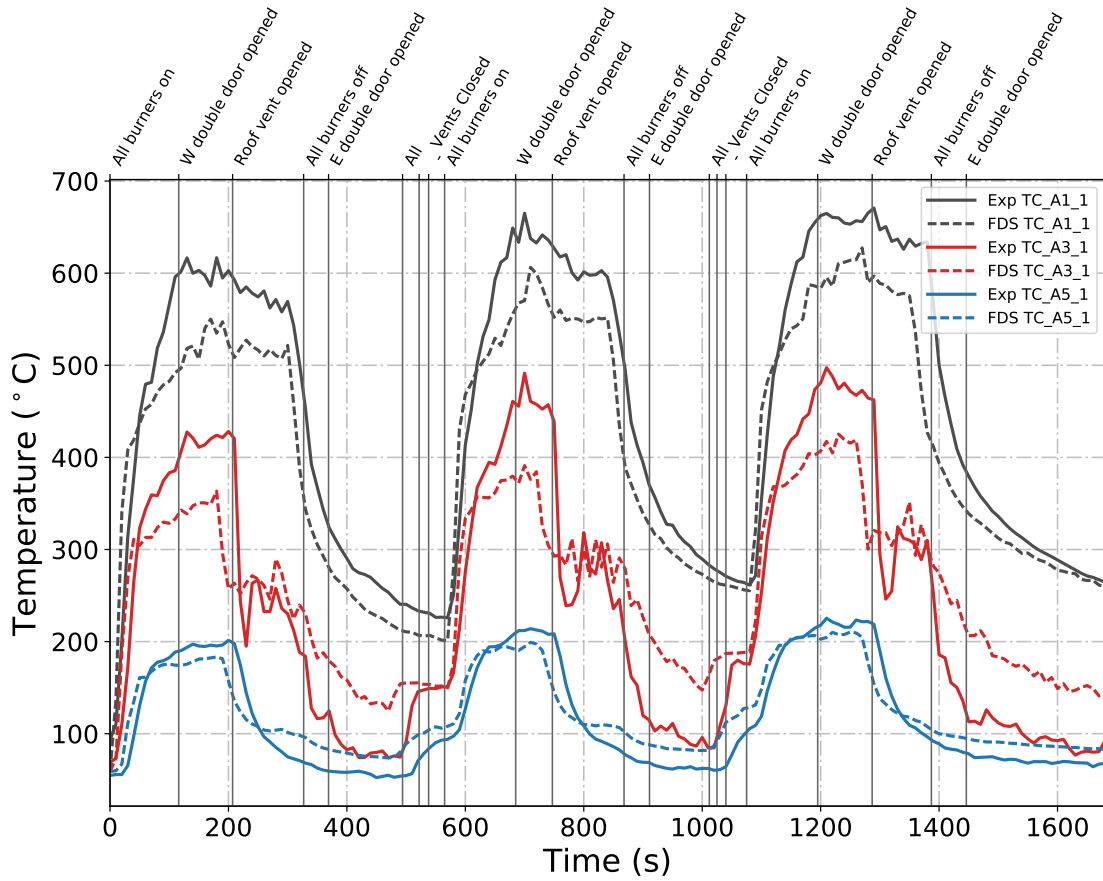


Figure B.16: Plots of measured and predicted ceiling jet temperatures during Test 6 obtained from thermocouple arrays A1, A3, and A5 located in the fire room, middle room, and north room of the East Structure, respectively.

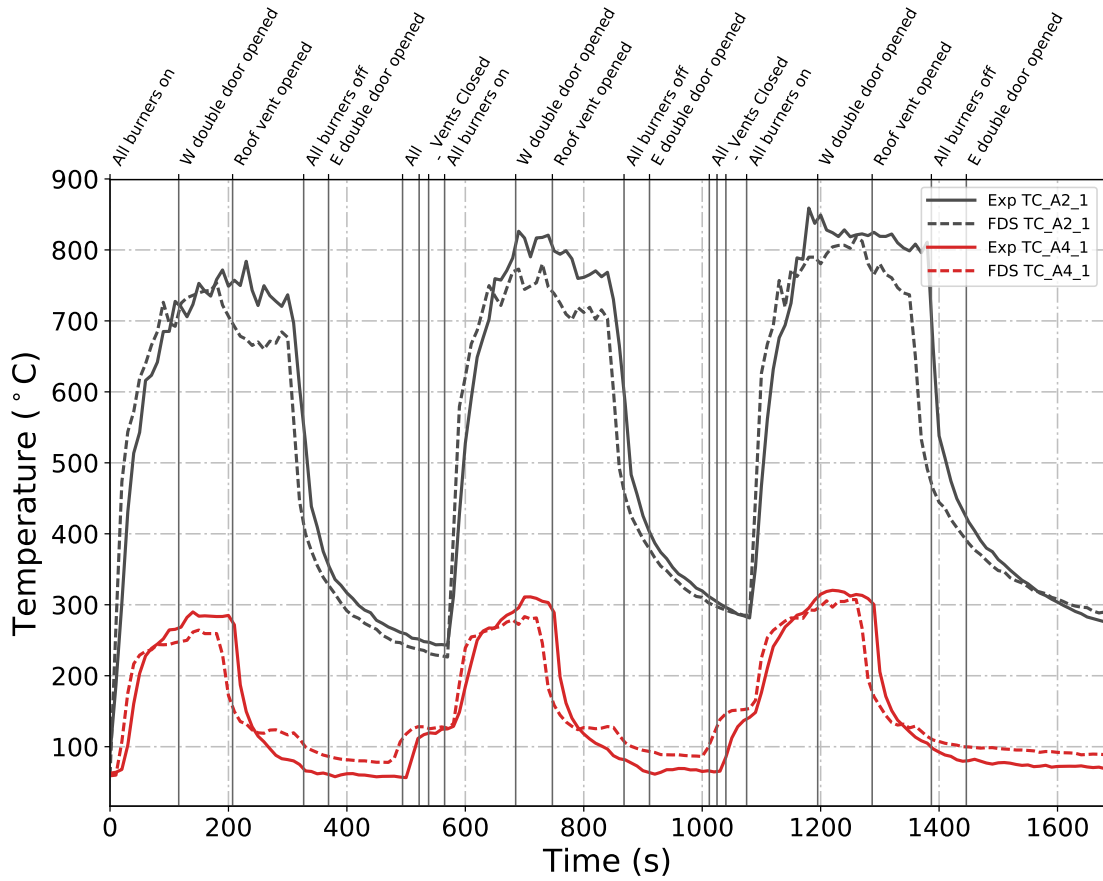


Figure B.17: Plots of measured and predicted ceiling jet temperatures during Test 6 obtained from thermocouple arrays A2 and A4 located in the fire room and north room of the East Structure, respectively.

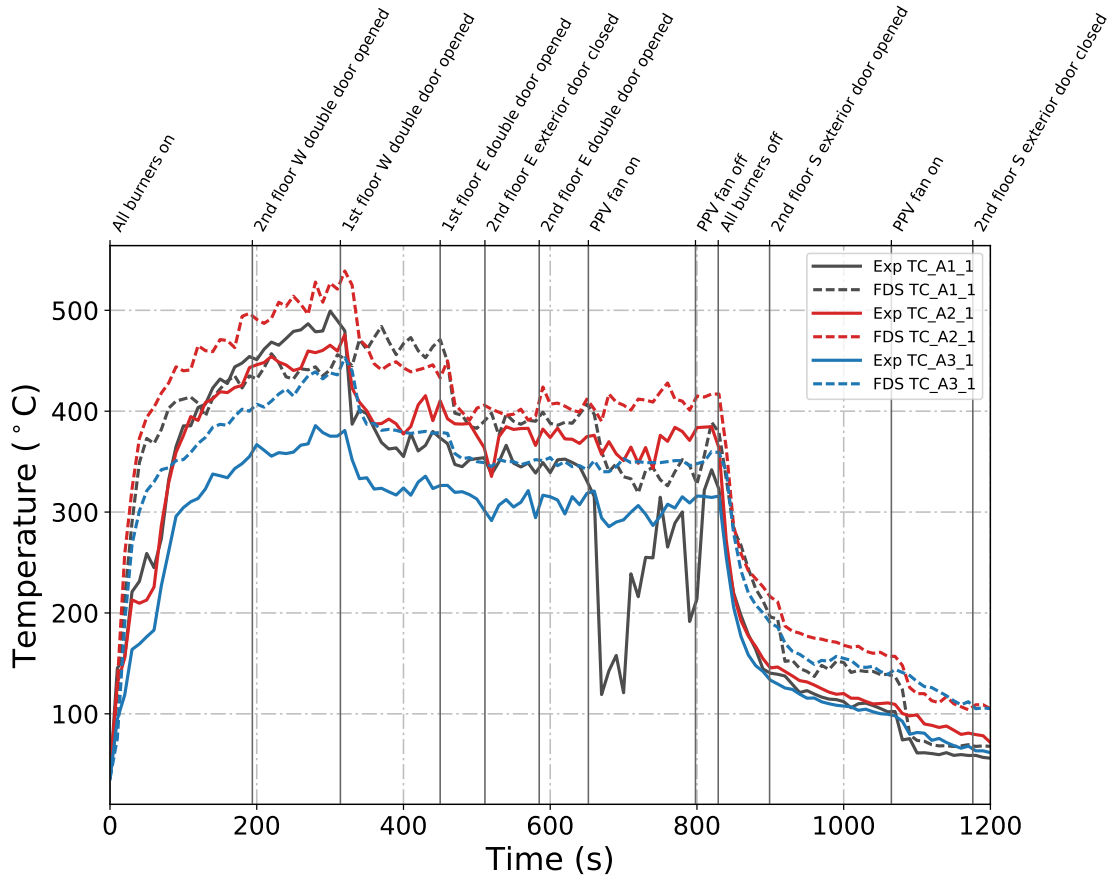


Figure B.18: Plots of measured and predicted ceiling jet temperatures on the first floor of the West Structure during Test 22.

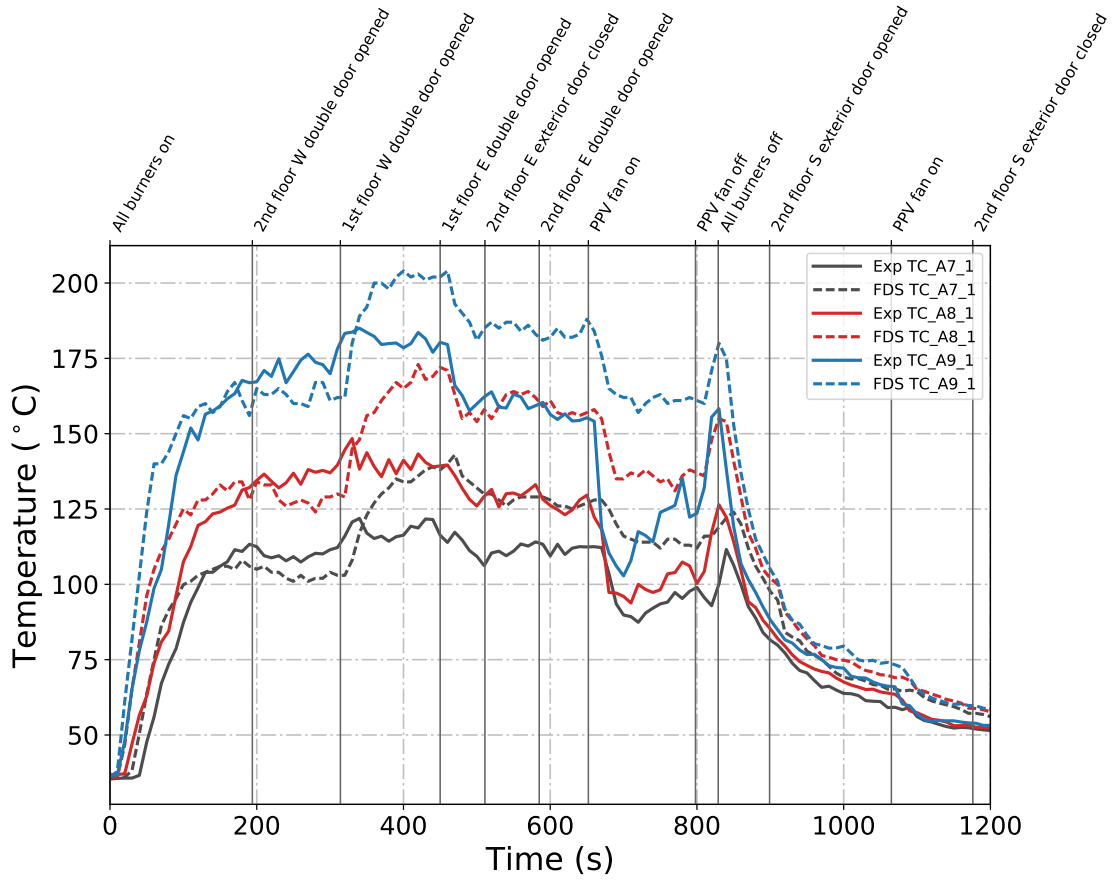


Figure B.19: Plots of measured and predicted ceiling jet temperatures on the second floor of the West Structure during Test 22.

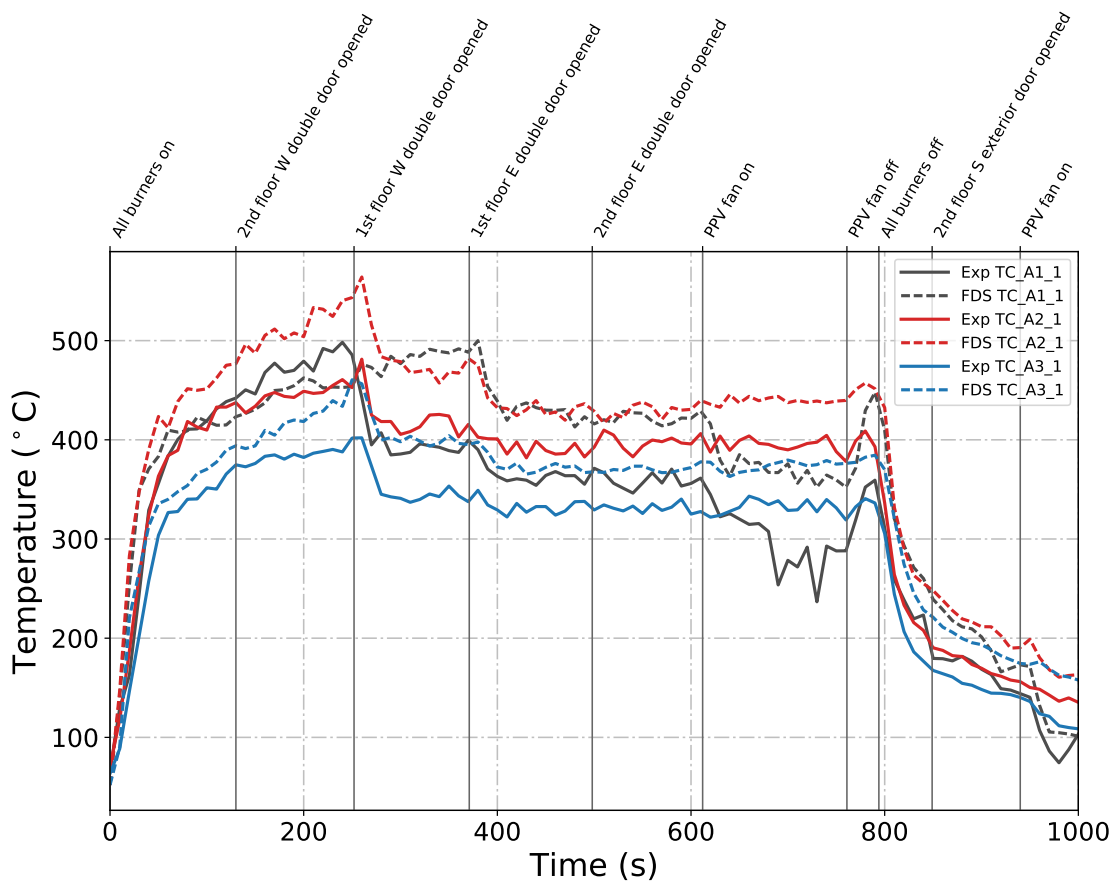


Figure B.20: Plots of measured and predicted ceiling jet temperatures on the first floor of the West Structure during Test 23.

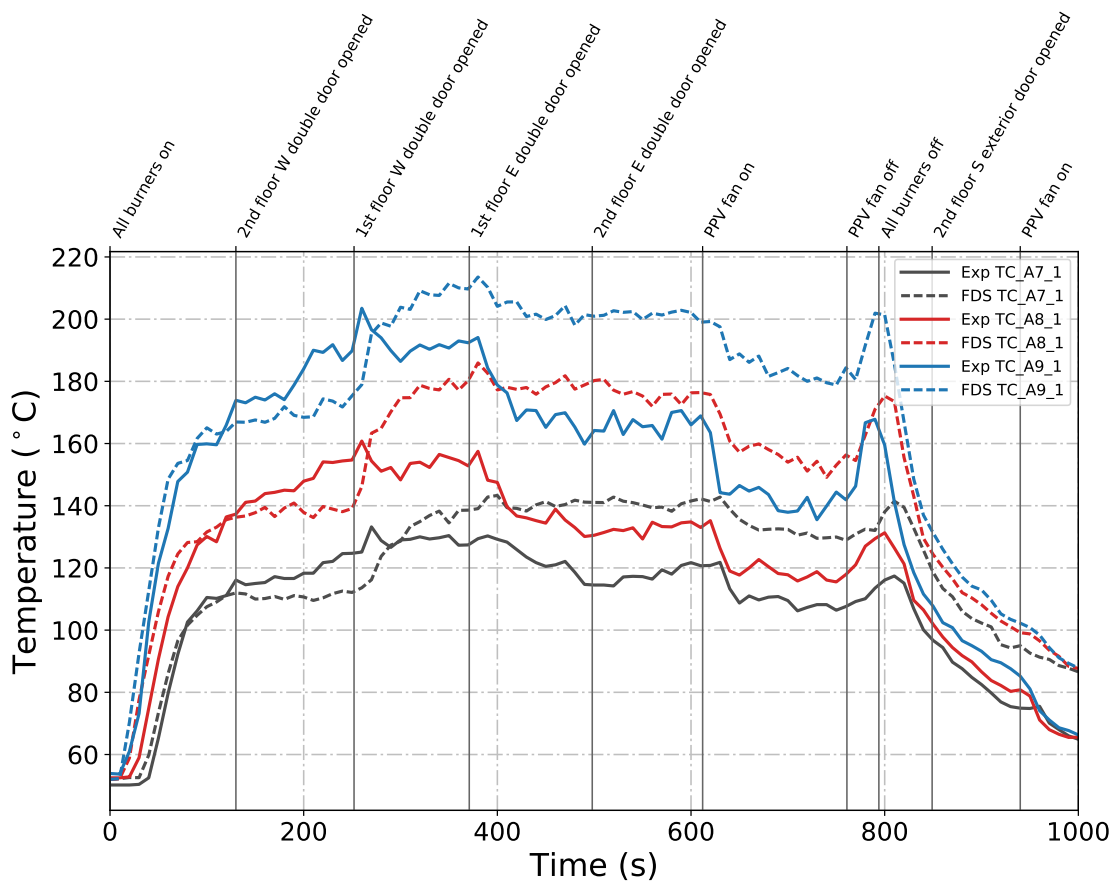


Figure B.21: Plots of measured and predicted ceiling jet temperatures on the second floor of the West Structure during Test 23.

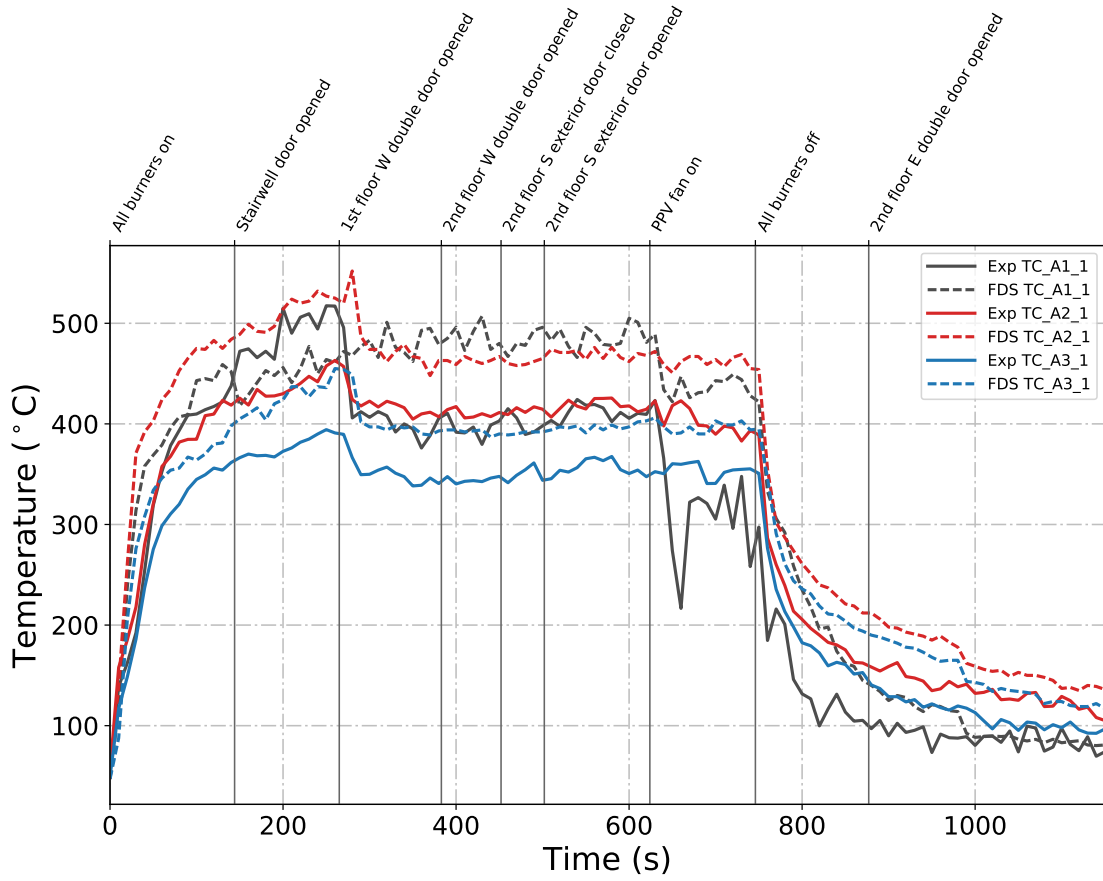


Figure B.22: Plots of measured and predicted ceiling jet temperatures on the first floor of the West Structure during Test 24.

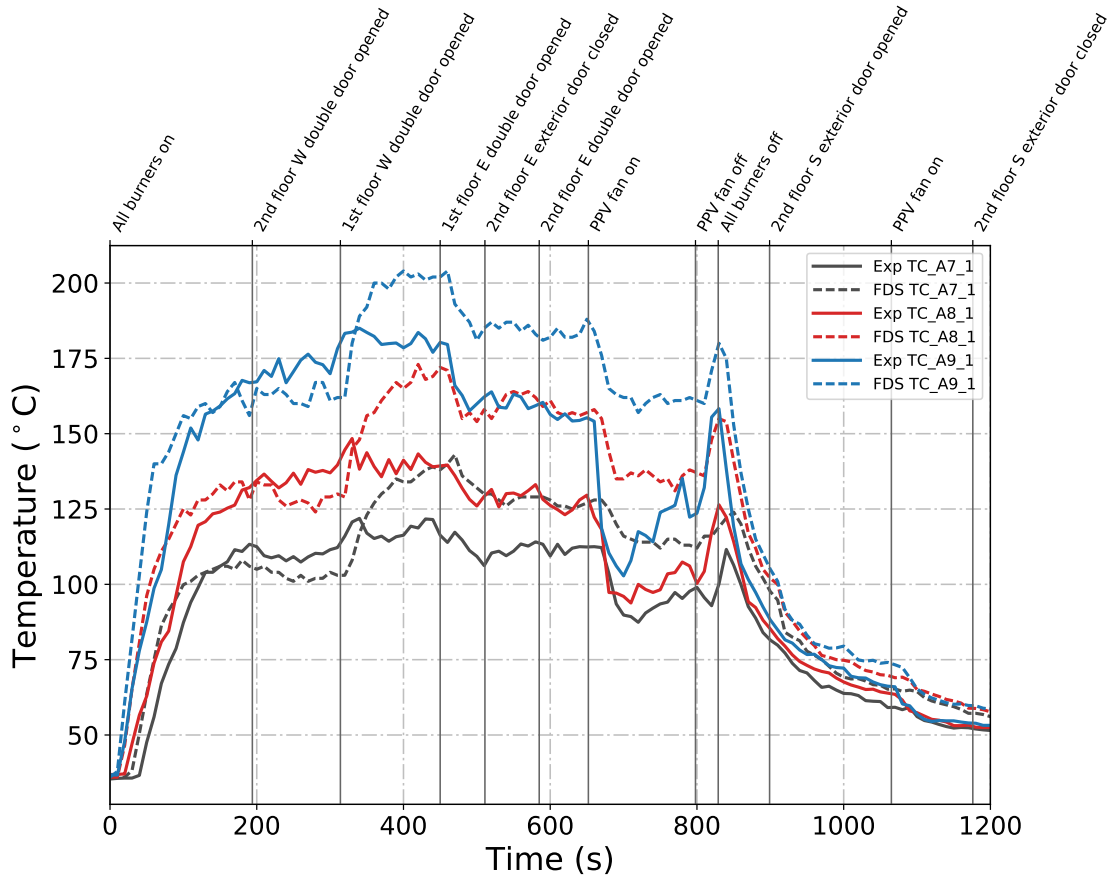


Figure B.23: Plots of measured and predicted ceiling jet temperatures on the second floor of the West Structure during Test 24.

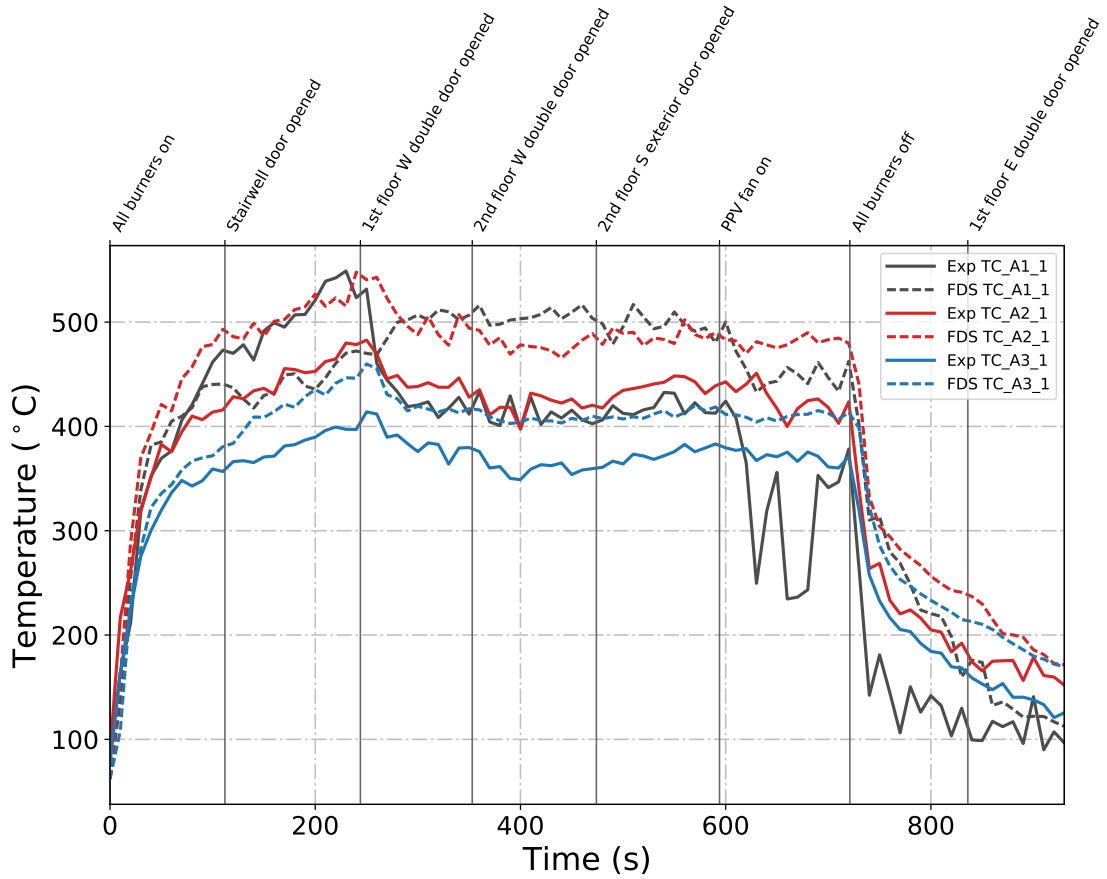


Figure B.24: Plots of measured and predicted ceiling jet temperatures on the first floor of the West Structure during Test 25.

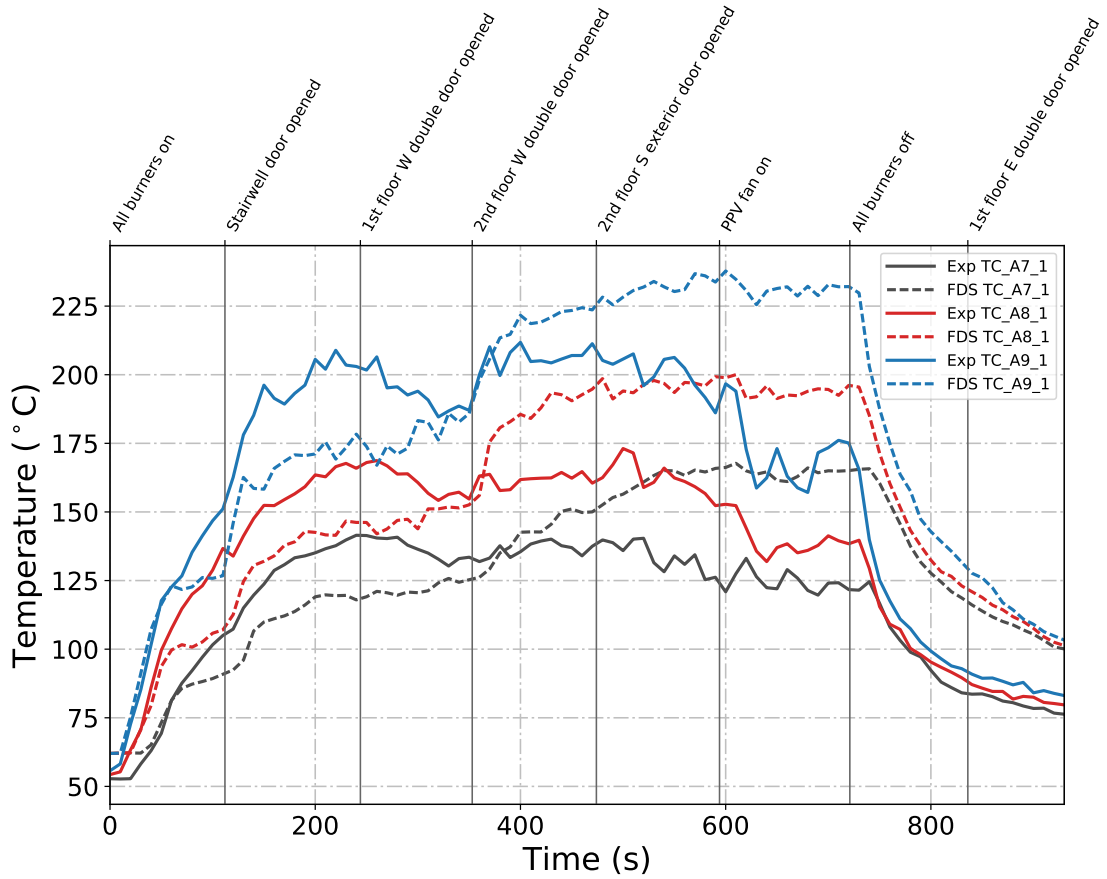


Figure B.25: Plots of measured and predicted ceiling jet temperatures on the second floor of the West Structure during Test 25.

### *Thermocouple Array Temperatures*

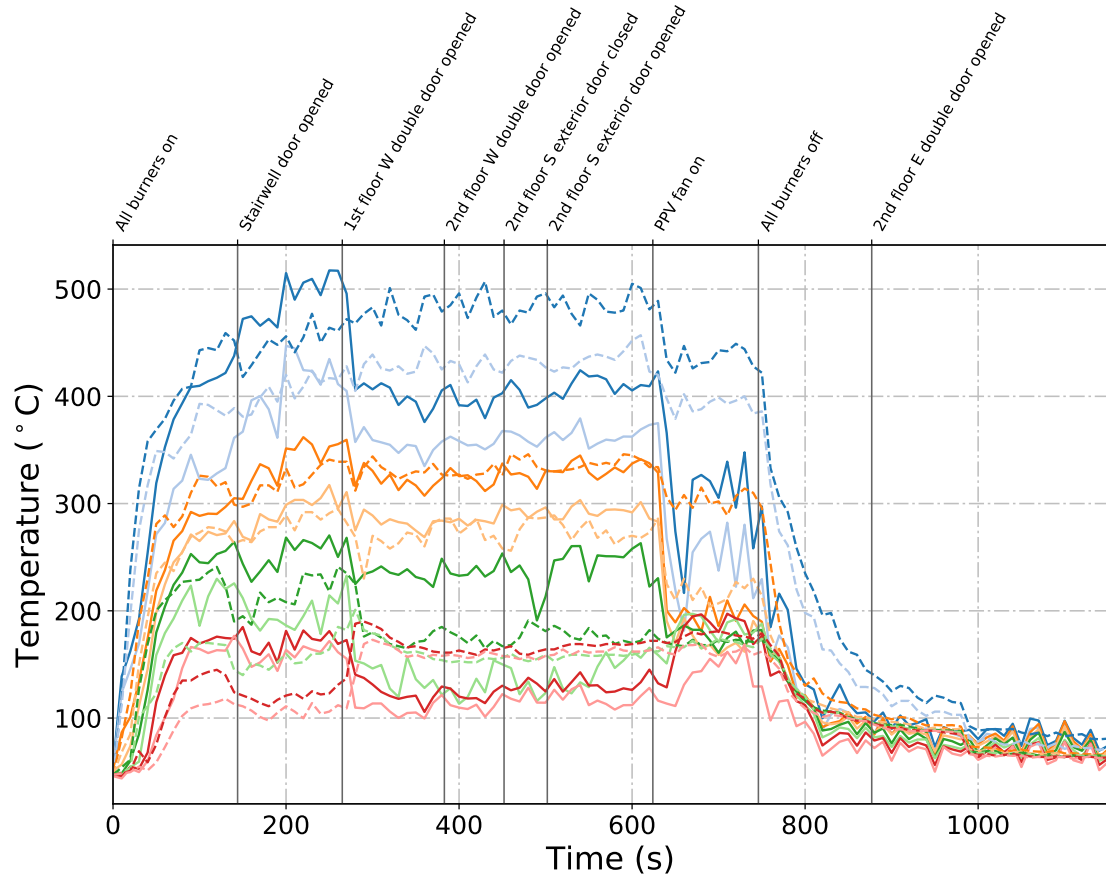


Figure B.26: Plots of measured and predicted temperatures during Test 24 obtained from thermocouple array A1.

## B.2 Gas Species Concentration

### $O_2$ Concentration

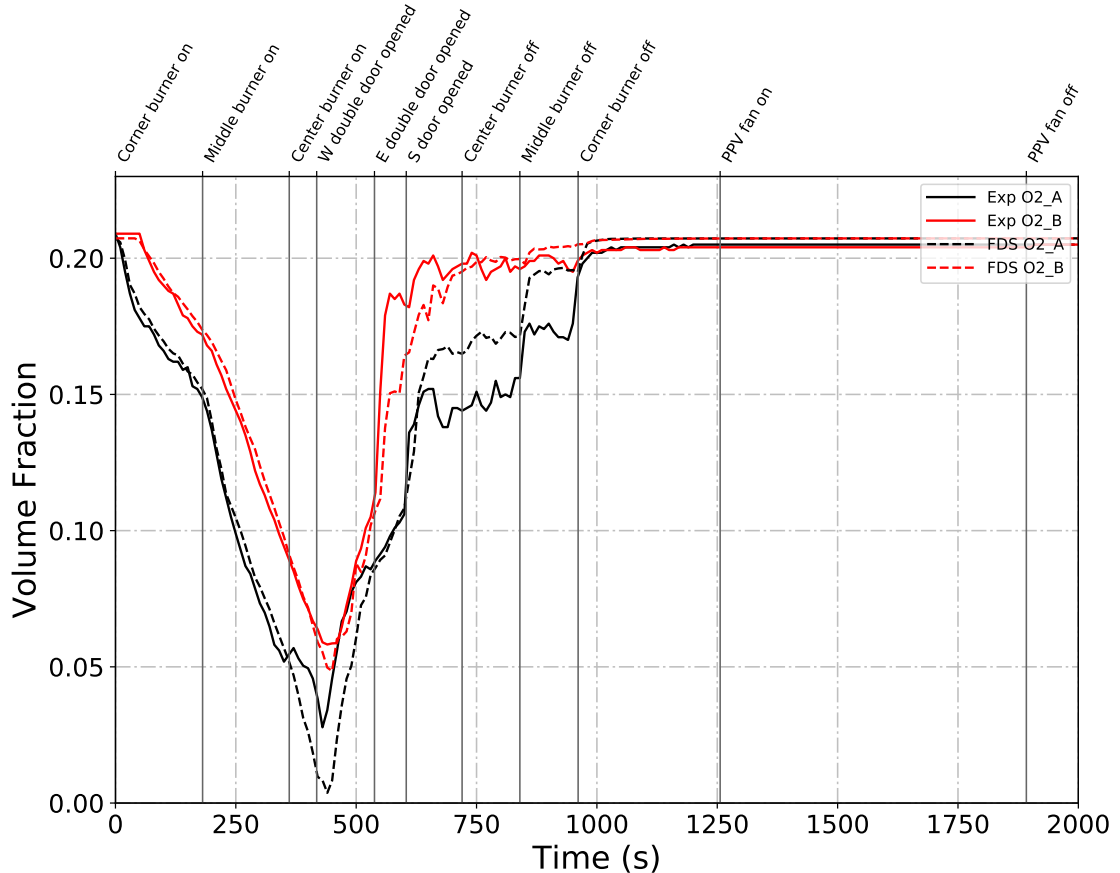


Figure B.27: Plots of measured and predicted  $O_2$  concentration in the fire room (black plots) and north room (red plots) of the East Structure during Test 2.

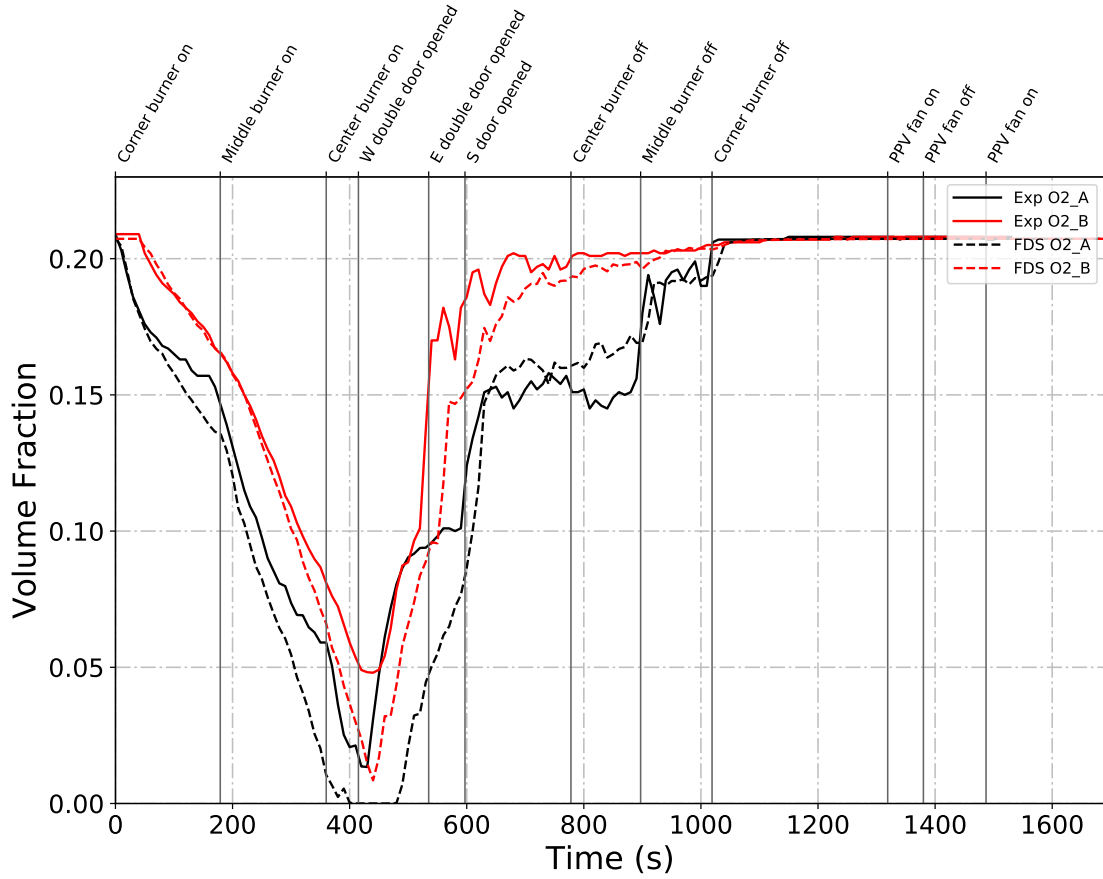


Figure B.28: Plots of measured and predicted  $O_2$  concentration in the fire room (black plots) and north room (red plots) of the East Structure during Test 4.

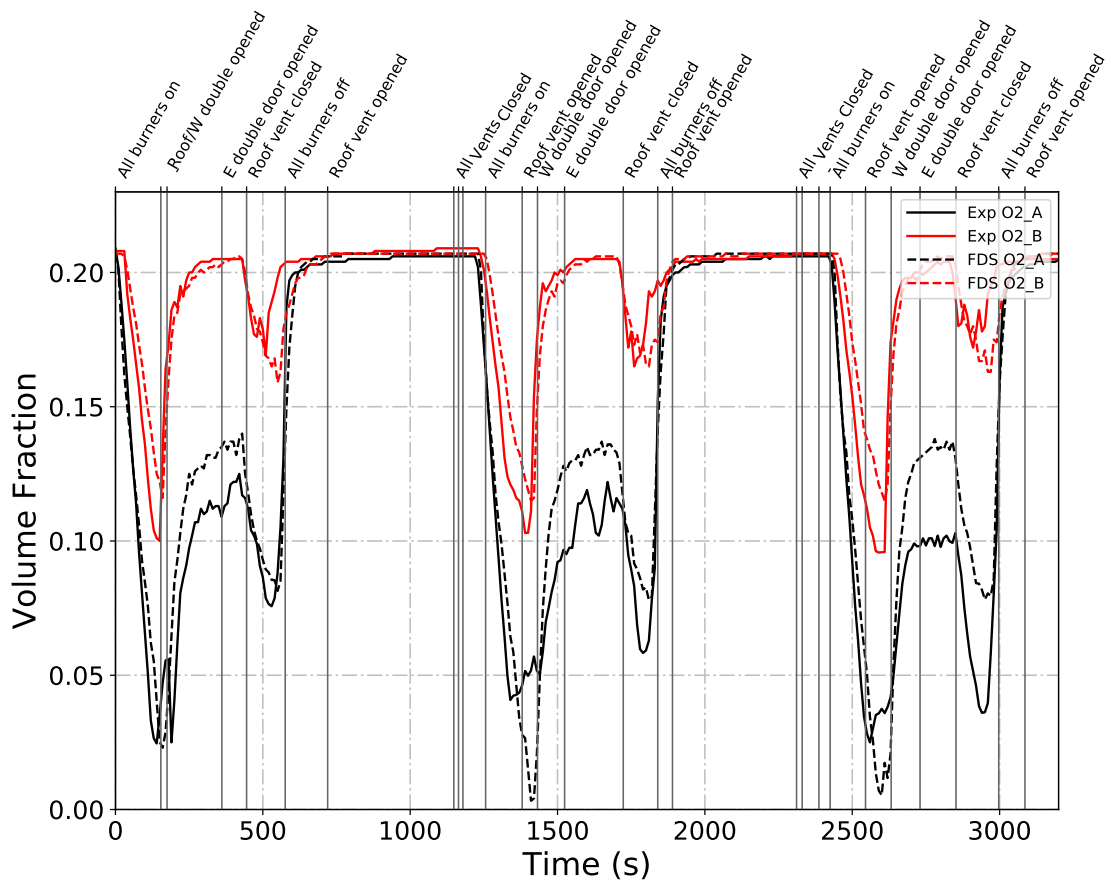


Figure B.29: Plots of measured and predicted  $O_2$  concentration in the fire room (black plots) and north room (red plots) of the East Structure during Test 5.

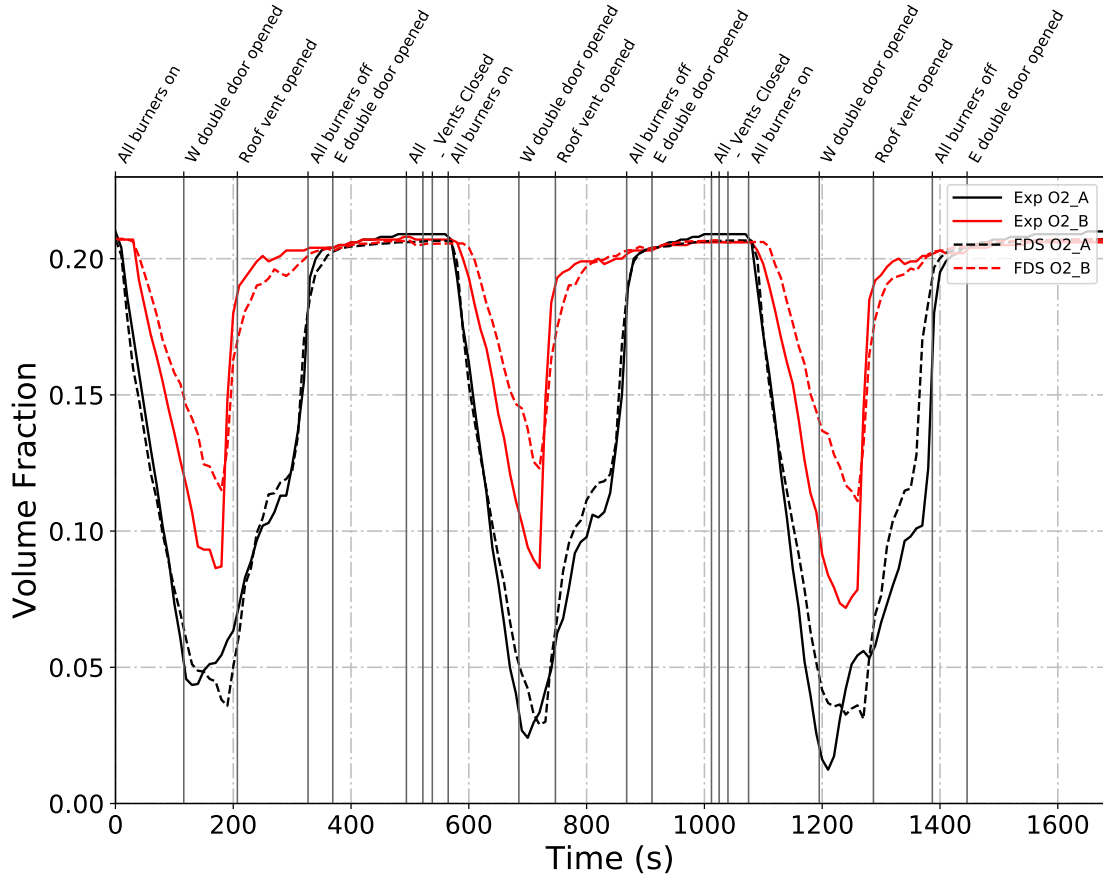


Figure B.30: Plots of measured and predicted  $O_2$  concentration in the fire room (black plots) and north room (red plots) of the East Structure during Test 6.

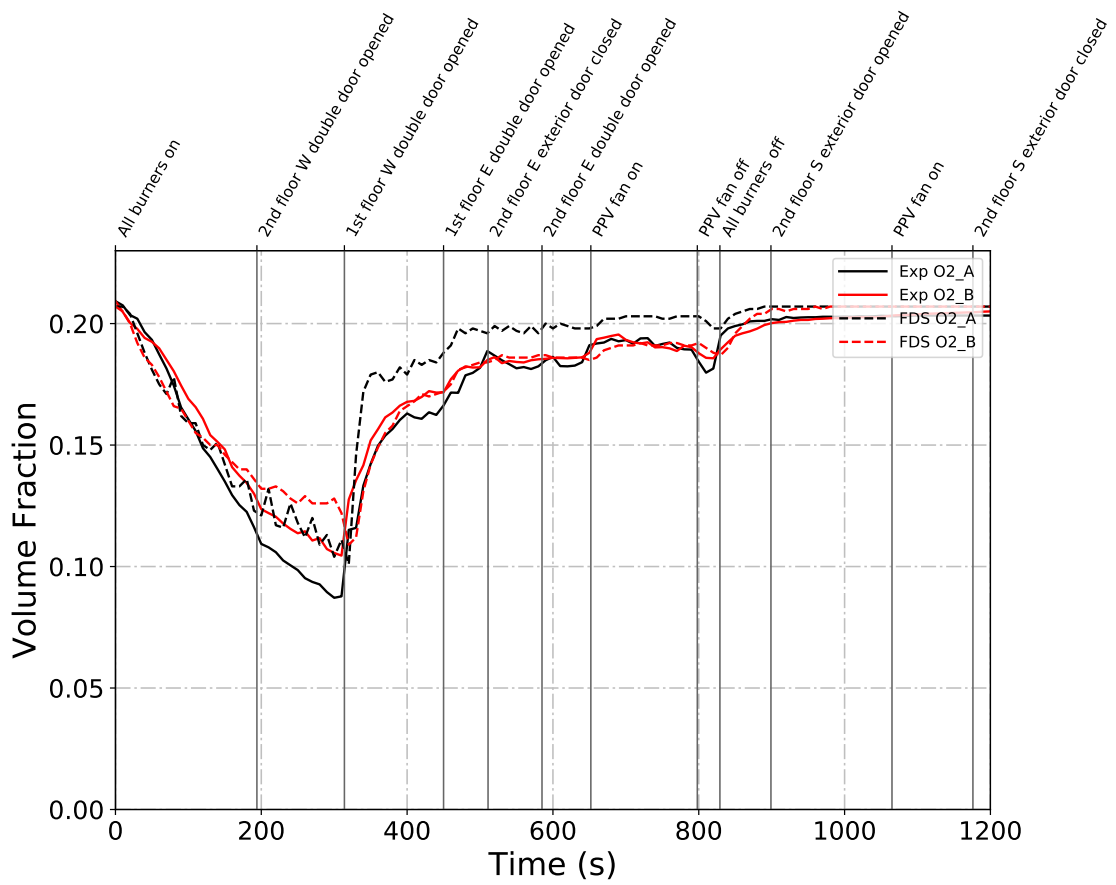


Figure B.31: Plots of measured and predicted  $O_2$  concentration on the first floor (black plots) and second floor (red plots) of the West Structure during Test 22.

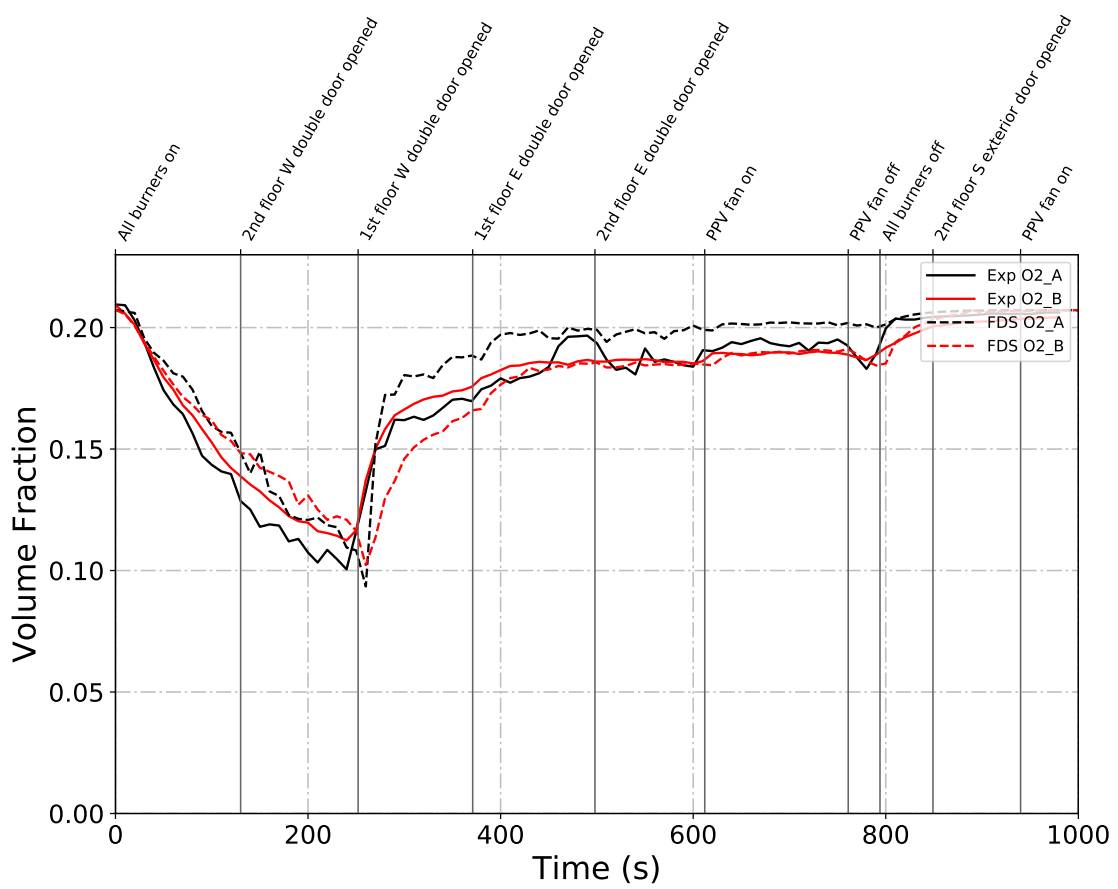


Figure B.32: Plots of measured and predicted  $O_2$  concentration on the first floor (black plots) and second floor (red plots) of the West Structure during Test 23.

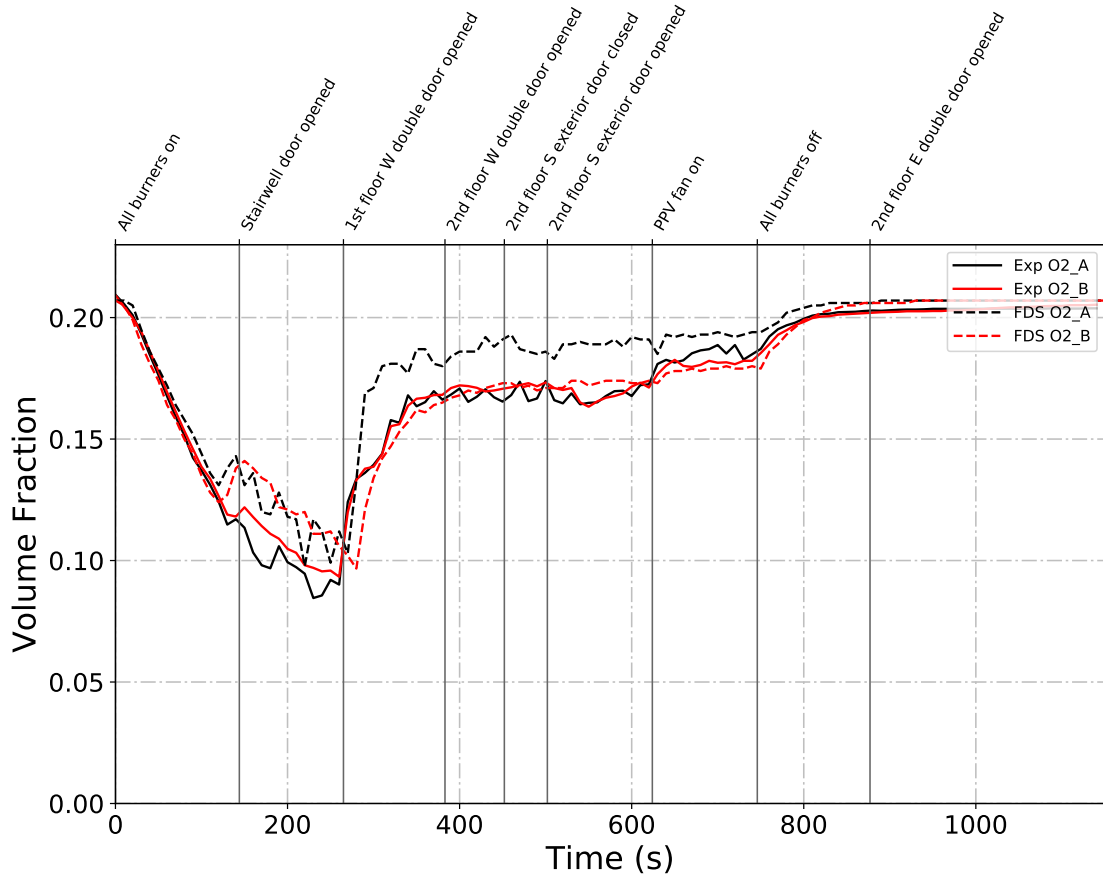


Figure B.33: Plots of measured and predicted  $O_2$  concentration on the first floor (black plots) and second floor (red plots) of the West Structure during Test 24.

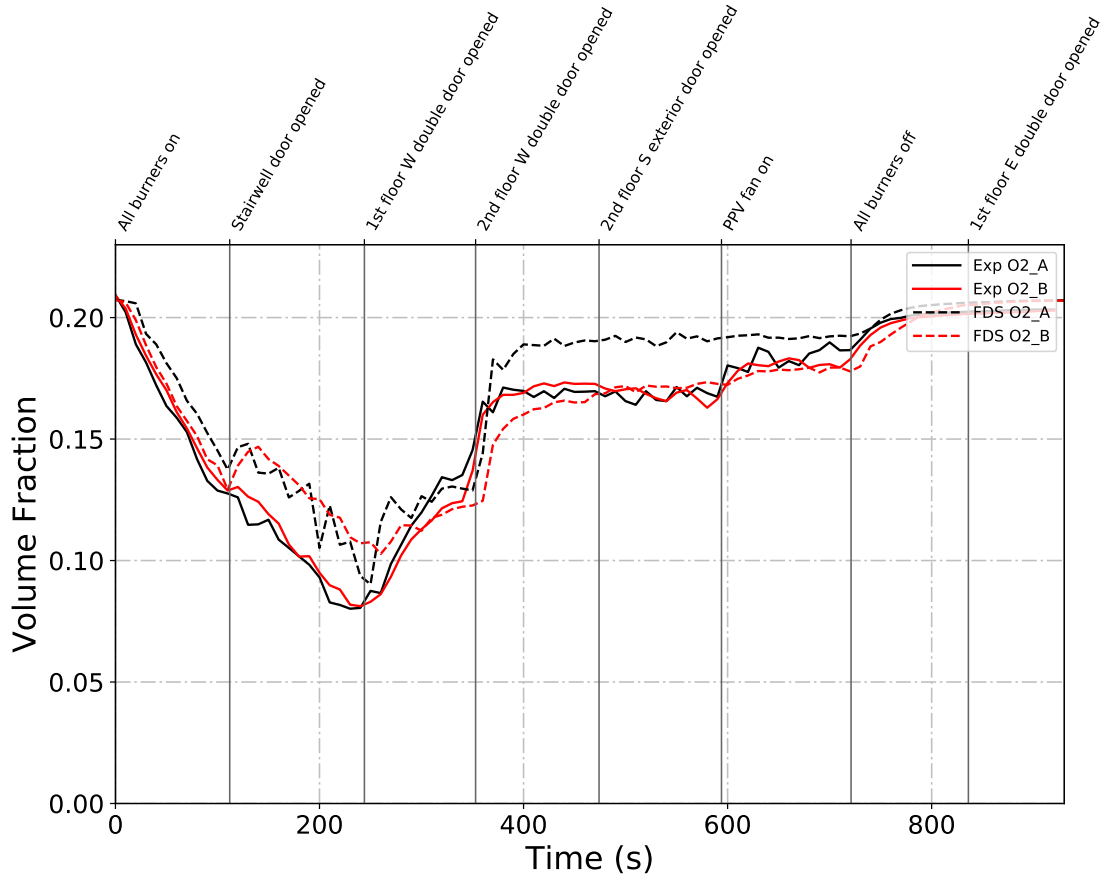


Figure B.34: Plots of measured and predicted  $O_2$  concentration on the first floor (black plots) and second floor (red plots) of the West Structure during Test 25.

## $CO_2$ Concentration

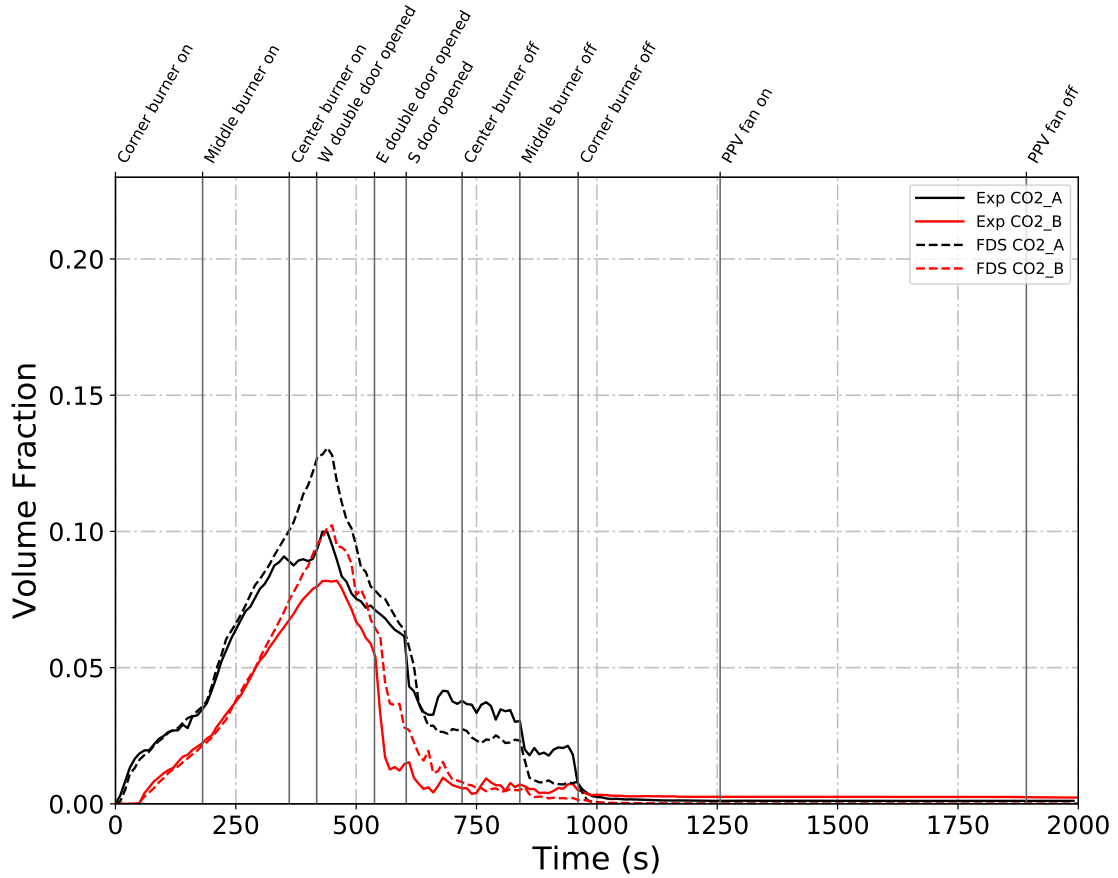


Figure B.35: Plots of measured and predicted  $CO_2$  concentration in the fire room (black plots) and north room (red plots) of the East Structure during Test 2.

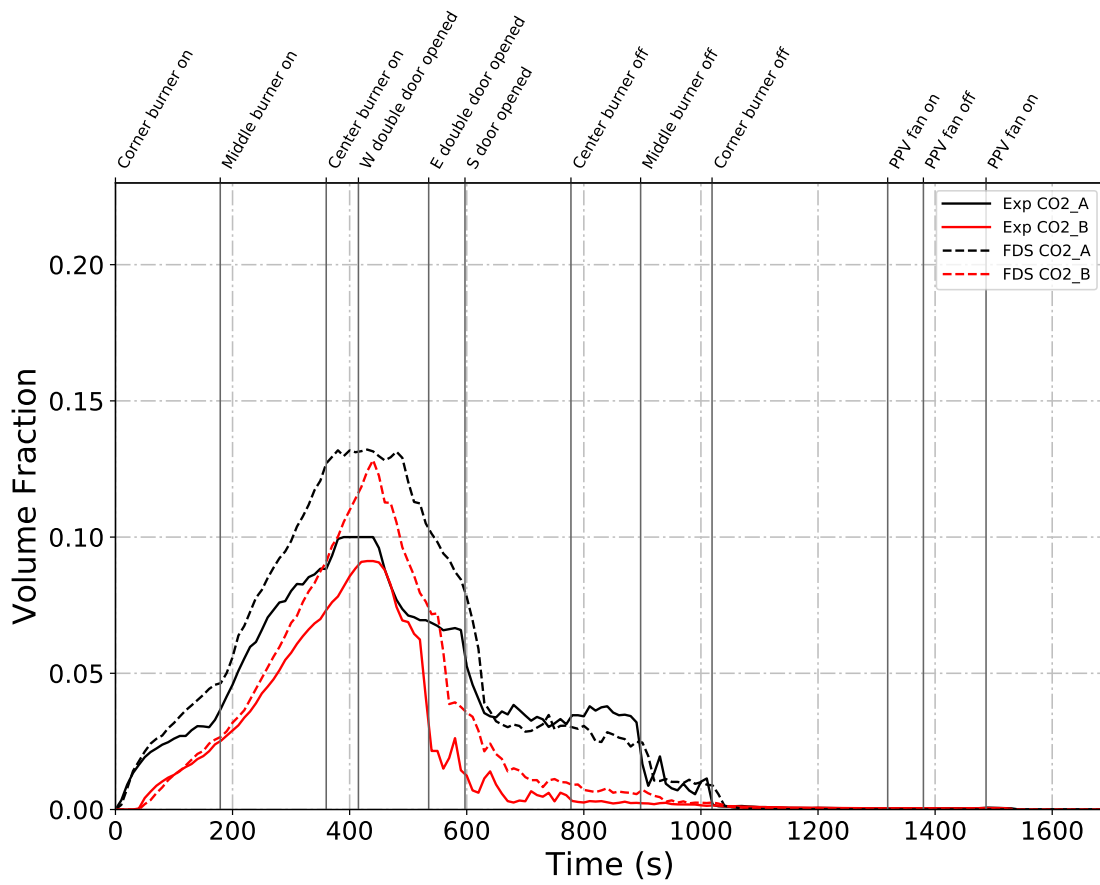


Figure B.36: Plots of measured and predicted  $CO_2$  concentration in the fire room (black plots) and north room (red plots) of the East Structure during Test 4.

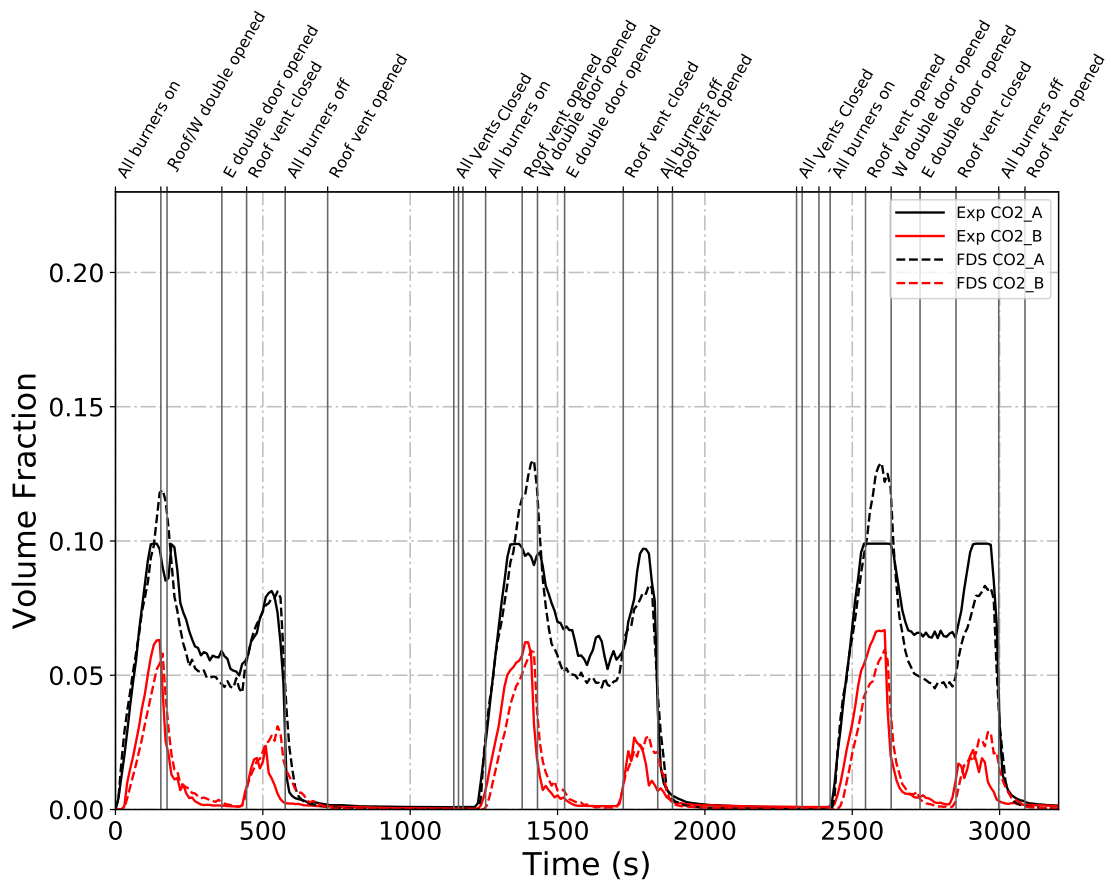


Figure B.37: Plots of measured and predicted  $CO_2$  concentration in the fire room (black plots) and north room (red plots) of the East Structure during Test 5.

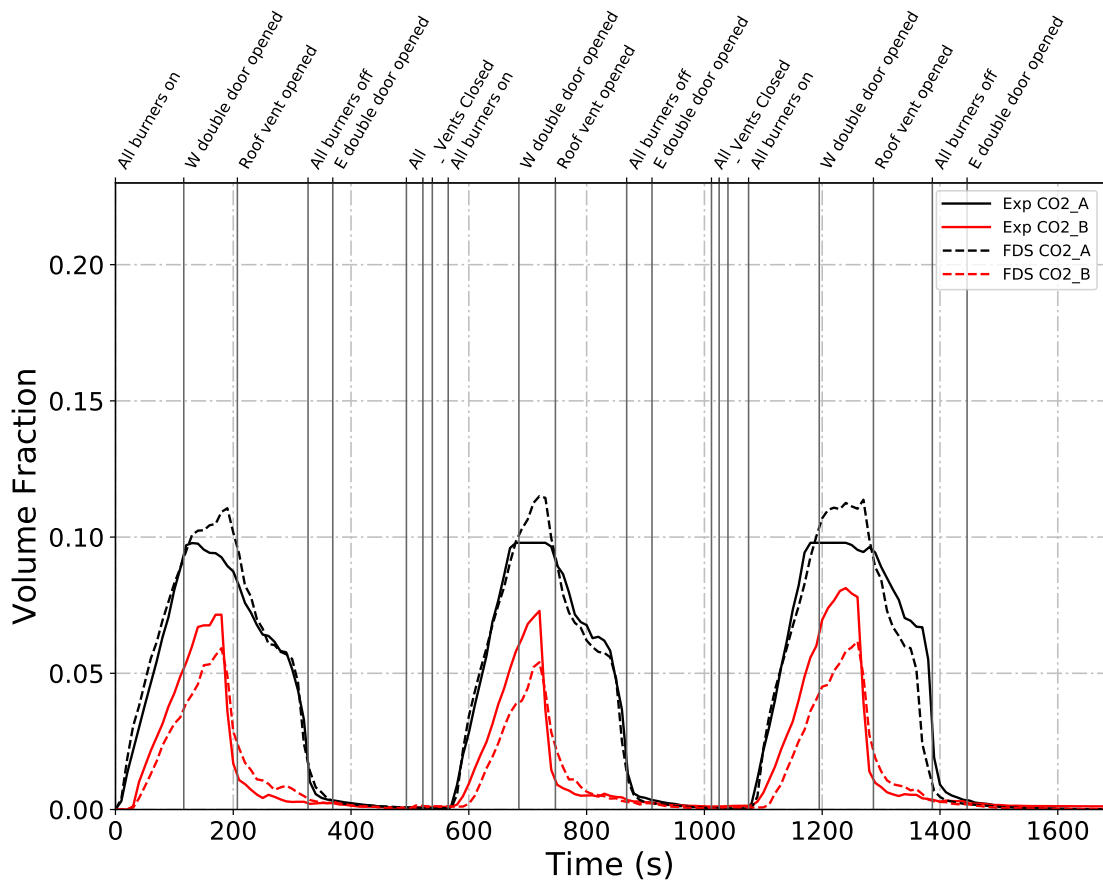


Figure B.38: Plots of measured and predicted  $CO_2$  concentration in the fire room (black plots) and north room (red plots) of the East Structure during Test 6.

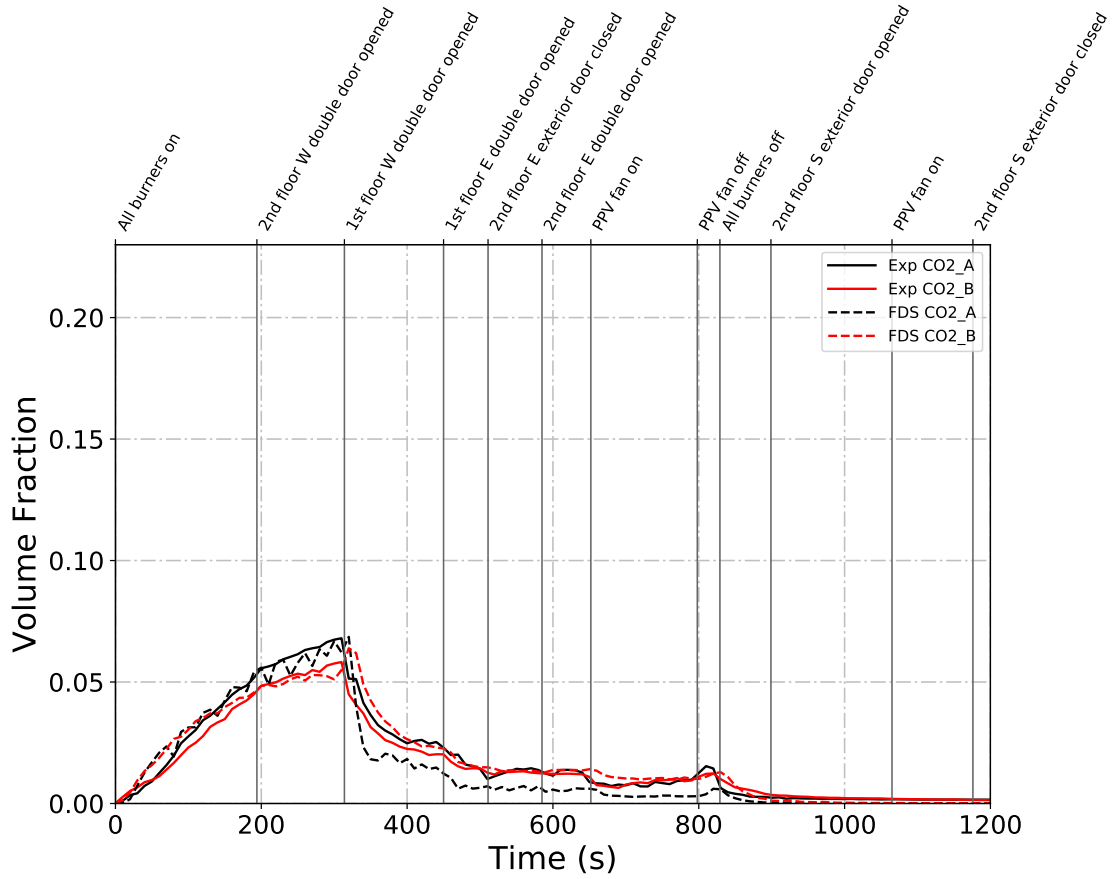


Figure B.39: Plots of measured and predicted  $CO_2$  concentration on the first floor (black plots) and second floor (red plots) of the West Structure during Test 22.

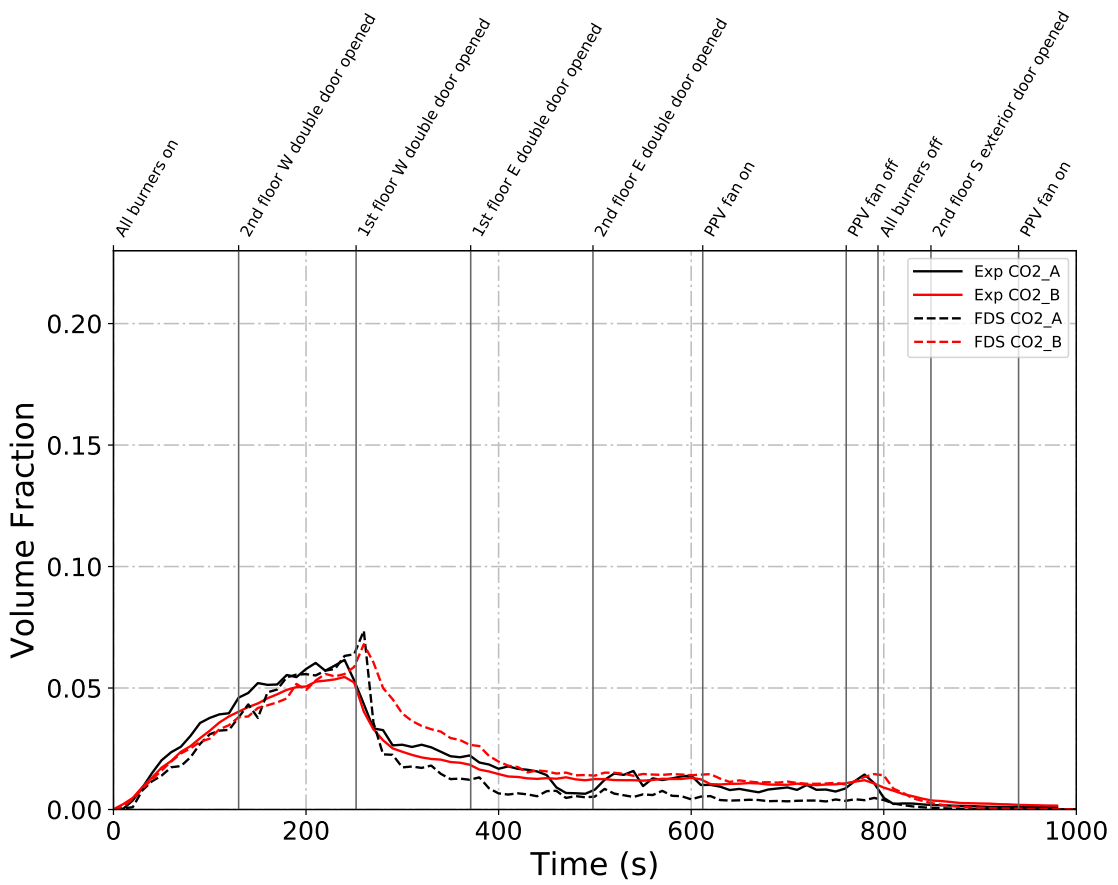


Figure B.40: Plots of measured and predicted  $CO_2$  concentration on the first floor (black plots) and second floor (red plots) of the West Structure during Test 23.

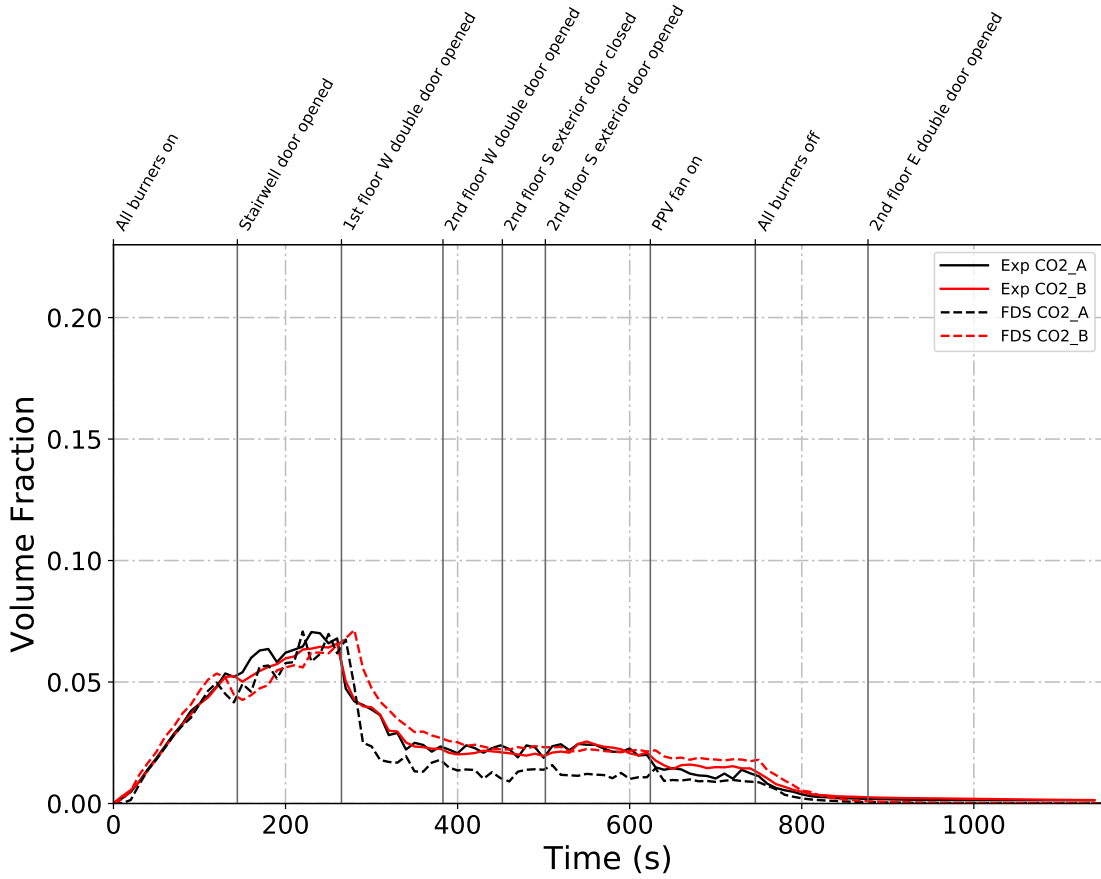


Figure B.41: Plots of measured and predicted  $CO_2$  concentration on the first floor (black plots) and second floor (red plots) of the West Structure during Test 24.

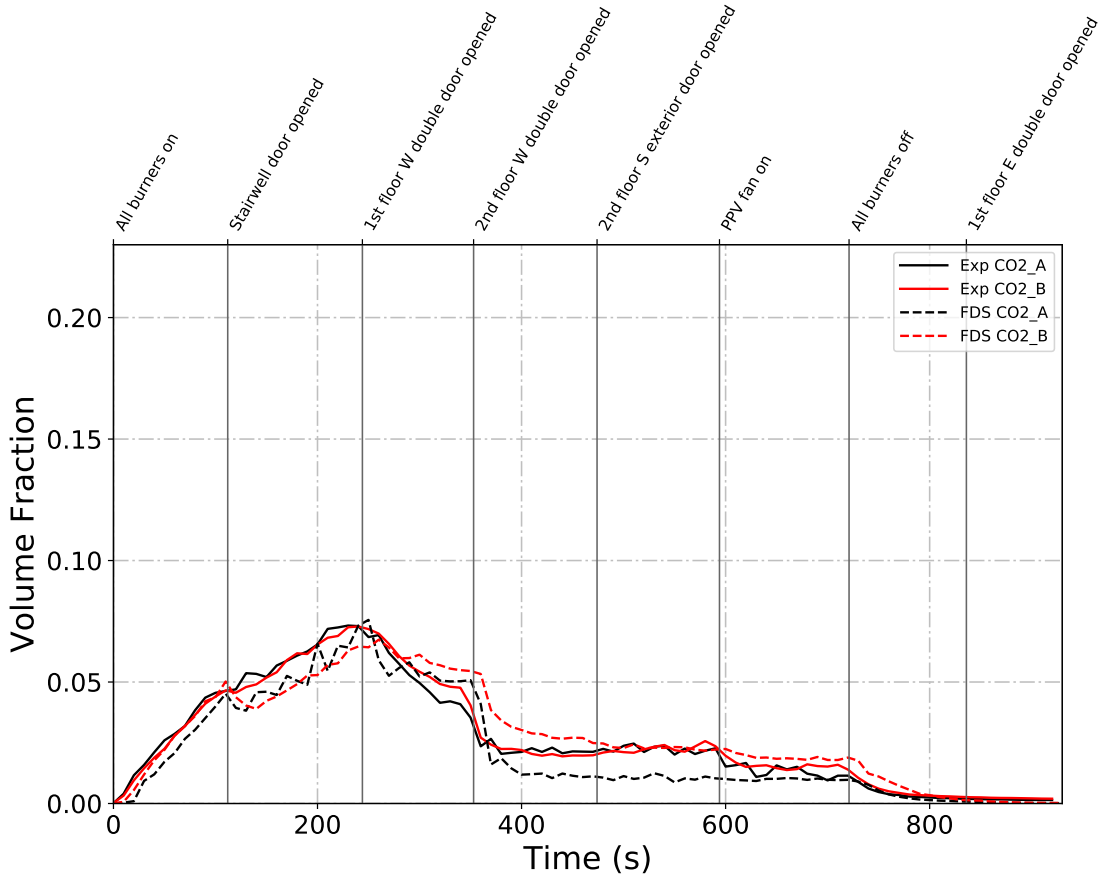


Figure B.42: Plots of measured and predicted  $CO_2$  concentration on the first floor (black plots) and second floor (red plots) of the West Structure during Test 25.

### B.3 Gas Velocity

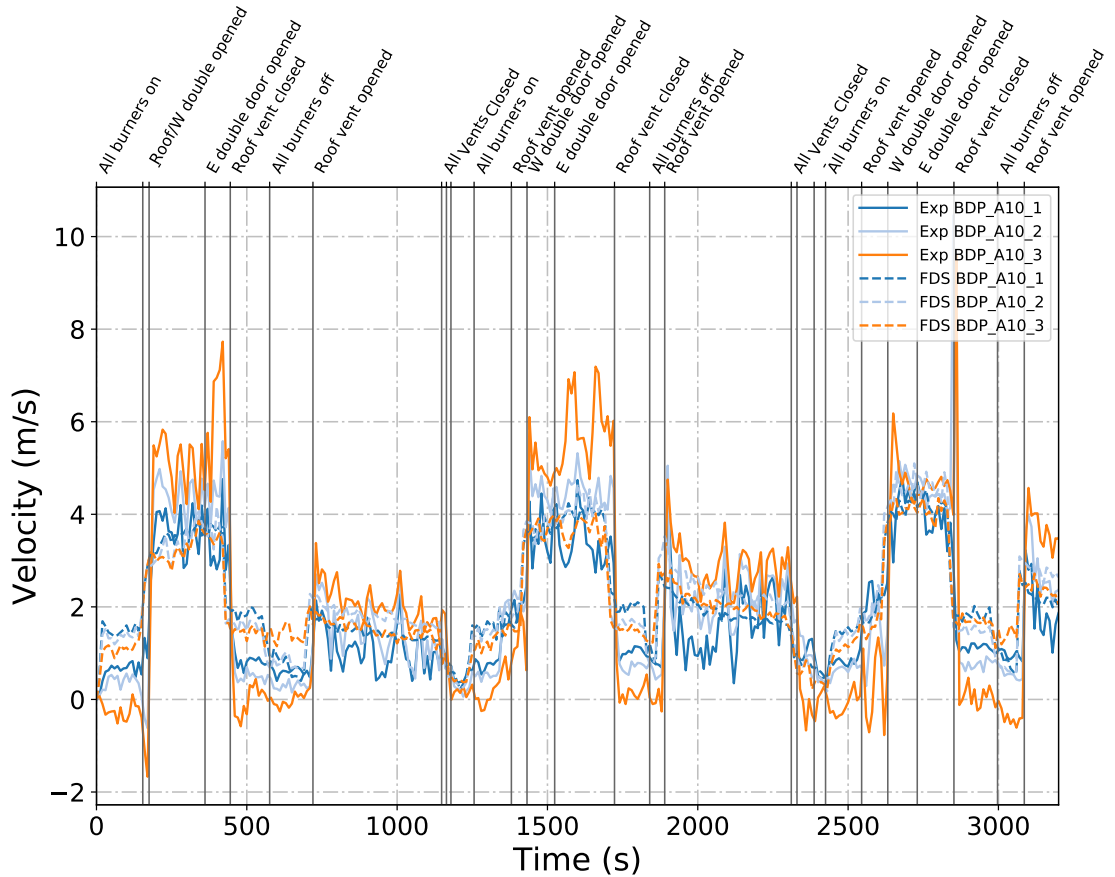


Figure B.43: Plots of measured and predicted gas velocity through the roof vent during Test 5.

## B.4 Total Heat Flux

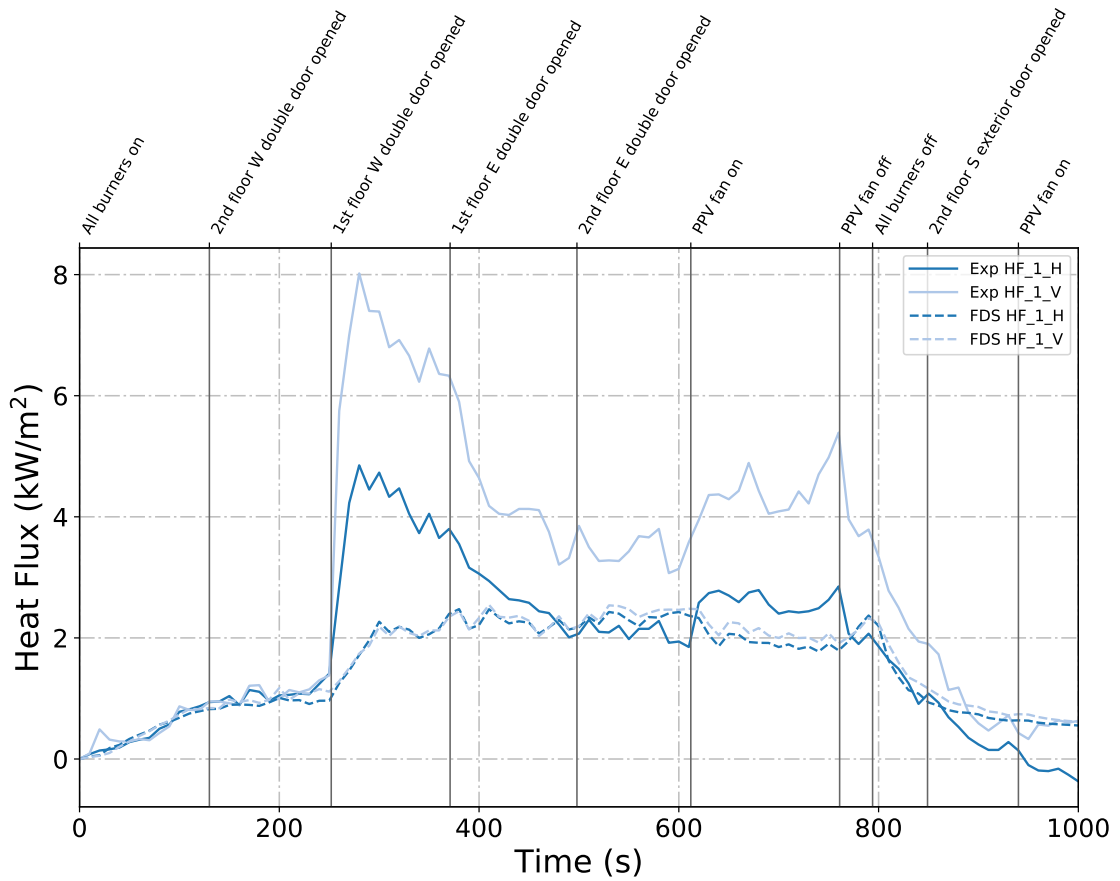


Figure B.44: Plots of measured and predicted heat flux measured by total heat flux gauges at the top of the stairs facing the stair doorway ('H') and facing the ceiling ('V').

## Bibliography

- [1] K. McGrattan, S. Hostikka, R. McDermott, J. Floyd, C. Weinschenk, and K. Overholt. *Fire Dynamics Simulator, User's Guide*. National Institute of Standards and Technology, Gaithersburg, Maryland, USA, and VTT Technical Research Centre of Finland, Espoo, Finland, sixth edition, September 2013.
- [2] K. McGrattan, S. Hostikka, R. McDermott, J. Floyd, C. Weinschenk, and K. Overholt. *Fire Dynamics Simulator, Technical Reference Guide*. National Institute of Standards and Technology, Gaithersburg, Maryland, USA, and VTT Technical Research Centre of Finland, Espoo, Finland, sixth edition, September 2013. Vol. 1: Mathematical Model; Vol. 2: Verification Guide; Vol. 3: Validation Guide; Vol. 4: Configuration Management Plan.
- [3] K. McGrattan, S. Hostikka, R. McDermott, J. Floyd, C. Weinschenk, and K. Overholt. *Fire Dynamics Simulator, Technical Reference Guide, Volume 2: Verification*. National Institute of Standards and Technology, Gaithersburg, Maryland, USA, and VTT Technical Research Centre of Finland, Espoo, Finland, sixth edition, September 2013.
- [4] K. McGrattan, S. Hostikka, R. McDermott, J. Floyd, C. Weinschenk, and K. Overholt. *Fire Dynamics Simulator, Technical Reference Guide, Volume 3: Validation*. National Institute of Standards and Technology, Gaithersburg, Maryland, USA, and VTT Technical Research Centre of Finland, Espoo, Finland, sixth edition, September 2013.
- [5] B.N. Taylor and C.E. Kuyatt. Guidelines for Evaluating and Expressing the Uncertainty of NIST Measurement Results. NIST Technical Note 1297, National Institute of Standards and Technology, Gaithersburg, Maryland, 1994.
- [6] Stanley Hand Tools, New Britain, Connecticut. *User Manual TLM 100*, 2013.
- [7] T. Butcher, S. Cook, L. Crown, and R. Harshman. NIST Handbook 44: Specifications, Tolerances, and Other Technical Requirements for Weighing and Measuring Devices. *National Institute of Standards, Gaithersburg, MD*, 2012.

- [8] Omega Engineering Inc., Stamford, Connecticut. *The Temperature Handbook*, 2004.
- [9] L.G. Blevins. Behavior of bare and aspirated thermocouples in compartment fires. In *National Heat Transfer Conference, 33rd Proceedings*, pages 15–17, 1999.
- [10] W.M. Pitts, E. Braun, R. Peacock, H. Mitler, E. Johnson, P. Reneke, and L.G. Blevins. Temperature uncertainties for bare-bead and aspirated thermocouple measurements in fire environments. *ASTM Special Technical Publication*, 1427:3–15, 2003.
- [11] Medtherm Corporation, Huntsville, Alabama. *64 Series Heat Flux Transducers*, 2003.
- [12] W.M. Pitts, A.V. Murthy, J.L. de Ris, J. Filtz, K. Nygård, D. Smith, and I. Wetterlund. Round robin study of total heat flux gauge calibration at fire laboratories. *Fire Safety Journal*, 41(6):459–475, 2006.
- [13] M. Bundy, A. Hamins, E.L. Johnsson, S.C. Kim, G.H. Ko, and D.B. Lenhart. Measurements of Heat and Combustion Products in Reduced-Scale Ventilated-Limited Compartment Fires. NISTTN 1483, National Institute of Standards and Technology, Gaithersburg, MD, 2007.
- [14] A. Lock, M. Bundy, E.L. Johnsson, A. Hamins, G.H. Ko, C. Hwang, P. Fuss, and R. Harris. Experimental study of the effects of fuel type, fuel distribution, and vent size on full-scale underventilated compartment fires in an ISO 9705 room. NISTTN 1603, National Institute of Standards and Technology, Gaithersburg, MD, 2008.
- [15] R.A. Bryant. A comparison of gas velocity measurements in a full-scale enclosure fire. *Fire Safety Journal*, 44:793–800, 2009.
- [16] Romet Limited, East Mississauga, Ontario. *Rotary Gas Meter RM3000 Technical Specification*, 2014.
- [17] K. Hill, J. Dreisbach, F. Joglar, B. Najafi, K. McGrattan, R. Peacock, and A. Hamins. Verification and Validation of Selected Fire Models for Nuclear Power Plant Applications. NUREG-1824, United States Nuclear Regulatory Commission, Washington, DC, 2007.
- [18] K. McGrattan and B. Toman. Quantifying the predictive uncertainty of complex numerical models. *Metrologia*, 48:173–180, 2011.
- [19] M.L. Janssens and H.C. Tran. Data Reduction of Room Tests for Zone Model Validation. *Journal of Fire Science*, 10:528–555, 1992.